

The Development of Carbon Fiber Reinforced Polymer Upright Prototypes

for a Formula SAE Race Vehicle

By

Copyright 2021

Nicholas Davis

Submitted to the graduate degree program in Mechanical Engineering and the Graduate Faculty of the University of Kansas in partial fulfillment of the requirements for the degree of Master of Science.

---

Chairperson: Dr. Robert M. Sorem

---

Dr. Elizabeth Friis

---

Dr. Lorin Maletsky

Date Defended: November 19, 2021

The Thesis Committee for Nicholas Davis certifies  
that this is the approved version of the following thesis:

The Development of Carbon Fiber Reinforced Polymer Upright Prototypes  
for a Formula SAE Race Vehicle

---

Chairperson: Dr. Robert M. Sorem

Date Approved: December 17, 2021

## **Abstract**

The upright functions as a bearing housing and connects all outboard linkages from the chassis to the wheel and tire, making their design critical to vehicle performance. To this end, this project focused on the development of four unique carbon fiber reinforced polymer uprights with all critical features molded after the initial cure with minimal post-processing from a common tool set. The composite uprights were developed through material failure strength evaluation, application of finite element analysis, and verified through on-vehicle static structural testing for use on the University of Kansas Formula SAE vehicle.

Through the composite laminate development, components were designed with a Hashin factor of safety of 1.650 for the front upright and 1.582 for the rear upright. Moreover, utilizing a composite material resulted in a decrease in mass compared to aluminum of 55.0% and 20.0% for the front and rear uprights, respectively, while allowing for a component camber change contribution of 0.015 degree/g and 0.153 degree/g at the tire. Static structural testing utilizing strain gages suggested an average error of 5.4% for the front uprights and 4.8% for the rear uprights in comparison to the finite element models. As a result, the performance of a Formula SAE vehicle is improved through the development of carbon fiber reinforced polymer uprights.

## **Acknowledgements**

I wish to extend a special thanks to Dr. Robert Sorem for his mentorship through my undergraduate and graduate careers. I am thankful for the experience and time that Dr. Elizabeth Friis and Dr. Lorin Maletsky have contributed to the project as committee members. I appreciate the guidance in machining and fabrication from Charles Gabel and Ash Shadrick from the Mechanical Engineering Machine shop over the many years of SAE projects. Composite material design and technical expertise provided by Dr. Richard Hale was greatly appreciated. Manufacturing assistance for the composite tooling from Adam Rosploch and Peyton Miller was a huge help in the timely completion of this project. The resources provided by Tom Roudebush and Troy Oberle at AkroFire, and Royal Lovingfoss at the National Institute for Aviation Research were invaluable to the composite material property validation. I appreciate all the motivation and constructive criticism from the Jayhawk Motorsport alumni throughout the development of the project. I would not have made it to this milestone in my academic career without the loving encouragement from my parents, from whom I am a first-generation college graduate. I am extremely thankful for the companionship through the times of challenge and celebration from my best friend Bailey and four-legged friends Bruiser and Jax.

## Table of Contents

Abstract .....	iii
Acknowledgements .....	iv
Table of Contents .....	v
List of Tables .....	vii
List of Figures .....	viii
1. Introduction .....	1
1.1. Objectives .....	2
1.2. Design Limitations .....	3
1.3. General Requirements of Uprights .....	3
2. Background .....	6
2.1. Vehicle Dynamics .....	6
2.1.1. Unsprung Mass .....	7
2.1.2. Tires .....	7
2.1.3. Suspension Geometry .....	10
2.2. Composite Materials .....	12
2.3. Available Technologies .....	19
2.3.1. Research and Development within Transportation Sector .....	19
3. General Design of Uprights .....	25
3.1. Design Requirements .....	25
3.2. Upright Design .....	25
3.2.1. Legacy JMS Upright Designs .....	26
3.2.2. New JMS Upright Design .....	29
3.3. Modular Tool .....	37
4. Materials .....	43
4.1. Material Selection .....	43
4.1.1. Glass Transition vs Strength and Stiffness .....	44
4.2. Material Properties .....	46
4.2.1. Material Strength and Stiffness Data .....	46
4.2.2. Material Validation .....	47
4.3. Composite Constituent Content via Matrix Ignition .....	52
4.4. Discussion .....	59
5. Analysis .....	64
5.1. Model Setup .....	64
5.1.1. Load Cases .....	67
5.2. Laminate Development .....	68
5.3. Composite Failure Analysis .....	73
5.3.1. Maximum Strain Theory .....	74
5.3.2. Tsai-Wu Failure Theory .....	75
5.3.3. Hashin Failure Theory .....	77
5.3.4. Failure Theory Comparison .....	78
5.4. Fiber Misalignment Study .....	79
5.5. Critical Ply Analysis .....	80
5.6. Analysis Discussion .....	83
6. Manufacturing .....	85

6.1. Molds and Tooling .....	85
6.2. Composite Manufacturing Process.....	86
6.2.1. Lamina Preparation.....	86
6.2.2. Layup.....	86
6.2.3. Laminate Cure .....	92
6.3. Final Processing .....	93
7. Model Validation .....	96
7.1. Static Lateral Loading .....	96
7.2. Methods .....	96
7.3. Procedure .....	100
7.4. Results.....	104
8. Conclusions .....	107
References .....	109
Appendix A: Left Front and Left Rear Engineering Drawings .....	113
Appendix B: Front and Rear Upright Manufacturing Overview .....	129

## List of Tables

Table 4.1.1.1: Material Properties of Various Biaxial Weave Prepreg Composites.....	45
Table 4.2.1.1: Material Properties for T650/35 3K Prepreg Composite.....	47
Table 4.2.2.1: 8HS Control Coupons – Axis-1 Tensile Strength and Modulus (RTD).....	49
Table 4.2.2.2: PW Control Coupons – Axis-1 Tensile Strength and Modulus (RTD).....	49
Table 4.2.2.3: 8HS Control Coupons – Interlaminar Shear Strength (RTD).....	50
Table 4.2.2.4: PW Control Coupons – Interlaminar Shear Strength (RTD).....	50
Table 4.3.1: Fiber Content by Percentage Weight.....	54
Table 4.3.2: Matrix Content by Percentage Weight.....	54
Table 4.3.3: Fiber Content by Percentage Volume.....	55
Table 4.3.4: Matrix Content by Percentage Volume.....	56
Table 4.3.5: Void Content by Percentage Volume.....	56
Table 4.4.1: Effects of Ply Rotation on Tensile Modulus.....	61
Table 5.1.1: Material Allowable Values for Finite Element Model.....	64
Table 5.1.1.1: JMS19C Front Tire Load Cases.....	68
Table 5.1.1.2: JMS19C Rear Tire Load Cases.....	68
Table 5.2.1: Front Upright Laminate Development.....	69
Table 5.2.2: Rear Upright Laminate Development.....	70
Table 5.2.3: Load Case Failure Index Comparison (Hashin) – Front Upright.....	73
Table 5.2.4: Load Case Failure Index Comparison (Hashin) – Rear Upright.....	73
Table 5.3.4.1: Failure Theory Comparison – Front Upright.....	79
Table 5.3.4.2: Failure Theory Comparison – Rear Upright.....	79
Table 5.4.1: Fiber Misalignment Study – Front Upright.....	80
Table 5.4.2: Fiber Misalignment Study – Rear Upright.....	80
Table 5.5.1: Critical Ply Analysis – Front Upright.....	81
Table 5.5.2: Critical Ply Analysis – Rear Upright.....	81
Table 5.5.3: Three-Dimensional Stress State Failure Analysis – Front Upright.....	82
Table 5.5.4: Three-Dimensional Stress State Failure Analysis – Rear Upright.....	82
Table 7.2.1: FEA Load Cases.....	97
Table 7.2.2: Local Strain Averages for FEA Load Cases.....	100
Table 7.3.1: Averaged Strain Data from Lateral Loading of Front Quarter Assembly.....	103
Table 7.3.2: Averaged Strain Data from Lateral Loading of Rear Quarter Assembly.....	103
Table 7.4.1: Front Upright Strain Comparison – FEA vs Experimental.....	104
Table 7.4.2: Rear Upright Strain Comparison – FEA vs Experimental.....	104
Table 7.4.3: Front Upright FEA Positional Strain Error.....	105
Table 7.4.4: Rear Upright FEA Positional Strain Error.....	105

## List of Figures

Figure 1.1: Jayhawk Motorsports, 2019 Combustion Race Vehicle .....	1
Figure 1.3.1: 2019 FSAE Keep Out Zone [1].....	4
Figure 2.1: SAE Vehicle Dynamics Coordinate System [2] .....	6
Figure 2.1.2.1: SAE Tire Coordinate System [4] .....	8
Figure 2.1.3.1: Kingpin Geometry [3] .....	11
Figure 2.3.1.1: Hybrid Carbon Fiber/Aluminum Suspension Knuckle [11].....	22
Figure 2.3.1.2: Composite Knuckle-Tie Blade [12] .....	23
Figure 3.2.1.1: JMS Full Composite Rear Upright.....	26
Figure 3.2.1.2: JMS 2018 Front Upright.....	28
Figure 3.2.2.1: JMS 2019 Front Upright.....	29
Figure 3.2.2.2: JMS 2019 Rear Upright.....	30
Figure 3.2.2.3: Drop-In Shim .....	32
Figure 3.2.2.4: Front Upright Upper Ball Joint Mount Assembly with Shims .....	33
Figure 3.2.2.5: Ultimate Tensile Strength vs Temperature of a Two and Seven Series Aluminum .....	34
Figure 3.2.2.6: Rear Upright Lower Ball Joint Mount.....	35
Figure 3.2.2.7: 100% Ackermann Steering Mount.....	36
Figure 3.3.1: Tool Configuration for Left Front Upright.....	37
Figure 3.3.2: Secondary Drill Fixtures for Front Upright.....	38
Figure 3.3.3: Tool Configuration for Left Rear Upright .....	39
Figure 3.3.4: Bearing Housing Sample .....	40
Figure 3.3.5: Ideal Bearing Mandrel Geometry.....	41
Figure 3.3.6: Ideal Base Plate Geometry.....	42
Figure 4.1.1: Temperature Indicating Labels on Rear Upright and Caliper.....	43
Figure 4.1.2: DAQ Data from JMS17C .....	44
Figure 4.2.2.1: Tensile Test Coupon with Fiberglass Bonded Tabs .....	48
Figure 4.2.2.2: Tensile Test Coupon in Uniaxial Load Frame with Extensometer .....	48
Figure 4.2.2.3: Short Beam Shear Test Fixture .....	49
Figure 4.2.2.4: Material Microscopy of Composite Tensile Coupon .....	51
Figure 4.3.1: Test Specimen Before Matrix Ignition .....	52
Figure 4.3.2: Test Specimen in Electric Kiln .....	53
Figure 4.3.3: Test Specimen After Matrix Ignition .....	54
Figure 4.3.4: 5320-1 Vacuum Bag Arrangement for Cure [18] .....	57
Figure 4.4.1: Microscope Image of Manufactured Laminate with Prescribed Layer Orientations (left) vs Fit Ellipses Colored by Determined Rotation Angle (right) [28].....	60
Figure 5.1.1: Side View of Front Upright Boundary Conditions and Loads .....	66
Figure 5.1.2: Rear Upright Boundary Conditions and Loads.....	67
Figure 5.2.1: Design Parameter Values vs Iteration Revision for Front Upright Laminate.....	72
Figure 5.2.2: Design Parameter Values vs Iteration Revision for Rear Upright Laminate.....	72
Figure 5.3.2.1: Comparison of (a) Tsai-Wu and (b) Maximum Strain Failure Theories with Biaxial Strength Data of CFRP [8] .....	75
Figure 6.1.1: Tooling to Manufacture Front Left Upright .....	85
Figure 6.2.2.1: Joining of Both Sides of Tool .....	87
Figure 6.2.2.2: Joining of Inside and Outside Laminates.....	88



Figure 6.2.2.3: Brake Mandrel Installed to Tool .....	89
Figure 6.2.2.4: Debulking of Composite in Oven.....	90
Figure 6.2.2.5: Application of Local Plies to Component.....	91
Figure 6.2.2.6: Example of Supplemental Silicone Tool .....	92
Figure 6.2.3.1: Solvay 5320-1 Cure Cycle [18].....	93
Figure 6.3.1: Partially Assembled Front Corner Suspension Assembly .....	94
Figure 6.3.2: Fully Assembled Rear Upright .....	95
Figure 7.2.1: Strain Gauge Locations on Front Upright - Outboard.....	98
Figure 7.2.2: Strain Gauge Locations on Front Upright - Inboard .....	98
Figure 7.2.3: Strain Gauge Locations on Rear Upright - Outboard.....	99
Figure 7.2.4: Strain Gauge Locations on Rear Upright - Inboard .....	99
Figure 7.2.5: Example of Element Strain Averaging for Location Two on Front Upright.....	100
Figure 7.3.1: Strain Gauges Installed on Rear Upright.....	101
Figure 7.3.2: Maximum Lateral Load on Front Quarter Assembly .....	102

## Acronyms

8HS – eight-harness satin  
ABS - acrylonitrile butadiene styrene  
ABS – anti-lock brake system  
AM – additive manufacturing  
AN – Army-Navy  
ASTM - American Society for Testing and Materials  
CAD – Computer Aided Design  
CAE - Computer Aided Engineering  
CFRP – Carbon Fiber Reinforced Polymer  
CG – center of gravity  
CLT – Classical Lamination Theory  
CNC – Computer Numerical Control  
CTE - coefficient of thermal expansion  
DAQ – Data Acquisition System  
DoD – Department of Defense  
DOE – Department of Energy  
DOT – Department of Transportation  
DSC – Differential Scanning Calorimetry  
F – Fahrenheit  
FI – failure index  
FAA – Federal Aviation Administration  
FEA – Finite Element Analysis  
FEM – Finite Element Method  
FS – factor of safety  
FSAE – Formula SAE  
G – gravitational constant  
JMS – Jayhawk Motorsports  
JMS16C - Jayhawk Motorsports 2016 Combustion  
JMS17C – Jayhawk Motorsports 2017 Combustion  
JMS18C – Jayhawk Motorsports 2018 Combustion  
JMS19C – Jayhawk Motorsports 2019 Combustion  
ksi – kilo-pound per square inch  
KU – Kansas University  
lbf – pound of force  
msi – mega-pound per square inch  
MS – Military Specification  
NIAR – National Institution of Aviation Research  
OEM – Original Equipment Manufacturer  
ORNL - Oak Ridge National Laboratory  
PEMFC – Proton-Exchange Membrane Fuel Cell  
psi – pound per square inch  
PW – plain weave  
RBE – rigid body element  
RTD – room temperature dry

SAE – Society of Automotive Engineers  
SMC – sheet molding compound  
 $T_g$  - glass transition temperature  
TCS – traction control system  
TTC – Tire Testing Consortium  
VBO – Vacuum Bag Only

## 1. Introduction

Automobile racing is an internationally recognized pastime that is stimulating and competitive for organizations of all skill levels. At the collegiate level, FSAE provides a unique opportunity for university students to design, manufacture, and compete a single seat, open-wheeled prototype race vehicle within the constraints of the FSAE Rules [1]. A major contribution to creating a faster car than the competition is the utilization of resources such as advanced materials, analysis software, manufacturing technologies, and data acquisition.

To improve vehicle performance around the track it is desirable to reduce unsprung mass and minimize compliance within the suspension system to maintain grip at the tire. As with any race series but FSAE specifically, time and resources can be limited. The necessity for teams to fundraise or source material donations from sponsors drives the need to utilize simple yet effective designs to meet overall vehicle goals. This thesis documents the development of a laminated upright design that is manufactured from a single modular toolset for utilization at all four corners of the JMS19C vehicle (Figure 1.1).



*Figure 1.1: Jayhawk Motorsports, 2019 Combustion Race Vehicle*

## **1.1. Objectives**

The purpose of this thesis is to document the development of a laminated suspension component that is manufactured from a modular toolset. The upright (otherwise commonly referred to as a spindle or knuckle) is a structure that houses the wheel bearing(s) and hub that connects the outboard suspension linkages together and is located at all four corners of the vehicle. After the suspension and steering geometries are determined, this component is often designed to be manufactured from a metallic material such as aluminum, steel, or titanium. In previous JMS designs, the upright is designed from high strength aluminum and machined using a computer numerical control (CNC) program which can be time consuming, require the manufacturing of secondary fixtures, generate considerable waste material, and require post machining of bearing housing surfaces. The primary structure of the upright is designed using carbon fiber reinforced polymer (CFRP) to improve the manufacturability of the component and to capitalize on the greater strength and stiffness per unit mass of the material.

To allow for adjustability in static tire camber and Ackerman steering geometry the utilization of interchangeable or shim-able mounts were implemented for use in combination with the composite structure. After suspension hard points had been determined based on vehicle level targets the components were modeled using computer aided drafting (CAD) software. The utilization of finite element analysis (FEA) software allowed for the prediction of strain distribution for a given global and localized stacking sequence assigned to the structure with primary considerations being strength, camber compliance contribution to the suspension assembly, and weight.

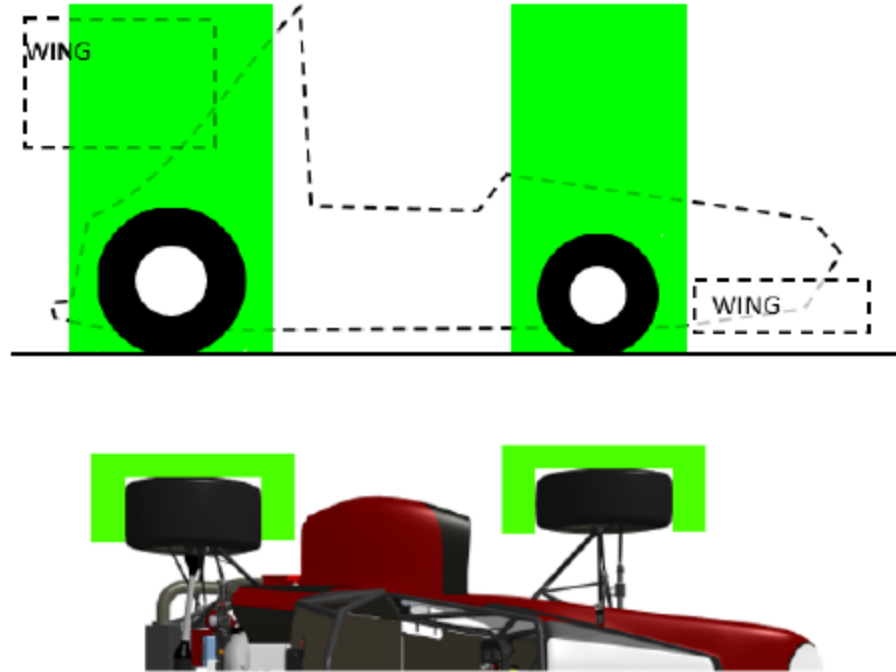
## **1.2. Design Limitations**

The focus of the project is primarily on the performance characteristics of the laminated composite structure and the adjustable mounts interacting therein. FEA was performed only on the primary structure and mounts so interactions from the suspension linkages, braking, and tires are not directly detailed within this paper. Isolated testing of the laminated components using a unilateral load machine were not utilized due to the additional complexity and fabrication time necessary to develop such an apparatus. Instead, strain data was collected from the components using the JMS19C vehicle and compared against the FEA output to quantify the accuracy of the models.

## **1.3. General Requirements of Uprights**

The upright interfaces directly with the suspension linkages, brake caliper, and wheel bearings. Indirectly the upright interfaces with the hub, wheel retention hardware, brake rotor, wheel, and tire. These components set the limitations based on packaging. Thermal limitations were considered based on heat generation from the brake system and its potential negative impact on the composite material.

Upright geometry can take form of what is classified as tall or short knuckle in the automotive industry. This specifically refers to locating the upper ball joint above or below the tire from a side view, respectively. While each has their advantages, the use of a tall knuckle design is implicitly forbidden by FSAE rule T.1.1.2 [1]. This rule does not allow the top 180 degrees of the wheel/tire to be obstructed when viewed from above the wheel (Figure 1.3.1). As a result, the upper ball joint on the JMS19C is located within the wheel. Based on the selection of the Continental C18 tire for use on the JMS19C, the wheel diameter must be 13". This created the overall limiting volume for the upright to reside within the wheel.



*Figure 1.3.1: 2019 FSAE Keep Out Zone [1]*

Additionally, the 2019 FSAE rules in sections T.1.5, T.1.6, T.10.2, T.10.3, and T.10.4 [1] influence the design of the uprights. Overall suspension limitations are liberal based on the rules in section T.1.5. Applicable rules only effect the upright design such that all the suspension mounting points need to be visible, all fasteners used in the design must be critical fasteners (T.10.2 and T.10.3), and spherical bearings must be mounted in double shear or captured by a washer larger than the outside diameter of the spherical bearing (T.1.5.5). T.1.6.4 requires that either the steering rack or upright features steering stops to prevent the wheels and tires from contacting suspension, body, or frame members during dynamic events. Section T.6.11 and T.1.6.12 require steering components to employ critical fasteners and be of double shear or single shear encapsulated configuration. All mounts attached to the primary composite structure are of double shear configuration and the steering rack is utilized to limit wheel rotation.

Section T.10 defines the critical fastener as a hex head or hexagonal recessed drive fasteners that must meet or exceed the rating of SAE Grade 5, Metric Grade 8.8 and/or AN/MS (Army-

Navy/ Military Specification) (T.10.2). Via rule T.10.3 securing fasteners must utilize an acceptable positive locking mechanism such as a properly installed safety wiring, cotter pins, nylon lock nuts (where temperature does not exceed 80 Celsius) or prevailing torque lock nuts. Finally, rule T.10.4. necessitates that a minimum of two full threads shall extend beyond any lock nut. All fastened mounts to the primary structure or connections to the mounts utilize AN Spec hexagonal head hardware with permanent thread deforming lock nuts where available and two or more threads protruding. In connections that utilize a blind hole with threaded insert or riveted nut plate, safety wire is used to prevent the fastener from backing out. Additional limitations are provided within the constraints of the vehicle suspension geometry design and material strength limits.



## 2. Background

This chapter provides basic information on vehicle dynamics, design of suspension geometry, composite materials, and information pertaining to related technologies at the time. Additional information can be found in literature from Milliken, Gillespie, and Blundell. Throughout the thesis, the forces and moments acting on the vehicle are described using a Cartesian coordinate system with the origin located at the vehicles center of gravity (Figure 2.1).

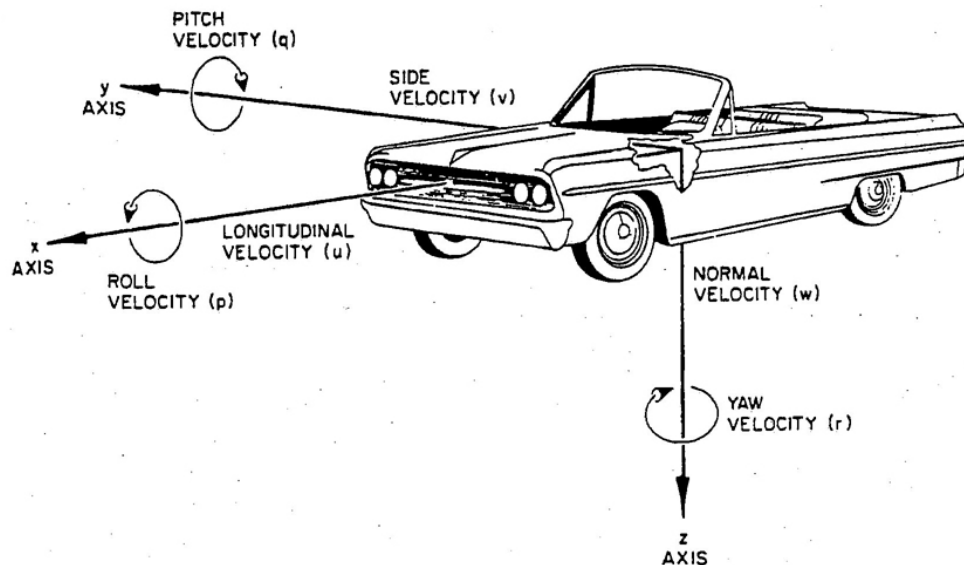


Figure 2.1: SAE Vehicle Dynamics Coordinate System [2]

### 2.1. Vehicle Dynamics

In FSAE as well as other racing series, limits are placed on the power output of the vehicle. In 2019, displacement of the engine for combustion vehicles is limited to 710 cc and power drawn from the accumulator for electric vehicles is 80 kW [1]. To utilize the power most efficiently, it is necessary to minimize the mass of the vehicle while meeting safety, strength, and stiffness requirements. A vehicle with a large power to weight ratio is more capable of accelerating rapidly compared to a vehicle of greater mass and can produce faster lap times.

Designers utilize high-strength and low-density materials such as composites and aluminum to reduce the mass of the components in the vehicle and improve the ability to accelerate.

### **2.1.1. Unsprung Mass**

Most vehicles can be simplified to a two-mass system composed of an unsprung mass and a sprung mass [3]. The sprung masses include the chassis, engine, dampers, electronics, and in the case of JMS19C, the aerodynamic package. The unsprung masses include the wheels, tires, hubs, uprights, brake calipers, rotors, and suspension linkages. Simply stated, anything that is supported by the vehicle's suspension is a sprung mass. Reduction in mass of the uprights aids in increasing the vehicle's ability to accelerate and decelerate in addition to increasing the effectiveness of the springs and dampers.

Reduced mass in the upright is also helpful in improving the yaw moment of inertia of the vehicle,  $I_z$ . This moment of inertia acts about the vertical axis through the vehicles center of gravity (CG) and contributes resistance to changes in direction or rotation. If the vehicle is treated as a single point mass and the moment of inertia formula in its general form is applied (1), a reduction of mass further away from the vehicles CG will reduce the effort required for the vehicle to turn.

$$I = mr^2 \quad (1)$$

Considering that the mass of the upright is in the vicinity of the furthest distance from the CG of the vehicle, a performance gain can be obtained by designing a component that can meet its limit load requirements while minimizing weight.

### **2.1.2. Tires**

Tires provide the means for the vehicle to accelerate in a longitudinal or lateral direction through their interaction with the road surface. This interface is referred to as the tire-road

contact patch. The primary functions of a tire are to support vertical load while dampening against road impacts, generate longitudinal (tractive) forces for accelerating and braking, and generating lateral forces for cornering [4]. All forces applied to the vehicle are created in the tire contact patch except for aerodynamic forces. Figure 2.1.2.1 illustrates the forces, moments, and angles of a tire that influence the performance the vehicle.

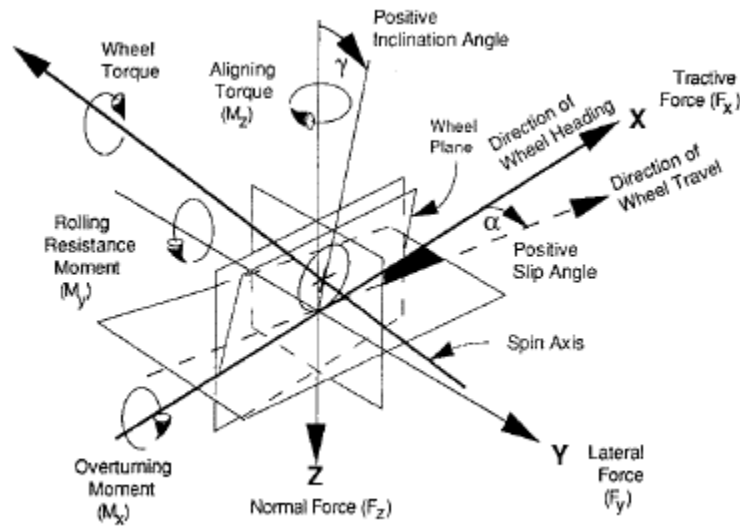


Figure 2.1.2.1: SAE Tire Coordinate System [4]

Tractive force generation is a function of driveline and braking systems. The mechanism of force generation is via the slip ratio of the tire [5]. The longitudinal force is created by the tire rotating at a different rate than its free-rolling speed (no drive or brake force applied) and is expressed as a percentage. For example, if a tire is turning 110 times to cover the same distance as free-rolling tire rotating 100 times the tire has an instantaneous slip ratio of 10% and induces a tractive force to the vehicle. The efficiency of longitudinal force generation is reduced via the rolling resistance moment ( $M_y$ ) due to effects such as frictional resistance from moving components within the driveline and suspension, inertia of rotating components, and

aerodynamic drag. Vehicle systems such as anti-lock brake (ABS) and traction control (TCS) are designed to aid the driver in the management of longitudinal forces.

A vehicle's ability to corner is dependent upon the lateral force generation of the tire. Lateral force generation is a function of slip angle and camber (inclination angle in Figure 2.1.2.1). Slip angle ( $\alpha$ ) is the primary mode of lateral force generation and is measured between the direction of wheel heading and the direction of travel. It is considered positive when the tire is moving to the right as it rolls forward. The driver can change the slip angle of the front tires using the steering wheel to induce a yaw moment on the vehicle via the resultant lateral force of the tire. Slip occurs when the lateral force of a tire tread element overcomes the available friction as it rotates through the tire contact patch. Therefore, lateral force generation due to slip angle is only possible when the vehicle is in motion. Additionally, they are heavily modified by the vertical loads on the tires at a given instant in time.

Vertical loads can vary due to weight transfer of the vehicle from roll and pitch in addition to aerodynamic influence. Camber ( $\gamma$ ) is the angle between the wheel plane and the vertical and is positive as the 'top' of the tire leans outward from the vehicle and contributes a small (but non-negligible) lateral force in the tire. This secondary mechanism of force generation is often referred to as camber thrust and acts in the direction that which the tire is inclined. It is the role of the suspension linkage to regulate the tires lateral forces by controlling the slip and camber angles. Vertical loads on the tire are primarily managed by the calibration of springs and dampers.

### 2.1.3. Suspension Geometry

The geometry of a vehicle's suspension defines how the unsprung mass of a vehicle is attached to the sprung mass. The intention is to control the wheel motion relative to a car body in a single path and may contain camber change, caster change, and toe change [3]. A well-designed suspension should not allow the tire to move fore/aft or laterally relative to the path. The only motion of the tire allowed by the suspension linkage should be up and down against the spring/damper or rotation due to steering input from the driver. Considering a vehicle with independent suspension, the upright is the component that ties all the outboard suspension linkages together.

In three-dimensional space there are three components of linear motion and three components of rotational motion resulting in six total degrees of freedom for a single body. To constrain the upright to limit motion in five degrees of freedom, five tension-compression links are required. The JMS19C utilizes a dual a-arm suspension with pushrods that connect the lower control arm to the spring and damper assembly. Each a-arm is equivalent to two straight links. The fifth degree of freedom is obtained from the tie rod which allows for steering input in the case of the front upright. In the rear suspension configuration, a "toe link" is used to constrain the tires rotational Z degree of freedom.

An upright is designed in one of two general configurations, short or tall. The length of the upright is based on the span of the kingpin axis and vertical position of the upper ball joint relative to the tire. The kingpin axis is a line connecting the upper and lower ball joints that the tire rotates about when the vehicle is steered (as depicted in Figure 2.1.3.1).

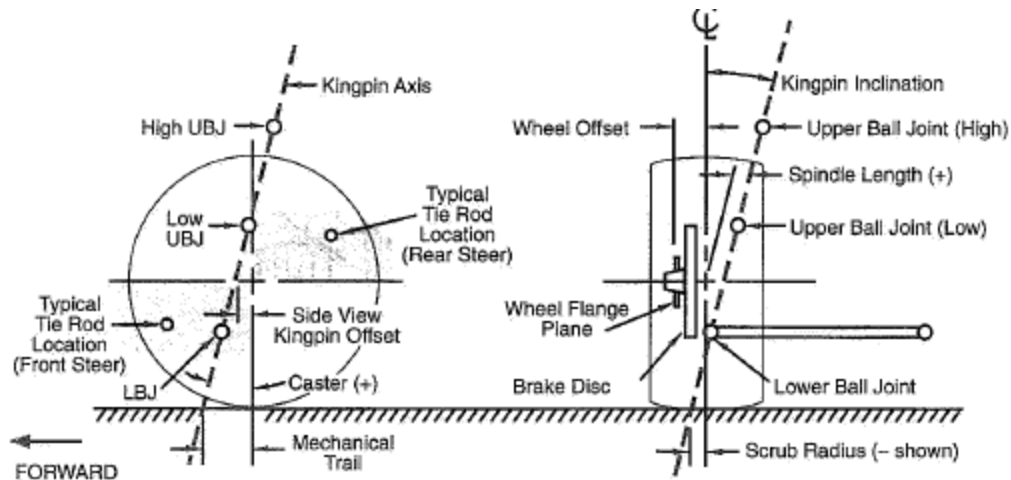


Figure 2.1.3.1: Kingpin Geometry [3]

The tall upright is more common in production automobiles where the upper ball joint can be positioned above the tire. This configuration is also depicted in Figure 2.1.3.1 as the upper ball joint (high) in the side and front views. The ball joint position allows for smaller kingpin angles while maintaining a desirable spindle length and scrub radius. As a result of the larger span, reaction loads are reduced on the upright and in turn lowered through the control arms. The ‘short’ design requires that the entire upright is packaged within the wheel from a side view. This configuration is depicted as the upper ball joint (low) in Figure 2.1.3.1. This design is more common in FSAE vehicles due to rule T.1.1.2 which does not allow for components to exist within the aerodynamic keep out zone (recall Figure 1.3.1). A short upright is often lighter in comparison to its counterpart as it typically requires less volume of material to perform its function. However, it can have less desirable kinematic effects under load in comparison to its alternative by inducing camber change in cornering due to compliance acting through a shorter kingpin axis length.

A secondary steering attribute that is considered during the design of the upright is Ackermann geometry. The front steering linkage dictates whether the wheels will remain

parallel as the wheels are steered away from the straight-ahead position. Ackermann is measured as a percentage and correlates to 100% for parallel, <100% for reverse Ackermann and >100% for Ackermann (or pro-Ackermann) for a given steer angle without input of a static toe angle. This parameter can be designed for reconfigurations given different vehicle performance targets. For example, a track with many small radii, low speed corners would suggest the necessity for a reverse Ackermann geometry to steer the inside front wheel at a greater angle than the outside front. A higher speed course with larger radii turns would not require as much variation in side-to-side wheel slip angle because the front wheels do not need to be steered to as high of a degree. Additionally, the vehicle weight transfer due to body roll unloads the inside tires reducing the vertical force acting within the tire contact patch.

The specific details of the overall suspension design of the vehicle does not fall within the scope of this thesis. However, it is important to note that as the uprights function in conjunction with other suspension elements, they will influence the overall kinematic performance of the vehicle.

## **2.2. Composite Materials**

Early in the design of a component, engineers must consider the benefits and drawbacks of available materials. Composite materials differ from conventional options such as aluminum or steel because they are composed of two or more materials on a macroscopic level to form a subsequent material [6]. These materials demonstrate the best properties of their constituents and often some traits that neither constituent exhibit independently. This principle of combined action improves properties such as strength, stiffness, wear resistance, fatigue life, weight, and thermal insulation. Additionally, composite materials follow an additive manufacturing philosophy when compared to a machined component. The laminate is built or ‘laid up’ using

plies or lamina to create the part. In contrast, a machined component begins as a volume of material that is reduced to its final geometry.

On a fundamental level composite material are composed of two major constituents, the matrix phase and dispersed phase. The matrix phase can be a metal, polymer, or ceramic and allows for an applied load to be transferred between the dispersed phases. Furthermore, the matrix protects from chemical reaction with the environment or surface damage resulting from mechanical abrasion [7]. Variation of the dispersed phase comes about in the shape, distribution, and orientation of the fibers or particles. Common configurations of dispersions include continuous and aligned, discontinuous and aligned, discontinuous and random, or a combination thereof. The strength of a fiber dispersion composite is attributed to fiber length, concentration, and the orientation of the fiber. This configuration of the constituents contributes to the anisotropic and inhomogeneous nature of a composite material as opposed to a metallic material that is homogenous and isotropic on a macroscopic scale.

A composite material achieves a high strength to weight ratio via the configuration of the dispersed phase. These typically fall into particle-reinforced, fiber-reinforced, or structural composites. Structural composites are composed of a composite and homogenous material such as a foam or honeycomb core. Particle reinforced composites have a lower strength than a fiber-reinforced or structural composite due to the interactions of the dispersion-matrix at a molecular level. This is attributed to the matrix carrying most of the applied load in opposition to a fiber-reinforced composite. The strength contribution of the dispersed phase is a function of fiber length to diameter ratio [7]. A greater length to diameter ratio provides better reinforcement due to load shearing into adjacent fibers via the matrix at fiber



extremities. A fiber-reinforced composite is chosen for use in this project due to its greater load carrying capacity.

Continuous and aligned fiber composites are manufactured in a variety of configurations. The fiber architecture of the dispersed phase influences the properties of the composite in addition to the processing [8]. The fiber can be one-dimensional in the form of a unidirectional fiber, two-directional as a woven fiber product, or three-dimensional as a stitched woven stack fiber product. There are a variety of materials available with common types being glass, carbon, and aramid with each possessing their own unique material properties.

A composite's strength is influenced by the elastic behavior of the constituent materials. To quantify the elastic behavior of a composite, consider a unidirectional lamina subject to longitudinal loading (in the direction of the fiber alignment). A cross section of the composite subject to a longitudinal load ( $F_c$ ) is the sum of the load carried by the matrix ( $F_m$ ) and the fibrous phase ( $F_f$ ).

$$F_c = F_m + F_f \quad (2)$$

It is assumed that the bond between the matrix and fiber is near perfect suggesting that the strain experienced by the composite is equal to the fiber strain and matrix strain or an isostrain condition (similar to springs in parallel). The applied load to the composite can be rewritten as the product of stress and cross-sectional area for each constituent acting over the total cross-sectional area. Assuming the phase lengths are all equal the area fractions for each constituent ( $A_m/A_c$  and  $A_f/A_c$ ) are equivalent to volume fractions.

$$\sigma_c = \sigma_m \left( \frac{A_m}{A_c} \right) + \sigma_f \left( \frac{A_f}{A_c} \right) = \sigma_m V_m + \sigma_f V_f \quad (3)$$

Application of the isostrain state with the condition that the deformations of the composite, matrix and fiber all being elastic allows for the substitution of the modulus of elasticity for each

respective component (example:  $\sigma_c/\varepsilon_c = E_c$ ). The resulting equation is commonly referred to as the rule of mixtures and provides an approximation of the longitudinal stiffness of the composite material for a continuous and aligned fiber composite.

$$E_{c,\text{longitudinal}} = E_m V_m + E_f V_f \quad (4)$$

In general, the fibrous phase is brittle, and the matrix phase is ductile. The rule of mixtures demonstrates that the composite stiffness and strength is dependent upon the concentration of longitudinally oriented fibers and increases linearly with the fiber volume fraction.

The longitudinal elastic behavior assumes that the volume fraction of the composite is purely composed of the fiber and matrix phases. However, air or other volatiles can become trapped within the laminate during the manufacturing process that results in micro voids. Micro voids tend to negatively influence the composite material by reducing the consistency of the mechanical properties. Examples include lowering the fatigue resistance and allowing for greater susceptibility to moisture diffusion [8]. A high void content is 2.0% or greater by volume and can be approximated by comparing the theoretical density with the actual density of a material sample. Alternatively, samples can be prepared and processed via American Society for Testing and Materials (ASTM) D3171 to experimentally determine the void volume of the material.

Transverse elastic behavior differs from the longitudinal behavior for a unidirectional continuous fiber lamina. This scenario is not uncommon in practical application of composite materials and occurs when the load is applied perpendicular to the fiber orientation. An approximation for the transverse stiffness ( $E_{c,\text{transverse}}$ ) is derived using the assumption of an isostress condition and is reduced to the following equation [7] where  $E_m$  and  $E_f$  are matrix

and fibrous phase stiffnesses and  $V_m$  and  $V_f$  are matrix and fiber volume fractions, respectively.

$$E_{c,transverse} = \frac{E_m E_f}{(V_m E_f + V_f E_m)} \quad (5)$$

The previous equation demonstrates the high transverse stiffness contribution of the matrix phase in a unidirectional lamina. Despite the lower transverse strength of a unidirectional fiber lamina, it can provide excellent reinforcement properties when combined with other lamina to form a laminate. For this reason, many composite components utilize a cross ply, angle ply, or combination configuration laminate of unidirectional lamina to provide greater strength in structures with various loading conditions.

Laminated composites are not limited to combinations of unidirectional lamina. Biaxial fabrics are woven to provide similar strength and stiffness in the warp (along length of roll) and fill (across width of roll) directions. Woven fabric is not as strong as pure unidirectional fabric due to the lower fiber quantity in direction of load (for a given cross section) and the crimp of fibers at their intersection that is inherent of a woven textile. However, woven fabrics provide better drape qualities and control of fiber orientation in components with complex contours.

The calculation of lamina stiffness is more complicated than the previously mentioned examples for a unidirectional lamina. Stiffness of a lamina or laminate is typically presented in the form of a matrix  $[\bar{Q}]$  and is used to relate in-plane stresses to known in-plane strains [8].

Inversely, the reduced compliance matrix  $[\bar{S}]$  relates in-plane strains to known in-plane stresses.

$$\begin{Bmatrix} \sigma_{xx} \\ \sigma_{yy} \\ \tau_{xy} \end{Bmatrix} = \begin{bmatrix} \bar{Q}_{11} & \bar{Q}_{12} & \bar{Q}_{16} \\ \bar{Q}_{12} & \bar{Q}_{22} & \bar{Q}_{26} \\ \bar{Q}_{16} & \bar{Q}_{26} & \bar{Q}_{66} \end{bmatrix} \begin{Bmatrix} \varepsilon_{xx} \\ \varepsilon_{yy} \\ \gamma_{xy} \end{Bmatrix} = [\bar{Q}] \begin{Bmatrix} \varepsilon_{xx} \\ \varepsilon_{yy} \\ \gamma_{xy} \end{Bmatrix} = [\bar{S}]^{-1} \begin{Bmatrix} \varepsilon_{xx} \\ \varepsilon_{yy} \\ \gamma_{xy} \end{Bmatrix} \quad (6)$$

where various elements of the reduced stiffness matrix are represented as

$$\begin{aligned} \bar{Q}_{11} &= Q_{11} \cos^4 \theta + 2(Q_{12} + 2Q_{66}) \sin^2 \cos^2 \theta + Q_{22} \sin^4 \theta \\ \bar{Q}_{12} &= Q_{12} (\sin^4 \theta + \cos^4 \theta) + (Q_{11} + Q_{22} - 4Q_{66}) \sin^2 \theta \cos^2 \theta \end{aligned}$$

$$\begin{aligned}
\bar{Q}_{22} &= Q_{11}\sin^4\theta + 2(Q_{12} + 2Q_{66})\sin^2\cos^2\theta + Q_{22}\cos^4\theta\bar{Q}_{16} \\
&= (Q_{11} - Q_{12} - 2Q_{66})\sin\theta\cos^3\theta + (Q_{12} - Q_{22} + 2Q_{66})\cos\theta\sin^3\theta \\
\bar{Q}_{26} &= (Q_{11} - Q_{12} - 2Q_{66})\cos\theta\sin^3\theta + (Q_{12} - Q_{22} + 2Q_{66})\sin\theta\cos^3\theta \\
\bar{Q}_{66} &= (Q_{11} + Q_{12} - 2Q_{12} - 2Q_{66})\sin^2\cos^2\theta + Q_{66}(\sin^4\theta + \cos^4\theta)
\end{aligned}$$

and  $\theta$  is the ply alignment angle.

The components of the reduced stiffness matrix defined above are expressed in terms of the properties in the principal material directions that are determined via material testing or approximation from calculations of longitudinal modulus ( $E_{11}$ ), transverse modulus ( $E_{22}$ ), in-plane shear modulus ( $G_{12}$ ), major Poisson's ratio ( $\nu_{12}$ ), and minor Poisson's ratio ( $\nu_{21}$ ). Those coefficients are calculated as follows

$$Q_{11} = \frac{E_{11}}{1 - \nu_{12}\nu_{21}} \quad (7)$$

$$Q_{22} = \frac{E_{22}}{1 - \nu_{12}\nu_{21}} \quad (8)$$

$$Q_{12} = Q_{21} = \frac{\nu_{12}E_{22}}{1 - \nu_{12}\nu_{21}} = \frac{\nu_{21}E_{11}}{1 - \nu_{12}\nu_{21}} \quad (9)$$

$$Q_{66} = G_{12} \quad (10)$$

These relationships are fundamental in the determination of in-plane stresses and strains of each lamina in a thin laminated structure using the classical lamination theory (CLT) [8]. Additionally, the CLT is used to determine the extensional, coupling, and bending stiffness of a laminate. Applied forces and moments are related to midplane strains and curvatures via the following matrix equations.

$$\begin{Bmatrix} N_{xx} \\ N_{yy} \\ N_{xy} \end{Bmatrix} = [A] \begin{Bmatrix} \varepsilon_{xx}^0 \\ \varepsilon_{yy}^0 \\ \gamma_{xy}^0 \end{Bmatrix} + [B] \begin{Bmatrix} k_{xx} \\ k_{yy} \\ k_{xy} \end{Bmatrix} \quad (11)$$

$$\begin{Bmatrix} M_{xx} \\ M_{yy} \\ M_{xy} \end{Bmatrix} = [B] \begin{Bmatrix} \varepsilon_{xx}^0 \\ \varepsilon_{yy}^0 \\ \gamma_{xy}^0 \end{Bmatrix} + [D] \begin{Bmatrix} k_{xx} \\ k_{yy} \\ k_{xy} \end{Bmatrix} \quad (12)$$

Where [A] is the extensional stiffness matrix for the laminate with components denoted in N/m, or lb/in

$$[A] = \begin{bmatrix} A_{11} & A_{12} & A_{16} \\ A_{12} & A_{22} & A_{26} \\ A_{16} & A_{26} & A_{66} \end{bmatrix}$$

[B] is the coupling stiffness matrix for the laminate with components denoted in N or lb.

$$[B] = \begin{bmatrix} B_{11} & B_{12} & B_{16} \\ B_{12} & B_{22} & B_{26} \\ B_{16} & B_{26} & B_{66} \end{bmatrix}$$

[D] is the bending stiffness matrix for the laminate with components denoted in N-m or lb-in.

$$[D] = \begin{bmatrix} D_{11} & D_{12} & D_{16} \\ D_{12} & D_{22} & D_{26} \\ D_{16} & D_{26} & D_{66} \end{bmatrix}$$

The elements of each respective stiffness matrix are calculated as follows

$$A_{mn} = \sum_{j=1}^N (\bar{Q}_{mn})_j (h_j - h_{j-1}) \quad (13)$$

$$B_{mn} = \frac{1}{2} \sum_{j=1}^N (\bar{Q}_{mn})_j (h_j^2 - h_{j-1}^2) \quad (14)$$

$$D_{mn} = \frac{1}{3} \sum_{j=1}^N (\bar{Q}_{mn})_j (h_j^3 - h_{j-1}^3) \quad (15)$$

such that N is the total number of plies in the laminate,  $(\bar{Q}_{mn})_j$  are the elements in the reduced stiffness matrix of the  $j$ th ply,  $h_{j-1}$  is the distance from the laminate midplane to the top of the  $j$ th ply and  $h_j$  is the distance from the midplane to the bottom of the  $j$ th ply.

The previous derivation for the various stiffness matrices are the basis of the in-plane failure

approximation provided by the finite element analyses that are covered in greater detail in Chapter 5.

### **2.3. Available Technologies**

This section highlights the application of composite materials in design within the automotive industry. Background information into the design basis for the composite upright is also provided from a previous JMS FSAE project [9].

#### **2.3.1. Research and Development within Transportation Sector**

The use of composite materials extends beyond automotive racing and aerospace sectors. Automotive Original Equipment Manufacturers (OEM) have adopted the use of these materials to increase fuel economy through reduction of mass in body and chassis components in addition to simplified assembly by consolidating parts. The United States Department of Energy (DOE) founded the FreedomCAR program that partnered with OEM in 1998 to develop a low-cost automotive grade carbon fiber [10]. The goal of the material was to have a cost of \$3-\$5/pound, tensile strength of 250 kilo-pound per square inch (ksi), modulus of 24.9 mega-pound per square inch (msi), and 1% strain to failure. Additionally, FreedomCAR sought to build confidence and experience with CFRP design and develop reliable joining, testing, and non-destructive evaluation methods to maintain similar safety and performance parameters for conventional vehicles. Oak Ridge National Laboratory (ORNL) is the lead laboratory for the DOE's carbon fiber research because it is equipped to develop, test, and validate improved precursors and conversion technology. Additionally, ORNL can perform measurement, characterization, and crash energy testing on composite structures.

Through their research ORNL found a reduction in cost of carbon fiber via new processing technologies [10]. The first notable discovery was microwave-assisted plasma systems for carbonization of the carbon fiber that resulted in a rapid, controlled carbonization of pre-oxidized precursor. The second notable discovery was a low temperature plasma processes for oxidization of the carbon fiber. This is relevant in reaching the cost goal of automotive grade carbon fiber because the oxidization was the most expensive and time-consuming step in the carbon fiber conversion process. Another contributor to reaching the cost target is the production of carbon fiber from lignin. Lignin is a chemical by-product of the papermaking process that is available nationwide in large supply and could be purified of sulfur and organic contaminants and melt spun into precursor. Aside from material development, issues related to manufacturing, supply chain, and ecological issues must be addressed.

Other challenges with widescale adoption of carbon fiber in automotive production is the creation of short cycle-time, high yield, molding processes, long term stability in price and supply of material, demonstration of affordable recycling, recovery, and repair methods [10]. Carbon fiber's greatest competition in lightweight automotive materials are aluminum and magnesium due to their proven track record in design, fabrication, assembly, and recycling. In 2006 the Aluminum Association reported that aluminum passed iron as the second most common automotive material at an average of 317 pounds per vehicle in North America. The International Magnesium Association forecasted that magnesium use will grow consistently 5%-7% from the current 10-13 pounds per vehicle.

If carbon fiber is to be feasible for mass adoption, the issue of recycling and reclamation must be addressed [10]. While regulations currently do not exist in North America, the European Union required more than 85% of all vehicle weight to be recycled as of 2006. If the utilized

mass of magnesium were to be traded out with carbon fiber while assuming scrap rates of at the time it would leave 44,463 tons of scrap to be addressed annually [10]. Adherent Technologies of Albuquerque, NM and Argonne National Laboratories made notable efforts to address the problem of recycling scrap carbon fiber. Adherent utilized a catalytic depolymerization process applicable to carbon fiber thermoset resin that could reclaim more than 90% of the fibers and suffered only 9% reduction in strength [10]. Argonne National Laboratory utilized a single-step pyrolytic process to recover carbon fiber in panels and thermoplastic/thermoset composites with recovered fibers that were similar in diameter, density, and morphology as the original fibers. Argonne National Laboratory believed the process to be economically viable based on the recovered fiber value of \$1.50/pound.

Through collaboration of OEM and the FreedomCAR program, notable technical and commercial achievements such as the carbon fiber tie-rod for heavy-duty trucks (Delphi Corporation), carbon fiber recovery from CFRP scrap, melt-spun carbon fiber precursor from lignin feedstock, technical improvement of the powdered pre-form General Motors fiberglass truck bed and development of carbon/carbon bipolar plates for proton-exchange membrane fuel cells (PEMFC) were made possible [10]. Other partnerships were formed between automotive manufacturers, research laboratories, and material suppliers demonstrated the basis of carbon fiber use in automotive suspension component design such as the hybrid carbon fiber/aluminum suspension knuckle (Figure 2.3.1.1) and the composite tie-knuckle blade (Figure 2.3.1.2).





*Figure 2.3.1.1: Hybrid Carbon Fiber/Aluminum Suspension Knuckle [11]*

The hybrid carbon fiber/aluminum suspension knuckle was a study performed by Saint Jean Industries and Hexcel to implement a prepreg patch to an existing aluminum geometry in order to increase the stiffness compared to a full aluminum version [11]. The design of this component desired the stiffness of cast iron but maintaining the weight of aluminum while upholding a relatively short production time. Saint Jean Industries was able to accomplish their goal by using a HexPly unidirectional M77 snap-cure epoxy prepreg patch adhered to the aluminum using Hexcel fast-curing Redux 677 film adhesive and a high-volume compression molding process. The added benefit of using film adhesive with the aluminum knuckle is preventing direct contact of carbon fiber and aluminum, thus reducing the risk of galvanic corrosion. The patch could be placed and cured at 150 degrees Celcius in less than two minutes enabling for the target production of 15,000,000 parts/year to be achieved while increasing the part stiffness 26% over baseline.

Another notable development in lightweight automobile suspension components is the collaboration between Ford Motor Company, Warwick Manufacturing Group, Gestamp, and GRM Consulting. This component was developed over a two year timespan with the goals of a 50% weight reduction compared to its steel counterpart, a sub five-minute cycle time, and a 25,000 part/year production rate [12]. At conception, the part was designed from a single material sheet moulding compound (SMC). Through material testing they found that the loading requirements could not be met and that longer cure times would be required. As a result, a co-molding SMC with layers of prepreg could meet the mechanical requirements of the component and allow for a more advanced geometry. Ultimately, the product could be manufactured by pressing pre-cut prepreg material into a die to generate the desired shape. The prepreg would be transferred to a compression molding press where it is cured with SMC resin composed of 53% weight fraction 15k filament count carbon. The largest challenge that was discovered over the two year course was remaining within the cost objective of the project.



*Figure 2.3.1.2: Composite Knuckle-Tie Blade [12]*

In the realm of FSAE, most teams continue to use aluminum or steel for the design of their uprights. In 2016 JMS developed a full CFRP rear upright prototype that was tested on

the JMS16C. Once the design was validated, it was implemented on the JMS17C. The composite design sought to reduce weight over a full aluminum design, eliminate any post-machining of the components, save manufacturing burden on CNC equipment, and maintain stiffness of the aluminum upright design [9]. The effort in the design of a composite upright set the precedence for the uprights and tooling for the JMS19C.

### **3. General Design of Uprights**

This section covers the general design of the front and rear composite uprights developed in this project. The main topics covered are previous JMS designs, the geometry of the 2019 uprights, and features of the modular tooling. Laminate design for the composite structures is detailed in the chapter pertaining to analysis. Engineering drawings for the front and rear uprights developed in this thesis are available in Appendix A: Left Front and Left Rear Engineering Drawings.

#### **3.1. Design Requirements**

The primary objectives of the project are to develop a modular tooling set to produce four unique composite components that require no post machining operations, reduce weight in comparison to the full CNC aluminum design, develop a finite element model to maximize the efficiency of the laminate, allowing for tire camber and Ackermann steering adjustment at the upright while complying with all applicable FSAE rules, and meeting JMS19C static and dynamic design parameters.

#### **3.2. Upright Design**

Provided that the design of the uprights operated with the entirety of the JMS19C vehicle, some aspects of legacy designs were conserved from previous years. This helped to meet the goals of the project under time and resource constraints while operating in parallel to the overall goals and milestones of the JMS 2019 team.

Primary design consideration includes the location and forces of the upright to the suspension linkages from the hub. These limit loads are determined using force and moment balance matrices for the entire suspension assembly and are applied directly to the composite upright in the finite element analysis for the structures.

### 3.2.1. Legacy JMS Upright Designs

The original full composite rear upright prototype was implemented on the JMS17C/JMS18C (Figure 3.2.1.1) and sought to simplify the manufacturing of the component, reduce manufacturing burden on CNC equipment, reduce weight in comparison to a full aluminum design, and maintain stiffness of the aluminum upright design.



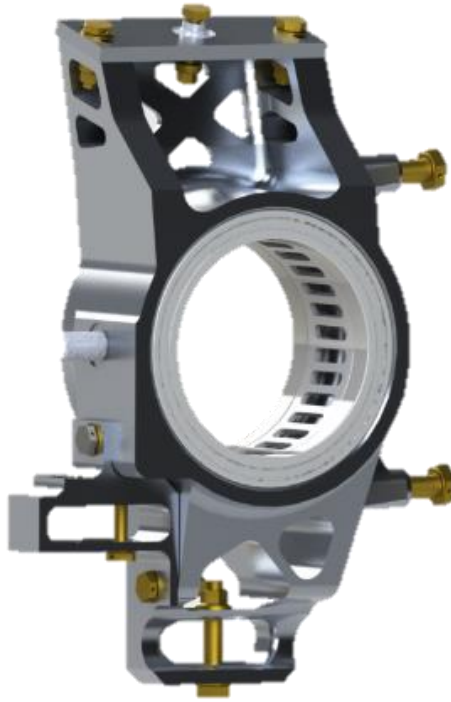
*Figure 3.2.1.1: JMS Full Composite Rear Upright*

The full carbon design had a manufactured weight of 0.70 lb compared to its aluminum counterpart at 2.05 lbs reducing component weight by 65.9% while maintaining the same corner stiffness. The lamination process was similar in duration to CNC time at around 14 hours/part but did not require any CNC machining time once tooling was manufactured. The upright tooling assured proper feature alignment that could fall out of tolerance due to setup changes on the CNC mill and turning of bearing housing dimensions on a lathe.

Adjustability of the rear tire camber was possible using shims between the upper ball joint and the outer control arm. If this would be implemented at the front upright, the adjustment of

camber would simultaneously change the kingpin inclination angle as designed which is undesirable to maintain suspension parameters. Alternatively, it is preferred to adjust tire camber angle at the upright without directly influencing characteristics such as scrub radius and kingpin angle. Ackermann steering is not a parameter of concern for the rear suspension geometry therefore adjustable mating points were not necessary in the full CFRP design. Additionally, dynamic toe could be controlled via inboard adjustment of the control link in turn simplifying the design of the full CFRP design.

The JMS18C front suspension utilized a full aluminum upright design. This configuration had a weight of 2.05 lb and allowed for camber angle, Ackermann geometry, and caster angle adjustment at the upright while maintaining a minimal amount of compliance at maximum lateral load (Figure 3.2.1.2). Moreover, the design and analysis were much more straightforward with an isotropic material which allowed for improvements to be made to the steering geometry and hubs for the 2018 vehicle.

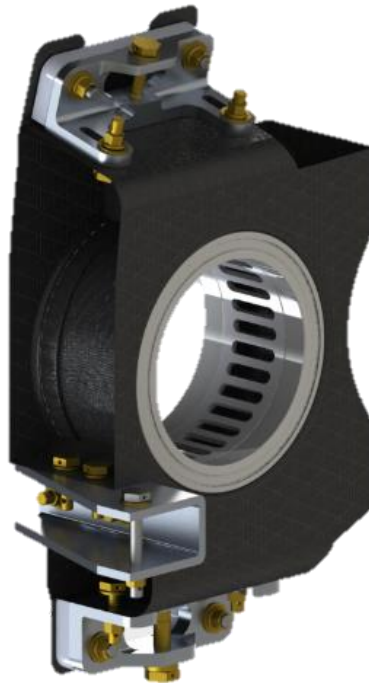


*Figure 3.2.1.2: JMS 2018 Front Upright*

Many teams tend to choose a CNC aluminum or welded steel configuration to simplify the design of the upright while complying with FSAE rules, overall team goals, and vehicle suspension kinematic targets. While the performance of the machined CNC design meets the goals of the subsystem, the manufacturing complexity requires the use of multiple CNC setups and precise tolerances which would make the upright one of the most difficult parts on the car to manufacture. In recent years some teams will partner with industry to produce additive manufacturing (AM) titanium uprights. However, an AM upright would require post-machining and a very high implied cost to meet the component requirements. This fell outside of the goals of the 2019 design as it would rely on outside manufacturing and potentially impact the timeline of vehicle completion for validation testing.

### 3.2.2. New JMS Upright Design

The new upright designs developed in this thesis (Figure 3.2.2.1 and Figure 3.2.2.2) sought to utilize the same tool set to manufacture all four unique primary composite structures. In comparison to the CNC aluminum upright, the tooling and aluminum mounts from the 2019 design are simple enough to be manufactured with the resources available on the Kansas University (KU) campus such as manual mills, manual lathes, composite oven, autoclave, and CNC mill. Synonymous manufacturing of the primary composite structure was made possible by designing the hubs to share the same bearing shaft diameter and spacing. As a result, the same mandrels could be used to form the housing features within the front and rear uprights producing a bearing surface that requires no post machining.



*Figure 3.2.2.1: JMS 2019 Front Upright*



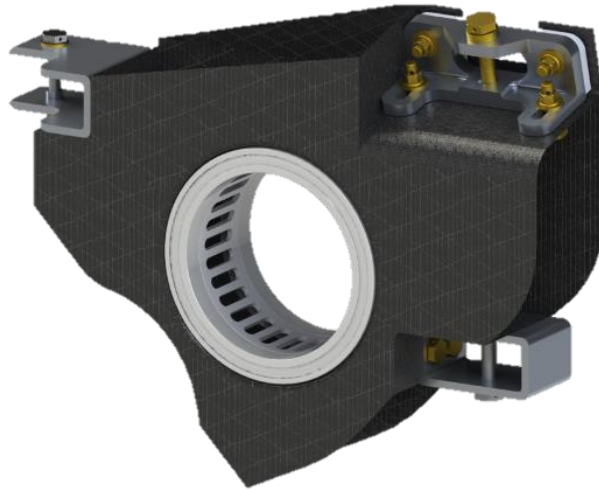


Figure 3.2.2.2: JMS 2019 Rear Upright

Research and analysis were performed on the wheel bearings from SKF coupled with legacy hub design to determine that it was the most effective option available off the shelf. At the time of design there were no other available options with less mass that can support the radial and axial loads acting on the bearings. Calculations from Shigley's mechanical design textbook [13] provide the means to determine the equivalent radial load ( $F_e$ ) of the bearing and catalog load rating ( $C_{10}$ ) based on the requirements of the vehicle.

$$C_{10} = F_D \left( \frac{L_D n_D 60}{L_R n_R 60} \right)^{\frac{1}{a}} \quad (16)$$

where  $F_D$  is desired radial load (lbf),  $L_D$  is desired life (hours),  $n_D$  is rating speed (revolutions/minute),  $L_R$  is rating life (hours),  $n_R$  is desired speed (revolutions/minute), and  $a$  is a dimensionless constant which is equal to three for ball bearings. In this instance,  $F_D$  is substituted for  $F_e$ , or equivalent radial load, as the wheel bearings experience simultaneous axial and radial loading. The equivalent radial load of the bearings can be determined via the following equation.

$$F_e = X_i V F_r + Y_i F_a \quad (17)$$

$$\text{where } i = 1 \text{ when } \frac{F_a}{VF_r} \leq e \text{ and } i = 2 \text{ when } \frac{F_a}{VF_r} > e$$

and  $F_r$  is radial load (lbf),  $F_a$  is axial load (lbf),  $V$  is a dimensionless constant equal to one when the bearings are configured such that the outer ring is fixed, and the inner ring rotates. Table 11-1 (13) provides the means to determine the value of  $e$  (0.38) using the ratio of  $\frac{F_a}{C_0}$  (0.28). This gives the values of  $X_2 = 0.56$  and  $Y_2 = 1.15$  to substitute back into equation 17 to solve for the equivalent radial load,  $F_e$ , of 993.28 lbf under the combined limit loads of  $F_r = 443.00$  lbf and  $F_a = 648.00$  lbf.

Assuming a maximum vehicle speed of 80 miles/hour, a loaded tire diameter of 17.94",  $n_D$  is equivalent to 1497.34 revolutions/minute. A design life,  $L_D$ , of 1000 hours is deemed acceptable for a race vehicle. Taking the equivalent radial load,  $F_e$ , of 993.28 lbf, and the SKF rating life of  $10^6$  revolutions =  $L_R n_R 60$  (13), the catalog rating [13],  $C_{10}$  can be determined to be 4452.94 lbf (per equation 17). The basic static load rating ( $C_0$ ) of the SKF 61815-2RS1 is 2428.00 lbf [14] therefore two of the bearings are required per hub to meet limit load requirements of the vehicle.

The ability to adjust camber angle at the upright is possible via aluminum mounts that can translate about the inclined surface of the composite. These mounts coupled with drop-in shims of various thickness between the mount and upright allow for adjustment of camber angle for a desired vehicle setup. The camber shims were designed from aluminum sheet to be manufactured using a waterjet cutting machine and are interchangeable from front to rear for camber angle adjustment in increments as low as 0.1 degree to 0.5 degree per shim (Figure 3.2.2.3) and is demonstrated as an assembly later in this section.



*Figure 3.2.2.3: Drop-In Shim*

Primary design requirements of the mounts necessitated that the spherical bearings be retained in a double shear configuration (T.1.5.5 [1]) via a single blind fastener threaded into a steel insert that is locked in place using safety wire (T.10.3 [1]). The spherical bearings are oriented with the fastener axis inclined from vertical to allow for the upright to rotate throughout the maximum steer angles. The outboard vertical surface of the mount must allow pass through of the control arm to accommodate suspension geometry design and retain the camber shims. The horizontal region of the mount must allow for the geometry to translate relative to the composite due to camber adjustment and secure the assembly together while shearing applied stresses into the laminate. The upper and lower ball joint mount geometry was modeled with consideration of the limit steering angles at full damper compression and rebound to prevent binding of the suspension linkage (T.1.6.4 [1]). For simplicity of the prototypes, two similar mount designs were utilized that are interchangeable between front and rear uprights. To meet project milestones, the mounts are designed for manufacture on a three-axis CNC mill. Preliminary stress analysis was performed in Microsoft Excel using the maximum ball joint forces to determine minimum flange thicknesses, edge distances, and fastener diameters to drive the CAD modeling of the mounts. Material yield strengths for the fasteners and ball joint mounts

were chosen over ultimate strength to provide conservative factor of safety estimates. Ball joint flange thicknesses and edge distances were analyzed based upon edge shearing of the mount (purely in lateral forces) and bearing stresses (via magnitude of lateral and longitudinal magnitude forces). Fastener forces for the ball joint interface and aluminum mount to composite upright were analyzed separately. Ball joint fastener strengths were evaluated in shear using the magnitude of vehicle lateral and longitudinal forces. Fasteners to constrain the aluminum mounts to the composite upright were evaluated for axial and shear stress in the horizontal and vertical orientations.



*Figure 3.2.2.4: Front Upright Upper Ball Joint Mount Assembly with Shims*

By comparison, the lower load bearing capacity of the front upper ball joint of the front upright necessitated a structure suitable for an AN-3 (3/16" diameter) bolt attachment while the higher load bearing capacity of the lower ball joint of the front upright and upper ball joint of the rear upright shared a similar load carrying capacity through a AN-4 (1/4" diameter) bolt. The machined mounts were designed from 2024 aluminum to take advantage of the retention of strength at elevated operating temperatures in comparison to a six or seven series aluminum. This consideration is important due to the heat generation from the braking system and is addressed in greater detail in the following chapter. 2024 aluminum has an

ultimate tensile strength that is lower than 7075 series by 12.9 ksi or 16% at room temperature [15]. However, at maximum operating temperature (300°F) of the component the 2024 series aluminum experiences a strength loss of 22% opposed to the 7075 series that loses 63% of its strength (Figure 3.2.2.5) [15]. Stress analysis of the mounts were performed using yield strength of the material at maximum operating temperatures at all limit load cases in an FEA program.

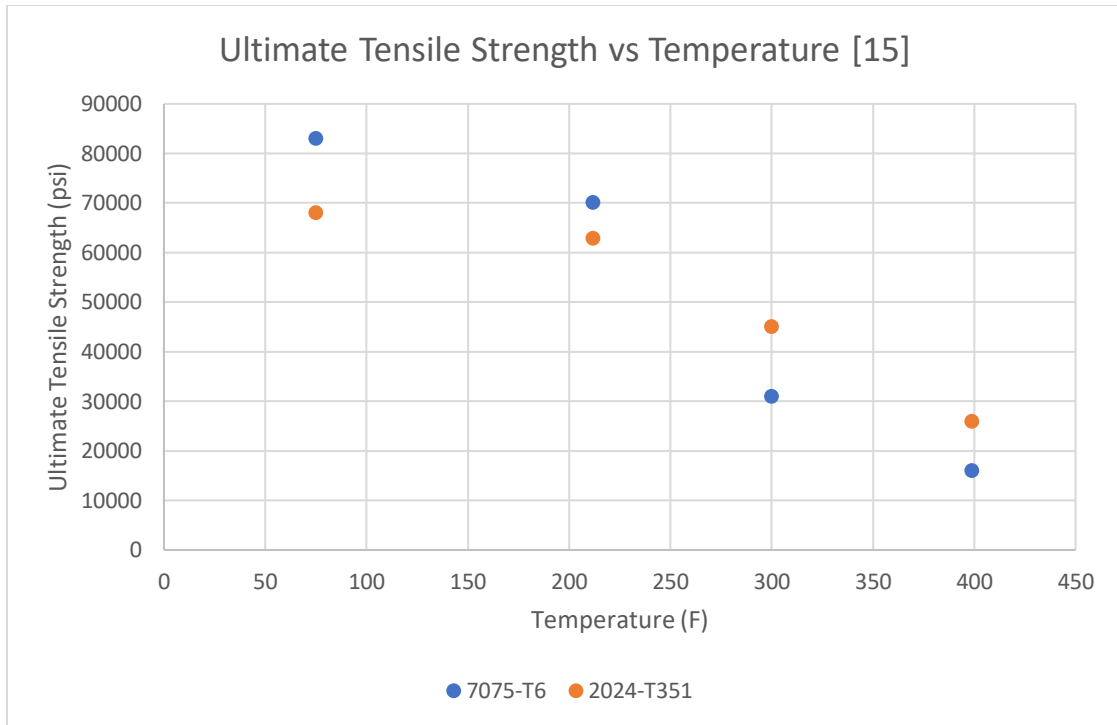
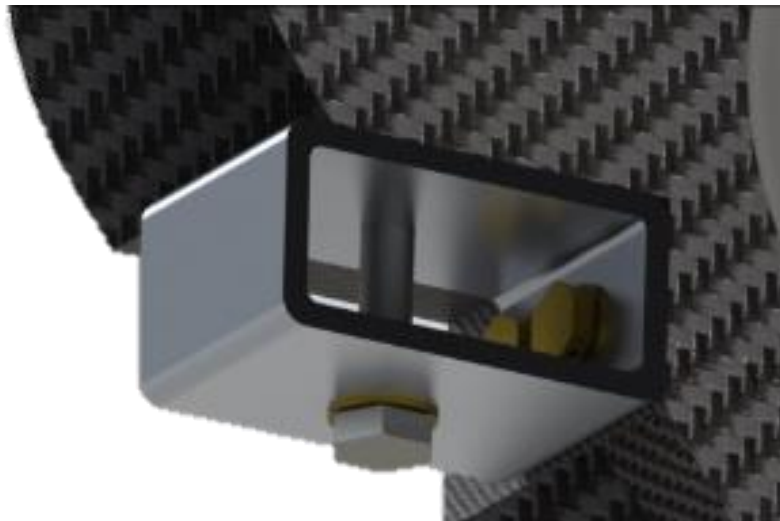


Figure 3.2.2.5: Ultimate Tensile Strength vs Temperature of a Two and Seven Series Aluminum

Sharing of the front lower and rear upper mount design is permissible for meeting the load carrying capacity, camber adjustment, and rapid build timeline while minimizing weight and compliance in the design of these components. The steer/toe and rear lower ball joint mounts were designed for simplicity and swift manufacturing. A rear tire typically does not receive intended steering input unless the vehicle has a dynamic toe rear steer designed into its geometry or a rear mount steering input. For the JMS19C, the rear upright does not have the requirement to

intentionally rotate about its kingpin axis. As a result, the lower ball joint of the rear suspension can be retained using a simple closed double shear mount (Figure 3.2.2.6).



*Figure 3.2.2.6: Rear Upright Lower Ball Joint Mount*

The interchangeable steer and fixed mounts are designed for manufacture using manual operated machine shop equipment with minimal operations. Machined mounts were chosen opposed to bonded composite or integral mounts to eliminate any chance of adhesive failure and simplify the composite manufacturing process for the prototype. The JMS full composite upright design utilized a bonded toe link that was successful during implementation on the 2016 and 2017 vehicles but would exhibit failure on the 2018 due to the increased torque production of the forced induction powertrain. To ensure reliability for the 2019 vehicle, fastened aluminum mounts are implemented to meet the adjustability requirements of Ackermann steering geometry, tire camber adjustment, weight reduction compared to full aluminum uprights, and rapid manufacturing. Three configurations of interchangeable steering mounts were designed and manufactured to meet the design parameters of 80%, 100%, and 110% Ackermann geometry (Figure 3.2.2.7).



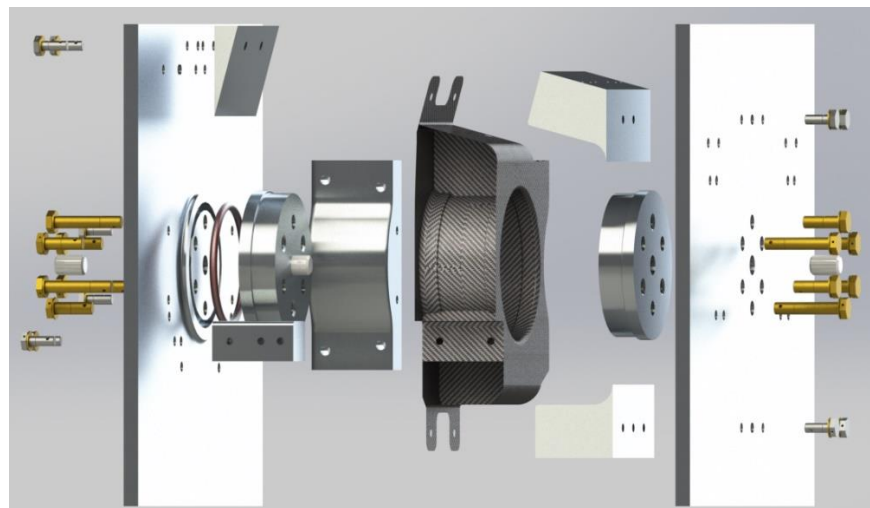
*Figure 3.2.2.7: 100% Ackermann Steering Mount*

Simplicity of the fixed mount designs is met by utilizing a common six series aluminum extrusion as a basis for geometry of the steering, toe, and rear lower ball joint mounts. Each of the mounts could be manufactured from start to finish in less than an hour.

Despite the integration of fastened aluminum mounts to the composite structure the design weight of the front upright allowed for a weight reduction of 44.9% (2.05 lbs down to 1.13 lbs) compared to the 2018 design and a reduction of 54.9% (2.51 lbs down to 1.13 lbs) compared to the 2017 design. The rear suspension geometry of the 2019 vehicle changed significantly from the 2017 or 2018 design and necessitated a higher load capacity structure due to its shorter span of kingpin axis. The 2019 rear upright had a design weight of 1.64 lbs (increase from .70 lb in 2017) and gained 134.3% from the 2017/2018 design. However, the 2019 rear composite upright had a weight decrease of 20.0% (from 2.05 lb) in comparison to the full aluminum 2016 design. While the weight reduction of the 2019 upright designs (compared to full aluminum) were advantageous for meeting vehicle performance goals, the increase in manufacturability justified the minor increase in weight of the rear uprights (compared to full CFRP) to accommodate the aggressive aerodynamic packaging and resulting higher load capacity rear suspension linkage.

### 3.3. Modular Tool

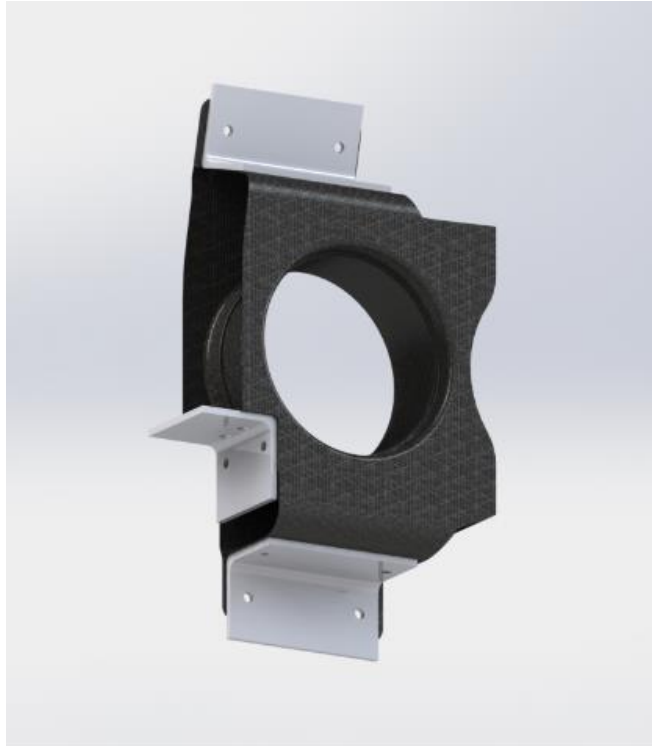
The key development in this project is a modular toolset that can produce all four uprights. The wheel bearing housing is formed during the initial composite cure and does not require post machining once removed from the tool. Additionally, the features that interface with the ball joints, tie rod linkages, and brake caliper are formed with reconfigurable mandrels that function as drill guides to precisely locate fasteners during the assembly of the components. An example of the front left upright configuration is presented in Figure 3.3.1.



*Figure 3.3.1: Tool Configuration for Left Front Upright*

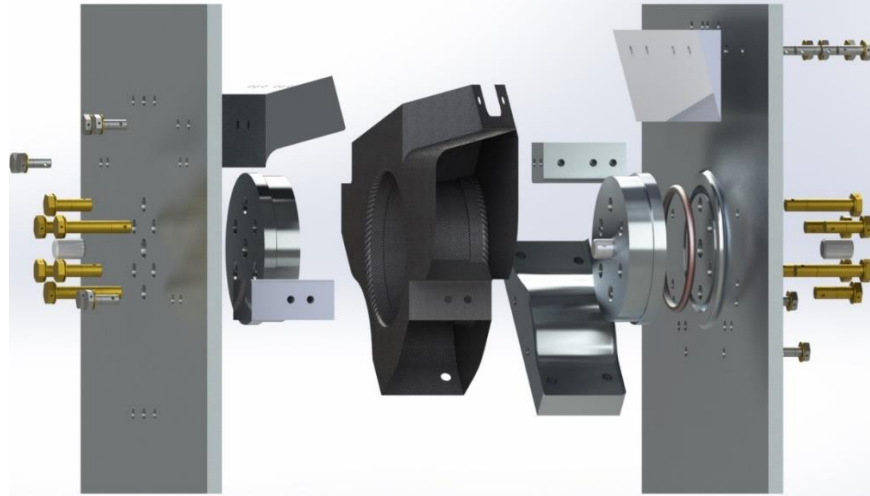
After the first cure is completed, the part is removed for trimming and local composite ply addition. The part is cured a second time and placed back into the tool for drilling. Secondary fixtures are utilized to finish the drilling operation of the parts. They are designed from extruded angled aluminum for low cost and quick manufacturing on a manual mill. A rendering to display the utilization of the secondary drill fixtures for the front upright is displayed in Figure 3.3.2 (sans hardware).





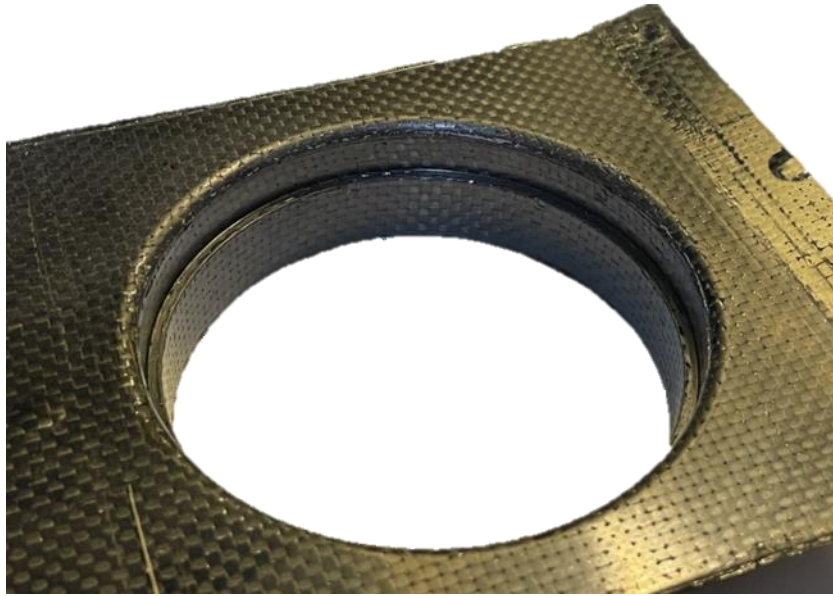
*Figure 3.3.2: Secondary Drill Fixtures for Front Upright*

A secondary advantage of the reconfigurable tooling is that the base plates can be remanufactured in later years with new locations for steering, upper and lower ball joint pickup points. The bearing size and spacing could be increased or decreased if the hub design is altered. If a larger brake rotor is desired the caliper mandrel may be relocated as well. This functions under the assumption that similar incoming angles of the control arms are maintained from year to year such that the operating angle of the spherical ball bearings are not exceeded. However, mandrels can be relocated or interchanged to achieve a desired suspension geometry. Figure 3.3.3 demonstrates the reconfiguration of the tooling to produce a different component that is suitable for the rear suspension geometry.



*Figure 3.3.3: Tool Configuration for Left Rear Upright*

To obtain the fit specified for the wheel bearings, the linear expansion of the aluminum mandrel up to cure temperature and the composite housing diameter change due to temperature fluctuation must be calculated and experimentally verified. A proper fit for the SKF 61815-2RS1 bearing necessitates a housing diameter tolerance of  $+0.0000''/-0.0008''$  on an outside diameter of  $3.7400''$ . The bearing mandrel was designed with an initial outer diameter of  $3.7300''$ . A sample of composite was manufactured to verify that the final product would have a housing diameter within the specification for bearing fit (Figure 3.3.4). The bearing mandrel was machined incrementally on a lathe after each sample until the cured housing diameter met the required tolerance.



*Figure 3.3.4: Bearing Housing Sample*

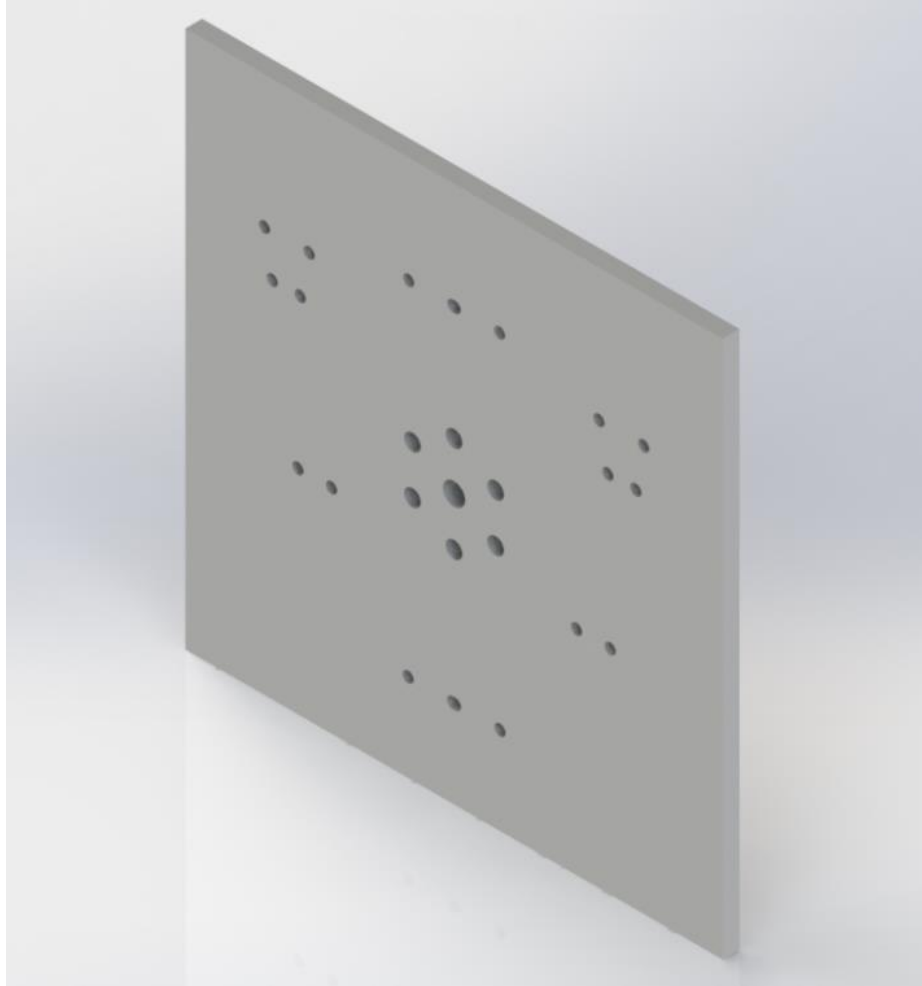
The final outer diameter of the bearing housing mandrel was 3.7260” which would expand to a diameter of 3.7393” at the composite cure temperature of 350°F. Considering the negative coefficient of thermal expansion (CTE) of the carbon (-0.3 ppm/°F) the diameter of the housing expands another 0.0003” after cooling from 350°F down to 70°F which gives a final diameter of 3.7396” and is within the fit tolerance for the bearing housing. Additionally, any temperature fluctuation of the composite structure due to heat generation from the braking system will maintain a housing diameter within the fit tolerance of the bearings.

In retrospect, the modularity of the tooling could have been improved by machining the radiused transition into the bearing mandrel (shown in Figure 3.3.5). This would allow for simplification of the base plates that locate the additional mandrels for the pickup points and brake caliper (Figure 3.3.6).



*Figure 3.3.5: Ideal Bearing Mandrel Geometry*

The simplified base plates in comparison to what was manufactured (Figure 3.3.1 and Figure 3.3.3) would allow for a lower cost and easier manufacturing effort if the upright design were to be iterated multiple times throughout vehicle development. The base plate would be manufactured on a machine as simple as a drill press to allow for repositioning of any of the suspension pickup points, changing of the brake caliper location, or accommodating for a different diameter of wheel bearing. Not only is the initial cost of the part much less expensive than a fully aluminum CNC structure, but the cost to change upright geometry is lower.



*Figure 3.3.6: Ideal Base Plate Geometry*

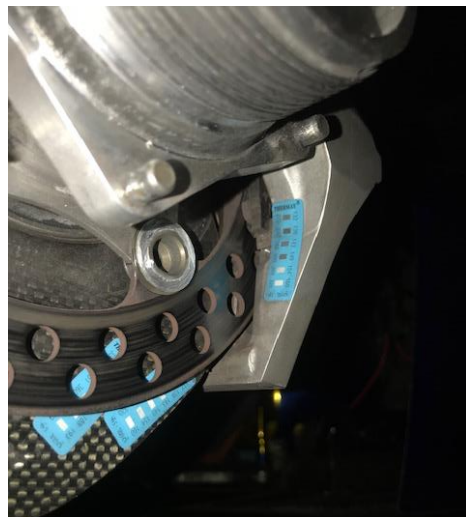
Additional improvements to the 2019 upright design would be achieved by manufacturing the ball joint, steering, and toe-link mounts from carbon fiber to be fastened to the primary structure. This would allow for additional weight reduction and the ability to adjust camber and caster angle at the upright with interchangeable upper and lower ball joint mounts.

## 4. Materials

When designing any component, it is critical to consider the operating environment and its effect on materials and their properties. The biggest factor in the choice of composite material for these components aside from strength and stiffness was the glass transition temperature ( $T_g$ ). This chapter details the methodology utilized in material selection for the project.

### 4.1. Material Selection

Due to the nature of environmental exposure that the uprights experience, physical testing was performed to determine the maximum expected operating temperature of the front and rear upright. JMS2017C was equipped with irreversible temperature indicating labels on the front and rear brake caliper and upright to record maximum operating temperatures (Figure 4.1.1). Additionally, the on-board data acquisition (DAQ) in conjunction with infrared sensors provided the means to record instantaneous temperature of the rotor over time (Figure 4.1.2). During the test, the vehicle was driven on a course with short straightaways and tight corners for a duration equivalent to half of an endurance event (~10 minutes), the point in which a driver change occurs.



*Figure 4.1.1: Temperature Indicating Labels on Rear Upright and Caliper*

		Park and Ride - Purple Track, Park and Ride - Purple Track
		None, JMS17C
		9/22/2018, Heat Transfer Due to Braking
		1:55:43 PM,
Brake Pressure Front [kPa]	Min	-15
	Max	2679
	Avg	156
Brake Pressure Rear [kPa]	Min	-9
	Max	3577
	Avg	256
Brake Temp Front [°C]	Min	-1
	Max	320
	Avg	152
	Std Dev	97
Brake Temp Rear [°C]	Min	-1
	Max	311
	Avg	152
	Std Dev	90

Figure 4.1.2: DAQ Data from JMS17C

Data from the DAQ indicated that the front brake rotors peaked at 606°F with an average temperature of 306°F. The rear brake rotors reached a maximum temperature of 592°F with an average of 306°F. After three minutes of driving the rotors appeared to reach their range of operational temperature. The data suggests that on a short straightaway course with tight corners, the rotors would spend approximately half the time between 473°F-518°F (front) and 446°F-518°F (rear). Despite the brake rotors reaching a temperature well above the  $T_g$  of the composite, the temperature indicating labels did not record a value greater than 300°F. This value of 300°F was recorded at the label located on the rear brake caliper. The labels located at the front and rear upright did not record a value greater than the minimum of the range at 270°F.

#### 4.1.1. Glass Transition vs Strength and Stiffness

Glass transition temperature was the first characteristic considered in CFRP material selection next to strength and stiffness.  $T_g$  is the temperature at which the thermoset containing the fiber softens from a rigid to compliant state. The  $T_g$  is not a single value but a temperature range such that mobility of the polymer chains increases significantly [16]. Conventionally,

manufacturers test the material using Differential Scanning Calorimetry (DSC) following ASTM E1356 to determine the midpoint temperature of the range bounded by the tangents of the two plateaus within the heat flow curve [17]. If the  $T_g$  is reached or exceeded the resin will begin to soften, leading to plastic deformation of the part which would result in undesirable vehicle performance and potentially failure. A design rule to ensure that matrix softening does not occur is to utilize a material that has a  $T_g$  that is 50°F+ above the maximum expected operating temperature. While it is possible to alter the  $T_g$  of a composite material by manipulating the cure cycle [16], that objective was outside of the scope of the project.

The material available for use in the prototypes were limited to what was available via generous donations to JMS. The main contributors to the program in the form of pre-impregnated materials are Solvay, Park, and Gurit. The various material stiffness, strength, and glass transition temperatures are listed in Table 4.1.1.1. Strength and stiffness values were measured at room temperature dry (RTD) conditioning.

*Table 4.1.1.1: Material Properties of Various Biaxial Weave Prepreg Composites*

<b>Material</b>	<b>E1 RTD (msi)</b>	<b>F1t RTD (ksi)</b>	<b>Tg dry (°F)</b>	<b>Thickness(in)</b>	<b>Source</b>
Cytec 5320-1 / T650-35 3K 8HS	10.04	132.5	374	0.015	Supplier [18]
Cytec 5320-1 / T650 3K PW	9.74	121.8	375	0.0077	NIAR [19]
Park E-765 / 3K PW	8.2	95	330*	0.0089	Supplier [20]
Gurit SE70 / XC411 45 Double Bias	9.57 (+/- 45deg)	205.1 (+/- 45deg)	259	0.0181	Supplier [21]
*At time of material selection the Park E765 composite was specified with a $T_g$ of 300F.					

When considering the data obtained from testing with the JMS17C, it was a clear choice that the Cytec 5320-1 resin system composites were the best option for the prototypes. The sustained operating temperature of 300°F at the brake caliper suggested that the Park E-765



material could soften if the composite structure reached a temperature within the range of  $T_g$ . The same methodology applies to the Gurit SE70 material. When deciding between the two Cytec materials, the eight-harness satin (8HS) fiber was chosen over the plain weave (PW) due to the high degree of drapeability that the satin weave exhibits [22]. Fabrics with a satin weave do not have tows that interlace at every fiber bundle intersection which makes them more suitable for manufacturing parts which contain complex surfaces and tight radii. Additionally, the greater ply thickness reduces the amount of time in ply cutting and lamination to improve manufacturability of the components.

## **4.2. Material Properties**

This section details the Cytec 5320-1 T650-35 3K 8HS and PW material properties and independent material testing for use in the design and analysis of the composite uprights.

### **4.2.1. Material Strength and Stiffness Data**

The material properties of the chosen composite material are listed in the table below. The manufacturers data was shown with material test data from National Institute for Aviation Research (NIAR) and the Department of Defense (DoD). Each prepreg utilizes the same carbon fiber (despite changes in supplier) but variations in resin system and cure cycle should be noted.

Table 4.2.1.1: Material Properties for T650/35 3K Prepreg Composite

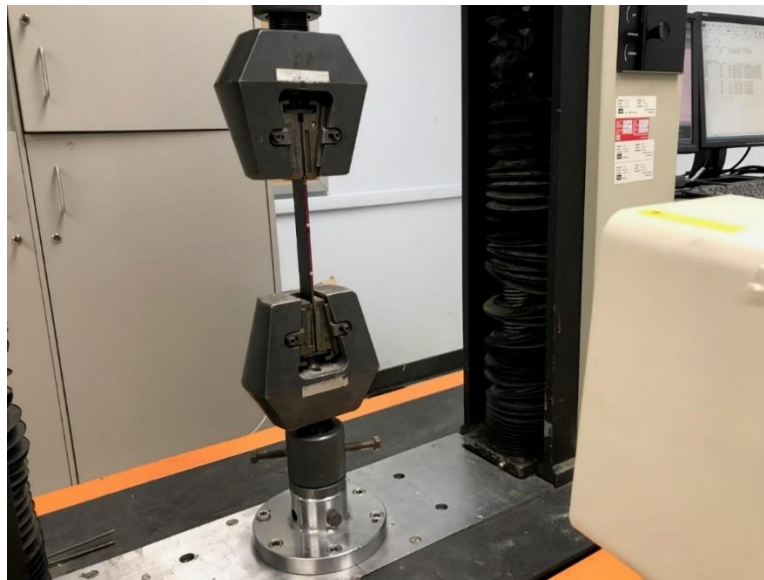
Property	Normalized Mean Value @ RTD (as measured in parenthesis)		
E <sub>1</sub> , Tensile (msi)	10.02	10.04	10.3
E <sub>2</sub> , Tensile (msi)	9.90	9.40	10.7
$\nu_{12}$	0.048	.050	-
G <sub>12</sub> (msi)	(0.81)	(0.63)	(.85)
F <sub>1</sub> <sup>t</sup> (ksi)	131.3	133.49	99.2
F <sub>1</sub> <sup>c</sup> (ksi)	108.8	102.55	86.2
F <sub>2</sub> <sup>t</sup> (ksi)	129.9	125.74	106
F <sub>2</sub> <sup>c</sup> (ksi)	110.6	105.56	90.1
F <sub>12</sub> (ksi)	(8.29)	(18.09)	(12.8)
F <sub>13</sub> (ksi)	(11.93)	(10.39)	-
V <sub>f</sub> (%)	56.7	52-60	58-61
Fiber	Solvay T650/35 3k	Amoco T650/35 3k	Amoco T650/35 3k
Resin	CYCOM 5320-1	Fiberite HMF 7740	Cytec Fiberite 976
Cure Method	VBO	Autoclave	Autoclave
Source	Solvay [18]	NIAR [19]	MIL-HDBK-17-2F [23]

#### 4.2.2. Material Validation

Due to the rapid development schedule of these components, material testing was limited to validation of warp material failure strength and stiffness as well as interlaminar shear strength. Two 12” x 12” panels of each Cytec material were manufactured and cured via an autoclave at 85 pounds per square inch (psi) following the suppliers recommended thermal ramp rates and dwell durations to represent the cure cycle of the uprights. After the test panels were cured, coupons were manufactured to the specifications outlined in ASTM D3039 [24] for tensile samples (Figure 4.2.2.1) and ASTM D2344 [25] for short beam shear samples.



*Figure 4.2.2.1: Tensile Test Coupon with Fiberglass Bonded Tabs*



*Figure 4.2.2.2: Tensile Test Coupon in Uniaxial Load Frame with Extensometer*

Specimen failure strengths were tested using a uniaxial load machine (Figure 4.2.2.2) and their apparent strengths and modulus were normalized to the average laminate thickness for each sample group. Results are shown in Table 4.2.2.1 through Table 4.2.2.4.

Table 4.2.2.1: 8HS Control Coupons – Axis-1 Tensile Strength and Modulus (RTD)

<b>Cytec 5320-1 3K 8HS 0 Degree - Control - ASTM D3039</b>						
Specimen	Thickness	Width	Apparent Strength	Modulus	Normalized Strength	Normalized Modulus
(identification)	(inch)	(inch)	(ksi)	(msi)	(ksi)	(msi)
8HS-C-T1	0.108	1.024	120.533	9.583	120.892	9.612
8HS-C-T2	0.106	1.015	110.914	9.311	109.078	9.157
8HS-C-T3	0.108	1.019	114.383	9.135	114.440	9.139
8HS-C-T4	0.109	1.020	102.209	8.969	103.559	9.088
8HS-C-T5	0.108	1.018	-	9.078	-	9.077
	0.108		112.010	9.215	111.992	9.215

Table 4.2.2.2: PW Control Coupons – Axis-1 Tensile Strength and Modulus (RTD)

<b>Cytec 5320-1 3K PW 0 Degree - Control - ASTM D3039</b>						
Specimen	Thickness	Width	Apparent Strength	Modulus	Normalized Strength	Normalized Modulus
(identification)	(inch)	(inch)	(ksi)	(msi)	(ksi)	(msi)
PW-C-T1	0.112	1.007	105.627	9.103	106.989	9.220
PW-C-T2	0.110	1.003	114.672	9.283	113.549	9.192
PW-C-T3	0.110	0.996	-	9.328	-	9.286
PW-C-T4	0.111	1.014	115.204	9.677	115.149	9.672
PW-C-T5	0.111	1.007	112.614	9.352	112.830	9.370
	0.111		112.029	9.349	112.129	9.348

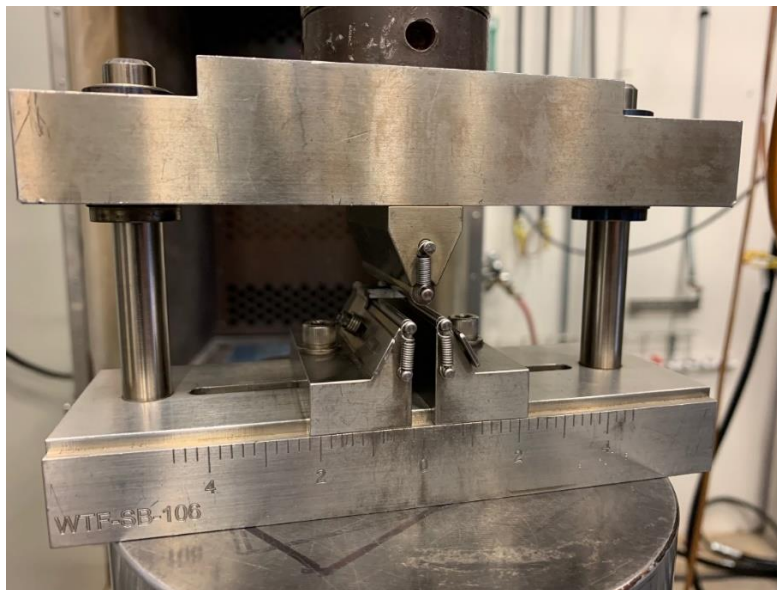


Figure 4.2.2.3: Short Beam Shear Test Fixture

Table 4.2.2.3: 8HS Control Coupons – Interlaminar Shear Strength (RTD)

<b>Cytec 5320-1 3K 8HS 0 Degree - Control - ASTM D2344</b>					
Specimen (identification)	Thickness (inch)	Width (inch)	Span (inch)	Apparent Strength (ksi)	Normalized Strength (ksi)
8HS-C-SB1	0.107	0.210	0.430	8.412	8.417
8HS-C-SB2	0.108	0.220	0.430	8.025	8.040
8HS-C-SB3	0.108	0.213	0.430	8.346	8.379
8HS-C-SB4	0.107	0.217	0.430	8.382	8.365
8HS-C-SB5	0.107	0.214	0.430	8.405	8.369
Average	0.107			8.314	8.314

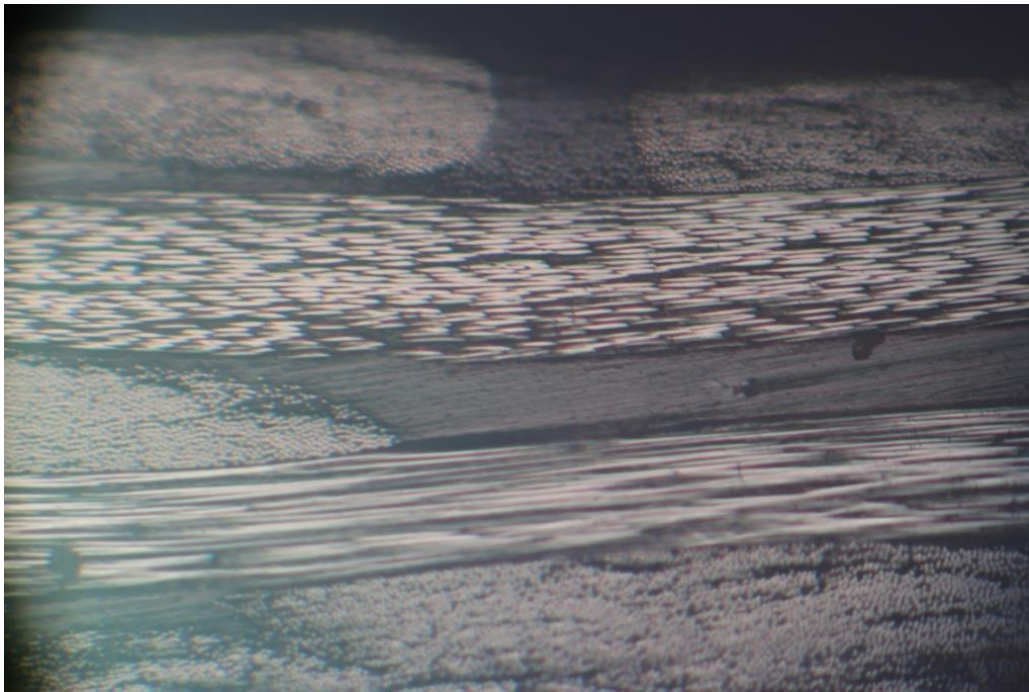
Table 4.2.2.4: PW Control Coupons – Interlaminar Shear Strength (RTD)

<b>Cytec 5320-1 3K PW 0 Degree - Control - ASTM D2344</b>					
Specimen (identification)	Thickness (inch)	Width (inch)	Span (inch)	Apparent Strength (ksi)	Normalized Strength (ksi)
PW-C-SB1	0.112	0.205	0.444	11.759	11.865
PW-C-SB2	0.111	0.206	0.444	11.237	11.237
PW-C-SB3	0.111	0.205	0.444	12.555	12.555
PW-C-SB4	0.111	0.204	0.444	11.430	11.430
PW-C-SB5	0.110	0.201	0.444	11.978	11.870
Average	0.111			11.792	11.791

Warp tensile strength ( $F_{1t}$ ) for the 3K 8HS displayed a normalized average value of 111.992 ksi which is a 14.7% reduction in comparison to the Solvay’s material specification of 131.300 ksi. The warp tensile modulus ( $E_1$ ) tested to a normalized average value 9.215 msi compared to the 10.020 msi per the data sheet for a reduction of 8.0%. Interlaminar shear failure strength ( $F_{13}$ ) for the 8HS material tested to an average of 8.314 ksi in comparison to the as measured Solvay value of 11.930 ksi for a reduction of 30.3%.

Warp tensile strength ( $F_{1t}$ ) for the 3K PW displayed a normalized average value of 112.129 ksi which is a 14.6% reduction in comparison to the Solvay’s material specification of 131.300 ksi. The warp tensile modulus ( $E_1$ ) tested to a normalized average value 9.348 msi compared to the 10.020 msi per the data sheet for a reduction of 6.7%. Interlaminar shear failure strength ( $F_{13}$ ) for the PW material tested to an average of 11.791 ksi in comparison to the as measured Solvay value of 11.930 ksi for a reduction of 1.2%.

The reduction in tested material strength is expected to be from a combination of fiber misalignment and resin aging of the pre-impregnated material. Fiber misalignment can occur during ply cutting and layup of the material. Additionally, when pressure is applied to the panel during the cure cycle fibers can wash out at the edges of the panel resulting in a greater degree of misalignment. A cross section of a zero-degree 8HS laminate coupon is shown in Figure 4.2.2.4. Ply misalignment can be observed in the top layer of carbon fabric with tow bundles running parallel to the page due to the high width to height ratio of the fibers. A sample with a low degree of ply misalignment would demonstrate fibers running parallel or into the image. This image is further compared to data from the research conducted by Sharp, Goodsell, and Favaloro in the discussion section of this chapter.



*Figure 4.2.2.4: Material Microscopy of Composite Tensile Coupon*

### 4.3. Composite Constituent Content via Matrix Ignition

To obtain a better understanding of the loss of strength exhibited by the composite material it was essential to determine the volume fractions of the constituent components. ASTM D3171 [26] provides guidelines for the manufacturing and processing of samples whether the matrix is chemically or thermally digested. The remaining fiber mass in conjunction with the known sample and constituent densities provides for the calculation of fiber, matrix, and void contents.

Sixteen samples of Cytec 5320-1 material were prepared for matrix ignition in an electric kiln. It was important to understand the matrix mass percentage of the uncured prepreg, so half of the samples were taken from consumed tensile test specimen and the other half were produced from uncured composite material. Another factor of consideration was the matrix and fiber content of the 8HS and PW composites. Each coupon had a length and width of one inch and was composed of either seven layers of 8HS or fourteen layers of PW. The uncured samples were compared against the cured samples to ensure consistency between mass fractions of fiber and matrix. The test samples are displayed in Figure 4.3.1 prior to the burn off process.



*Figure 4.3.1: Test Specimen Before Matrix Ignition*

After the samples were prepared, each sample was measured to determine their average length, width, and thickness. The product of the average dimensions determined the volume of the sample. Each specimen was placed on a calibrated scale to measure the mass prior to matrix ignition. The density of each sample was recorded for later use in calculation of the volume content of the fiber, matrix, and voids. The set of samples were placed into an electric kiln (in lieu of a muffle furnace per Procedure G of ASTM D3171) for six hours at 1000°F to completely combust the epoxy (Figure 4.3.2).



*Figure 4.3.2: Test Specimen in Electric Kiln*

After the samples were removed from the kiln, the contents of each crucible were placed on a scale to determine the amount of fiber remaining (Figure 4.3.3). The fiber and matrix content by weight percentage for the cured and uncured samples are displayed in Table 4.3.1 and Table 4.3.2, respectively.



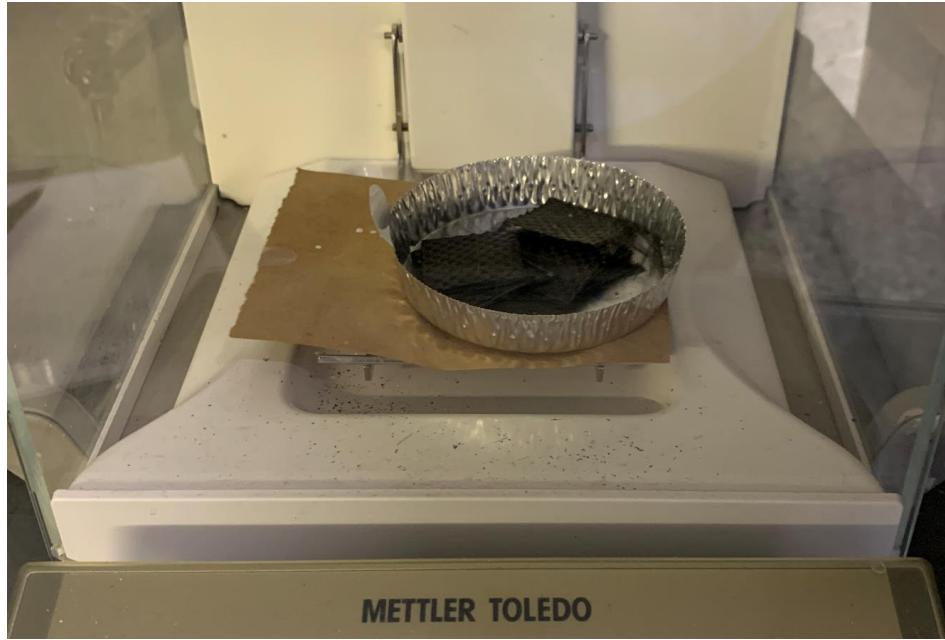


Figure 4.3.3: Test Specimen After Matrix Ignition

Table 4.3.1: Fiber Content by Percentage Weight

<b>W<sub>r</sub> - Fiber Content Weight (%)</b>					
8HS Cured – identification	8HS-C-1	8HS-C-2	8HS-C-3	8HS-C-4	Average
	61.8	62.7	69.2	66.7	65.1
PW Cured – identification	PW-C-1	PW-C-2	PW-C-3	PW-C-4	Average
	61.7	62.2	63.8	65.4	63.3
8HS Uncured – identification	8HS-U-1	8HS-U-2	8HS-U-3	8HS-U-4	Average
	62.7	62.1	60.8	61.2	61.7
PW Uncured – identification	PW-U-1	PW-U-2	PW-U-3	PW-U-4	Average
	60.5	63.1	64.1	64.0	62.9

Table 4.3.2: Matrix Content by Percentage Weight

<b>W<sub>m</sub> – Matrix Content Weight (% , neglecting voids)</b>					
8HS Cured – identification	8HS-C-1	8HS-C-2	8HS-C-3	8HS-C-4	Average
	38.2	37.3	30.8	33.3	34.9
PW Cured – identification	PW-C-1	PW-C-2	PW-C-3	PW-C-4	Average
	38.3	37.8	36.2	34.6	36.7
8HS Uncured – identification	8HS-U-1	8HS-U-2	8HS-U-3	8HS-U-4	Average
	37.3	37.9	39.2	38.8	38.3
PW Uncured – identification	PW-U-1	PW-U-2	PW-U-3	PW-U-4	Average
	39.5	36.9	35.9	36.0	37.1

The reinforcement content volume percent ( $V_r$ ) values displayed in Table 4.3.3 were determined by multiplying the fiber mass content percentage ( $W_r$ ) for each specimen by its respective calculated composite density (in g/cc) to fiber density ratio. The density of the fiber was assumed from the Thornel T-650 fiber datasheet at a value of 1.77 g/cc [27]. The density of the epoxy matrix was assumed to be 1.31 g/cc as provided in the Solvay 5320-1 data sheet [18]. The uncured fiber, matrix, and void volume data for the 8HS and PW samples are not included in Table 4.3.3 through Table 4.3.5 as the data would not be accurate as the material has not been properly consolidated. The equation for the calculation is shown below [8].

$$V_r = \left( \frac{M_f}{M_i} \right) * \left( \frac{\rho_c}{\rho_f} \right) * 100 \quad (18)$$

Table 4.3.3: Fiber Content by Percentage Volume

<b>V<sub>r</sub> – Fiber Content Volume (%)</b>					
8HS Cured - identification	8HS-C-1	8HS-C-2	8HS-C-3	8HS-C-4	Average
	50.5	51.8	58.2	54.8	53.8
PW Cured - identification	PW-C-1	PW-C-2	PW-C-3	PW-C-4	Average
	51.5	51.7	53.8	54.7	52.9

The matrix content volume percent ( $V_m$ ) values displayed in Table 4.3.4 were determined by multiplying the matrix mass content percentage ( $W_m$ ) for each specimen by its respective calculated composite density to matrix density ratio. The equation for the calculation is shown below [8].

$$V_m = \left( \frac{M_f - M_i}{M_i} \right) * \left( \frac{\rho_c}{\rho_m} \right) * 100 \quad (19)$$

Table 4.3.4: Matrix Content by Percentage Volume

<b>V<sub>m</sub> - Matrix Content Volume (%)</b>					
8HS Cured - identification	8HS-C-1	8HS-C-2	8HS-C-3	8HS-C-4	Average
	42.2	41.7	35.0	37.0	39.0
PW Cured - identification	PW-C-1	PW-C-2	PW-C-3	PW-C-4	Average
	43.3	42.4	41.2	39.1	41.5

The void volume percentage ( $V_v$ ) values displayed in Table 4.3.5 were determined via the equation below [8].

$$V_v = 100 - (V_r + V_m) \quad (20)$$

Table 4.3.5: Void Content by Percentage Volume

<b>V<sub>v</sub> - Void Volume (%)</b>					
8HS Cured - identification	8HS-C-1	8HS-C-2	8HS-C-3	8HS-C-4	Average
	7.3	6.5	6.8	8.2	7.2
PW Cured - identification	PW-C-1	PW-C-2	PW-C-3	PW-C-4	Average
	5.2	5.9	5.0	6.3	5.6

According to Mallick, a void content greater than 2.0% is considered high and tends to lead to a lowered fatigue resistance, greater susceptibility to water diffusion, and increased variance in material properties. Therefore, the 7.2% and 5.6% void volumes for the 8HS and PW material, respectively, are considered to have high void content. These high void volumes are suspected to be a result of the inability to properly install an edge dam around the laminate stack per the Cytec 5320-1 processing procedures (Figure 4.3.4).

## VACUUM BAG ARRANGEMENT FOR CURE

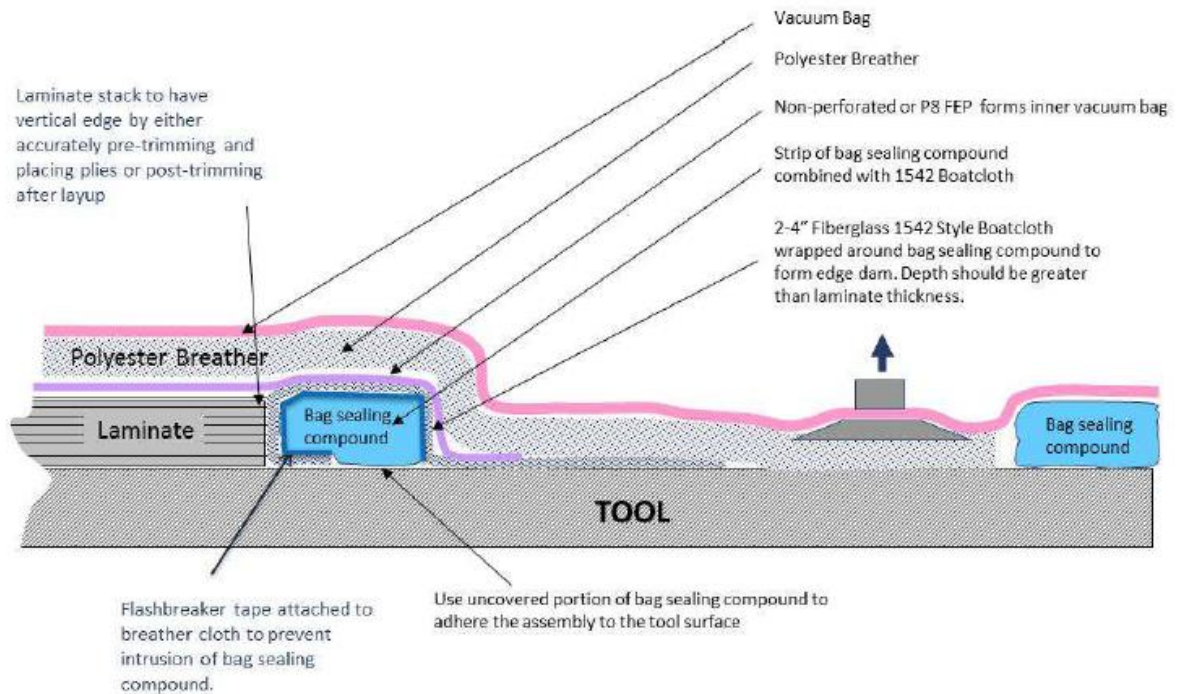


Figure 4.3.4: 5320-1 Vacuum Bag Arrangement for Cure [18]

To verify the measured void volume per procedures in ASTM D3171, the average fiber and matrix weight fractions and constituent densities were substituted into the following equation [8] to determine the theoretical density of the composite.

$$\rho_c = \frac{1}{\left(\frac{w_f}{\rho_f} + \frac{w_m}{\rho_m}\right)} \quad (21)$$

The calculated theoretical density for the composite was 1.58 g/cc. The actual average density of the 8HS material was 1.46 g/cc and the PW material was 1.48 g/cc. Using the following equation [8], the theoretical void volume for each composite was 7.2% and 6.1%.

$$v_v = \frac{\rho_c - \rho}{\rho_c} \quad (22)$$

where  $v_v$  void volume,  $\rho_c$  is theoretical density and  $\rho$  is actual density.

A simple sensitivity study was performed to evaluate the theoretical void volume of the composites. The samples measured for use in the matrix ignition process were cut from broken tensile test specimen and sanded using a disc to be as square as possible. Inherently, this process provides slight askew angles that are measured and averaged for the calculation of the coupon volume. Ideally, each sample would have been placed into a manual mill and squared more accurately and measured with a micrometer. The sensitivity study assumed a  $\pm 0.005''$  in the length and width dimensions and  $\pm 0.001''$  across the thickness. The modified composite densities and void volumes were calculated using these values. If the original coupons were at the upper end of the tolerance the density of the 8HS decreased to 1.44 g/cc and the PW decreased to 1.45 g/cc resulting in a void volume of 8.9% and 7.3% respectively. If the inverse were true and each coupon was 0.005'' smaller in the length and width as well as 0.001'' thinner, the density of the 8HS increased to 1.49 g/cc and the PW increased to 1.51 g/cc resulting in a void volume of 5.4% and 3.8%, respectively. More directly, if the accuracy of the measuring equipment is within  $\pm 0.005''$  across the length and width and within  $\pm 0.001''$  across the thickness the resulting theoretical void volume for the 8HS and PW can range +1.7%/-1.8% from nominal measured values of 7.2% and 5.6% void volume, respectfully.

#### 4.4. Discussion

The tensile strength of control PW and 8HS are within 0.1% of each other suggesting that fiber dominated failure strength of either material are interchangeable. Similarly, the tensile modulus of the 8HS and PW material were 9.215 msi and 9.348 msi, respectively, which are within 1.4% of each other. The interlaminar shear strength of the 8HS (-30.3%) varies significantly from the PW (-1.2%) suggesting that the out of freezer time for the 8HS was much longer. Although the prepreg materials were originally manufactured in 2016, the expired PW composite suggest the manufacturing process for both sets of material samples were consistent. This is further validated via the matrix combustion testing performed on both materials as average fiber content percentages were within 1.0% of each other. Therefore, any variation from material manufacturer strength data is primarily attributed to differences in use and/or storage duration and could possess additional strength loss due to fiber misalignment. Fiber misalignment can occur in material cutting, layup, tensile test sample preparation, and test setup. The image on the left in Figure 4.4.1 demonstrates a comparison of composite panel microscopy manufactured with deliberate ply misalignment orientations of 0° (1), 15° (2), 30° (3), 45° (4), 75° (5) and 60° (6) [28].

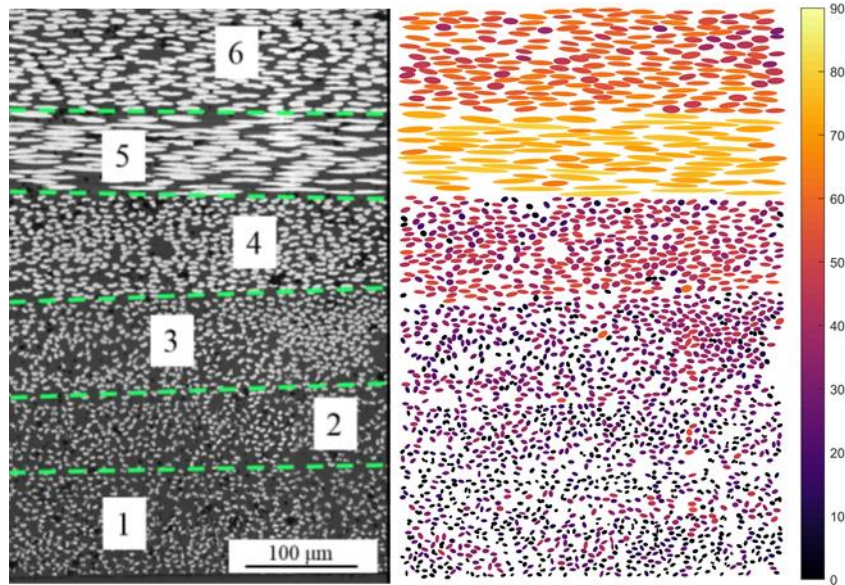


Figure 4.4.1: Microscope Image of Manufactured Laminate with Prescribed Layer Orientations (left) vs Fit Ellipses Colored by Determined Rotation Angle (right) [28]

The image on the right in the same figure shows the authors' fit ellipses to the microscope image to estimate fiber misalignments via the numerical model they developed. Region 5 illustrates a deliberate 15-degree misalignment of the panel. By inspection, the fiber width to length ratio appears to be more extreme than the misalignment that was witnessed in the 5320-1 8HS microscopy from Figure 4.2.2.4.

A simple calculation of a modified modulus due to ply rotation was performed to check the validity of the physical testing results for the tensile specimen (Table 4.4.1). Utilizing the manufactures stiffness data ( $E_1$ ,  $E_2$ ,  $G_{12}$ ) and Poisson's ratios ( $\nu_{12}$ ,  $\nu_{21}$ ), the estimated  $\bar{Q}_{11}$  value reduces to 9.049 msi at 15 degrees of rotation which would suggest a 10.0% reduction in composite stiffness. Therefore, it is believed that any ply misalignment up to 15 degrees occurs locally within the thickness of the sample and does not apply to each ply within the laminate, as investigated within the FEA analysis of the front and rear uprights for global ply misalignment effects on failure index and camber compliance (Section 5.4). The data suggests that some

amount of ply misalignment was a contributor to the overall reduced stiffness of the tensile test samples.

Table 4.4.1: Effects of Ply Rotation on Tensile Modulus

Effect of Rotation on $\bar{Q}_{11}$				
Parameter	Value	Unit	Ply Rotation	Unit
$E_1$	10.020	msi		
$E_2$	9.920	msi		
$G_{12}$	0.810	msi	15	Degrees
$\nu_{12}$	0.048		0.262	Radians
$\nu_{21}$	0.048			
Stiffness Components				
$Q_{11}$	10.043	msi		
$Q_{22}$	9.943	msi		
$Q_{12}$	0.477	msi		
$Q_{66}$	0.810	msi		
Stiffness after Transformation				
$\bar{Q}_{11}$	<b>9.049</b>	msi		

Resin aging of the composite during storage will tend to degrade the strength of the material. Typical shelf life for the CYCOM 5320-1 resin is one year at  $< 10^\circ\text{F}$  and a tack life of 20 days at room temperature [18]. The 8HS material utilized in this project had a manufacture date of 4/28/2016 and the PW material was manufactured on 10/04/2016. It has been noted that cure advancement with increasing storage period has attributed to the decrease in tensile strength by up to 25.0% in prepreg epoxy composites [29].

Chandrakala, Vanaja and Roa also determined that the resin flow of their epoxy matrix samples decreased by around 50.0% after a storage duration of 20 days for both systems that they tested and compared despite having no noticeable influence on the  $T_g$  of the composite material. The lowered resin flow of an epoxy during cure and lower material tackiness would attribute lower interlaminar shear and tensile strength due to poor adhesion of the plies to each other. The lowered tackiness was quantified in their research by a 30.0% increase in sample thickness due to the restricted ability of the prepreg to compact during cure.



While the Solvay material did not exhibit a 30.0% increase in thickness, it is noted that the average ply thickness of the control tensile and interlaminar shear coupons are 0.0154” and 0.0153”, respectively, for samples manufactured from the seven-ply 8HS panels. The manufacturer specifies an average ply thickness of 0.0145” for the material which suggests an average ply thickness increase of 6.2%. The PW tensile and interlaminar shear specimen measured an average thickness of .1109” and .1110” respectively. The manufacturer does not specify an average ply thickness in the data sheet, so the as-manufactured samples were compared against NIAR test data. NIAR recorded an average ply thickness of 0.0079” in their 14-ply material samples. The PW samples are equivalent to an average ply thickness of  $0.0793e-1$ ” per ply, suggesting a ply thickness increase of 0.4%. The lowered material strength is less than desirable in application. Therefore, the analysis performed throughout the laminate design considers the variations from manufacturers specification and utilizes knockdown factors of 0.853 to account for the reduced  $F_{1t}$  material allowable and estimate the  $F_{2t}$ ,  $F_{1c}$ ,  $F_{2c}$  and  $F_{12}$  and 0.920 for  $E_1$ ,  $E_2$ , and  $G_{12}$  to reflect the data obtained from physical material testing.

The Solvay material as tested maintains a similar strength to the Park material as advertised while having a ~25.0% higher  $T_g$  which was essential to meet the operational environmental consideration of the composite uprights. Utilization of a prepreg composite within its shelf life with greater control over fiber alignment would result in a higher performance part with a lower mass in comparison to the material utilized in this project. The 6.2% increase in average ply thickness of the 8HS in comparison to the 0.4% average ply thickness increase of the PW suggest that the epoxy did not flow as well during cure with the 8HS and agrees with the conclusions reached in the study performed by Chandrakala, Vanaja and Roa. This is further substantiated by the requirement of good resin flow and compaction of a laminate to achieve

consolidation of the layers of composite [8]. If a composite does not consolidate appropriately during cure, air bubbles or volatiles can become trapped within the laminate and create voids. Additionally, if the resin is unable to properly flow through the fibers during cure the laminate can develop a nonuniform fiber volume fraction which is evident in the data presented in Table 4.3.3 where the range of fiber volume fraction for 8HS ranges from 50.5% to 58.2%. The measured void volumes for the 8HS and PW material of 7.2% and 5.6% are thought to be higher than normal but are sensitive to the accuracy and precision of the equipment used to determine the specimen dimensions. Variation in length and width dimensions of  $\pm 0.005$ " and thickness of  $\pm 0.001$ " result in a theoretical void volume of +1.7%/-1.8% from nominal.

The absence of an edge dam during cure can inhibit the ability of the laminate to remove air or volatiles during cure opposed to the conventional through-thickness evacuation. However, the consistency of the interlaminar shear strength test data for the PW material in comparison to the manufacturers data suggests that the void content is below 2.0% - 3.0% by volume that can reduce tensile, compressive, and flexural strengths [8]. Since the PW and 8HS samples were produced utilizing identical processes and equipment, it is concluded that the reduction in flexural strength of the 8HS is a function of resin storage duration.

## 5. Analysis

This section delivers an overview of the analysis performed to determine the laminate configuration for the front and rear uprights. Finite element analysis software was utilized to approximate the structural integrity of the composite uprights and aluminum mounts. Altair is a leading computer-aided engineering (CAE) software solution provider that sponsors FSAE organizations at no cost to the university. Hypermesh 2017 was utilized as the preprocessor with the OptiStruct solver. Hyperview 2017 was used for postprocessing of the analysis output.

### 5.1. Model Setup

To perform the FEA, a minimum of part geometry, material properties, boundary conditions, and load cases are required. The tooled surface of the upright was extracted from the part model and imported into Hyperworks. Material properties from Solvay's material data sheet are input to the FEA material model and applied to the composite geometry. Tensile and compressive material failure strengths are scaled by a knockdown factor (0.853) determined via material testing to account for the resin aging of the composite. Tensile, compressive, and in-plane shear modulus were scaled by a knockdown factor (0.920) determined via material testing. The short beam shear strength from testing was used for interlaminar strength values. The material allowable values are displayed in Table 5.1.1.

*Table 5.1.1: Material Allowable Values for Finite Element Model*

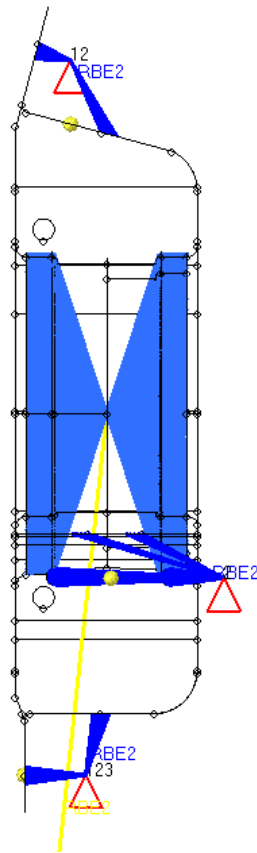
<b>Material Component</b>	<b>Strength (ksi)</b>
F <sub>1t</sub>	111.999
F <sub>1c</sub>	92.806
F <sub>2t</sub>	110.805
F <sub>2c</sub>	94.342
F <sub>12</sub>	7.071
F <sub>13</sub>	8.314
F <sub>23</sub>	8.314

Load cases were determined using tire data from the Tire Testing Consortium (TTC) and vehicle kinematic models to produce limit force vectors for application to the center of the tire contact patch in the FEA model. Boundary conditions are applied to the model to replicate the constraints necessary to fully define an upright as described in the suspension geometry section of Chapter 2. The boundary conditions applied to the upright are shown in Figure 5.1.1.

The upper ball joint, lower ball joint, and steering/toe constraints are modeled using rigid body elements (RBE). These RBE connect the respective fastener locations of the aluminum mounts to a node in space that represent the location of the outboard spherical ball joints (Figure 5.1.1 red triangles). The constraints for the model are applied to the independent node in space that are linked to the composite surface (Figure 5.1.1 in dark blue). The upper ball joint is constrained in  $U_x$  and  $U_y$  to not allow translation. All rotations ( $R_x$ ,  $R_y$ , and  $R_z$ ) and translation  $U_z$  are permitted at the upper ball joint constraint. The lower ball joint is fixed to not allow translation in X, Y, or Z, but allows all rotational degrees of freedom. The steering/toe connection is constrained to allow all rotation and translation in  $U_x$  and  $U_z$ .

Loads are applied remotely to the composite structure in a similar fashion. A node is placed at the geometric center in the loaded radius of the tire contact patch and is connected to a node via a RBE that is equidistant to the wheel bearings (Figure 5.1.1 yellow line). This rigid body element represents the wheel which would transfer load from the contact patch to hub. The node between the wheel bearings is connected to the radial and inboard component nodes of the composite surface via RBE3 to represent the hub that would typically reside within the upright (Figure 5.1.1 in light blue). The RBEs representing the hub only allow rotational displacements of  $R_x$  and  $R_z$  to be transferred to the upright. The same general

model simplifications and boundary conditions are used for analysis of the rear upright. Separate analysis of the mounts and simplification of the corner suspension geometry allows for a more efficient analysis that requires fewer resources to run iteratively and provides a more conservative result by isolating the analysis to that of the composite upright.



*Figure 5.1.1: Side View of Front Upright Boundary Conditions and Loads*

The imported surface geometry is meshed within the Hypermesh preprocessor using a PCOMPP composite element. The PCOMPP element is simply a two-dimensional shell element that allows for the analysis of the composite laminate to be reduced to a solid mechanics problem using classical laminate theory [30]. The mesh generated for the front and rear upright utilize a combination of triangular and quadrilateral elements with a characteristic length of 0.05". All

load cases are applied to the node representing the tire contact patch and are detailed further in the following section.

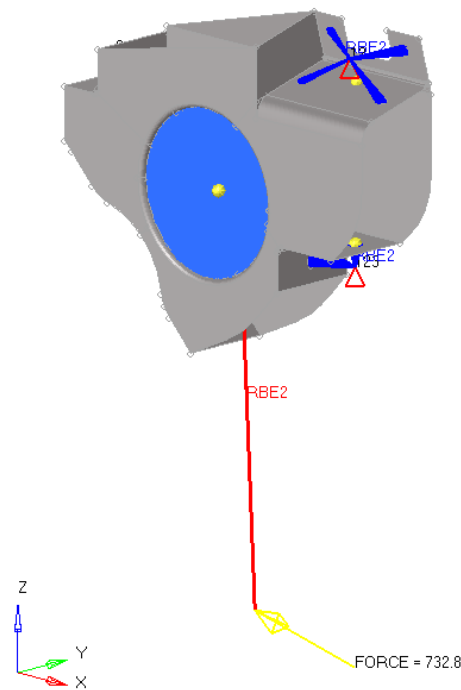


Figure 5.1.2:Rear Upright Boundary Conditions and Loads

### 5.1.1. Load Cases

The load cases implemented in this project were determined using tire data from the TTC, suspension geometry and kinematic calculations to solve for the limit tire loads expected in different vehicle performance scenarios. These forces are given in the tire coordinate system and applied to the node located in the tire contact patch. The front tire load cases are maximum lateral acceleration, maximum braking, maximum longitudinal acceleration and braking during turn entry. The values are organized in Table 5.1.1.1.

Table 5.1.1.1: JMS19C Front Tire Load Cases

<b>Front Tire Force</b>			
Load Case	X -Longitudinal (lbf)	Y - Lateral (lbf)	Z - Vertical (lbf)
Maximum Lateral Acceleration	0	-514	313
Maximum Braking	-344	0	300
Maximum Longitudinal Acceleration	100	0	78
Braking During Turn Entry	-307	-409	325

The rear tire load cases are similar to the front tire load cases. However, the JMS19C utilizes a rear-wheel-drive powertrain, therefore the addition of an accelerating through corner load case is necessary to be analyzed. The values of these load cases applied to the rear tire contact patch are organized in Table 5.1.1.2.

Table 5.1.1.2: JMS19C Rear Tire Load Cases

<b>Rear Tire Force</b>			
Load Case	X -Longitudinal (lbf)	Y - Lateral (lbf)	Z - Vertical (lbf)
Maximum Lateral Acceleration	0	-626	381
Maximum Braking	-206	0	180
Maximum Longitudinal Acceleration	297	0	232
Accelerating Through Turn	276	-348	378
Braking During Turn Entry	-256	-341	271

In normal testing and competition scenarios the race vehicle drives on a smooth flat surface. Therefore, the load cases do not account for any impact or shock scenarios. These cases would be experienced if a passenger vehicle would strike a pothole or curb. To achieve a greater degree of safety, these components should be analyzed for those load cases to ensure failure does not occur in the event of an incidental impact. However, since this vehicle is a designed for off-highway purposes only, impact is not expected to occur.

## 5.2. Laminate Development

To determine the most efficient and best performing laminate the front and rear composite structures were evaluated beginning with a base global laminate and incrementally adjusted. The

main parameters of focus were in-plane composite failure index, dynamic camber change, and weight. The data presented in Table 5.2.1 through Table 5.4.2 utilize the in-plane and interlaminar composite failure criteria available within the Altair Hyperworks software.

*Table 5.2.1: Front Upright Laminate Development*

Front Upright Analysis - Maximum Lateral Acceleration								
Rev	Laminate					Design Parameter		
	Global (G)	Local				Weight	Failure Index	Camber Compliance
		Bearing	UCA/LCA Mount	Shear Web	Brake Flange	lb	(Hashin)	$\Delta\theta/g$
1	[0,45]os	G	G	G	G	0.286	3.987	0.105
2	[45,0]s	G	G	G	G	0.374	1.246	0.062
3	[0,45]s	G	G	G	G	0.374	0.964	0.053
4	[0,45]os	G,45,0	G,45,0	G	G,45,0	0.398	0.759	0.029
5	[0,45]s	G,45,0	G,45,0	G	G,45,0	0.485	0.666	0.018
<b>6</b>	<b>[0,45]s</b>	<b>G,0,45,0</b>	<b>G,0,45,0</b>	<b>G</b>	<b>G</b>	<b>0.514</b>	<b>0.606</b>	<b>0.015</b>
7	[0,45]s	G,0,45,0	G,0,45,0	G	G,45,0	0.523	0.604	0.015
8	[0,45]s	G,0,45,0	G,0,45,0	45,0,G,0,45	G,45,0	0.549	0.594	0.015

The global laminate in Table 5.2.1 and Table 5.2.2 is represented as G within the local columns. A global laminate iteration [0,45]os would suggest a layup of plies in 0, 45, 0 degree configuration (as shown in iteration one of Table 5.2.1) with the first zero degree ply starting at the tooled surface of the part. The local ply layup for the brake flange in iteration eight of the front upright of G,45,0 suggests a layup of 0,45,45,0,45,0 with the first zero-degree ply beginning at the tooled surface of the part. The global laminates as analyzed were applied to the entire component while local laminates were added to specific regions of the structure based on the location of higher strain gradients. The final iteration for front and rear upright laminates are emboldened in their respective tables.



Table 5.2.2: Rear Upright Laminate Development

Rear Upright Analysis - Maximum Lateral Acceleration						
Rev	Laminate			Design Parameter		
	Global (G)	Local		Weight	Failure Index	Camber Compliance
		UCA/LCA Mount	Shear Web	lb	(Hashin)	$\Delta\theta/g$
1	[0,45]s	G	G	0.415	6.875	0.899
2	[45,0]s	G	G	0.415	4.434	0.893
3	[45,0,45,0]os	G	G	0.710	3.036	0.422
4	[45,0,45,0]os	G,0,45,45,0	G	0.793	2.549	0.313
5	[45,0,45,0]os	G,0,45,45,0	45,0,0,G,0,0,45	0.832	2.289	0.313
6	[45,0,45,0]s	G	G	0.808	3.168	0.339
7	[45,0,45,0]s	G,0,45,45,0	G	0.889	2.665	0.225
8	[45,0,45,0]s	G,0,45,45,0,45,45,0	G	0.986	2.233	0.191
9	[45,0,45,0]s	G,0,45,45,0,45,45,0,45,45,0	G	1.052	1.864	0.167
10	[45,0,45,0]s	G,0,45,45,0,45,45,0,45,45,0	45,0,0,G,0,0,45	1.091	1.666	0.166
<b>11</b>	<b>[45,0,45,0]s</b>	<b>G,0,45,45,0,45,45,0,45,45,0,45,45,0</b>	<b>G</b>	<b>1.123</b>	<b>0.632</b>	<b>0.153</b>
12	[45,0,45,0]s	G,0,45,45,0,45,45,0,45,45,0,45,45,0	45,0,0,G,0,0,45	1.161	0.571	0.144

The factor of safety for the structure was chosen based upon the recommended minimum design factor for composite structures outlined in the FAA’s Guide to Verifying Safety-Critical Structures for Reusable Launch and Reentry Vehicles [31]. The source recommends a minimum factor of safety (FS) of 1.500 of the material ultimate strength for a uniform geometry material in a protoflight verification approach. A FS of 1.500 for these components was the design minimum which correlates to a failure index (FI) value of 0.667 ( $FI = 1/SF$ ) for Maximum Strain and Hashin failure methods [32] and 0.444 ( $FI = 1/SF^2$ ) for Tsai-Wu [33]. The front and rear upright laminate analysis result in a Hashin safety factor of 1.650 and 1.582, respectively, which are both above the recommended minimum of 1.500.

Camber compliance in cornering was another significant parameter to reduce in the design of the composite uprights. The maximum lateral load case was chosen for the laminate development because it utilizes the greatest magnitude force vector at the contact patch for front upright. The through corner acceleration load case for the rear upright results in a slightly higher magnitude of

force at the tire contact patch but would not allow for a pure evaluation of expected camber compliance due to the longitudinal force component within the load case. The significance of minimizing the camber compliance contribution of the upright is relevant because the contact patch of the tire will change and can result in loss of grip under high load and undesirable vehicle handling characteristics.

As the laminate is iterated to utilize more material the weight increases while the failure index and dynamic camber change decrease. The balance of these parameters while consideration of ease of manufacturing were investigated through the iterations listed in the composite development. Figure 5.2.1 and Figure 5.2.2 provide visual representations of the laminate iterations as the weight, FI, and camber change converge on their estimated values. Revision numbers after the chosen laminate would provide marginal safety factor increase and camber stiffness at the expense of additional time and material in manufacturing that would add unnecessary weight.

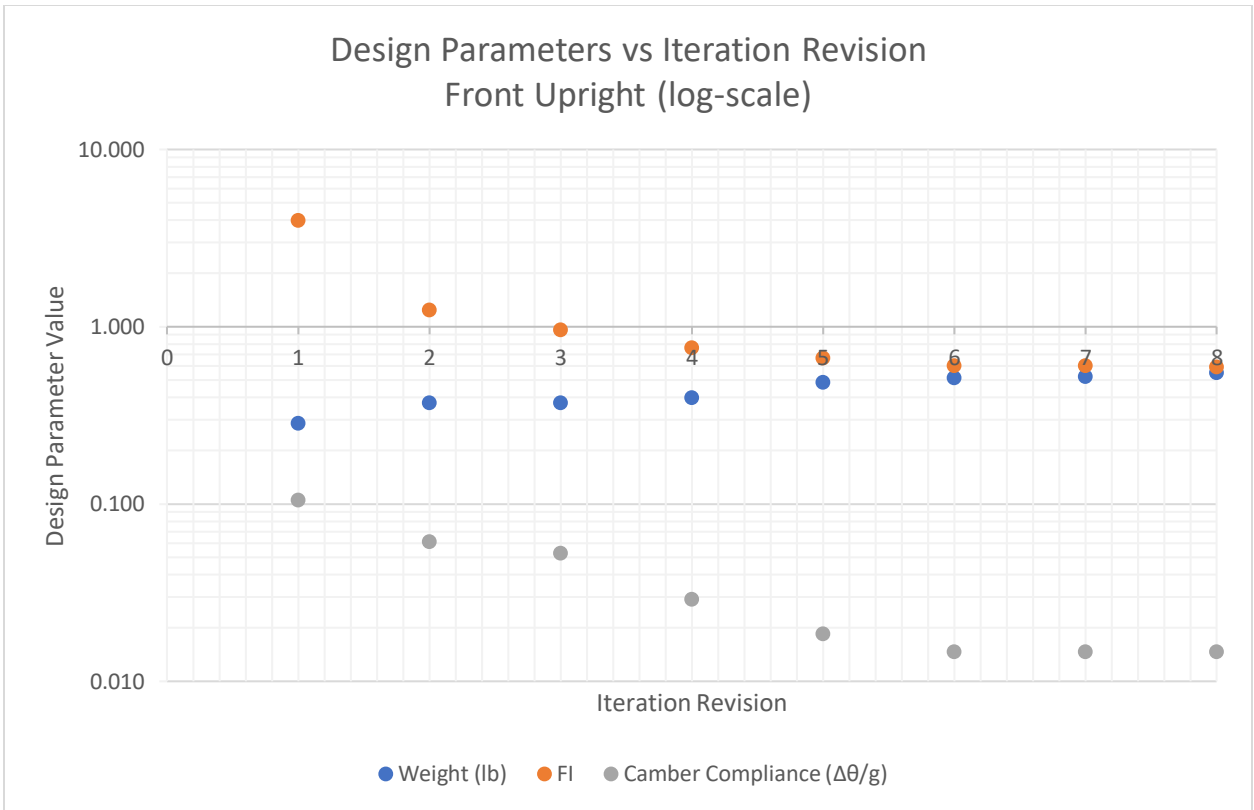


Figure 5.2.1: Design Parameter Values vs Iteration Revision for Front Upright Laminate

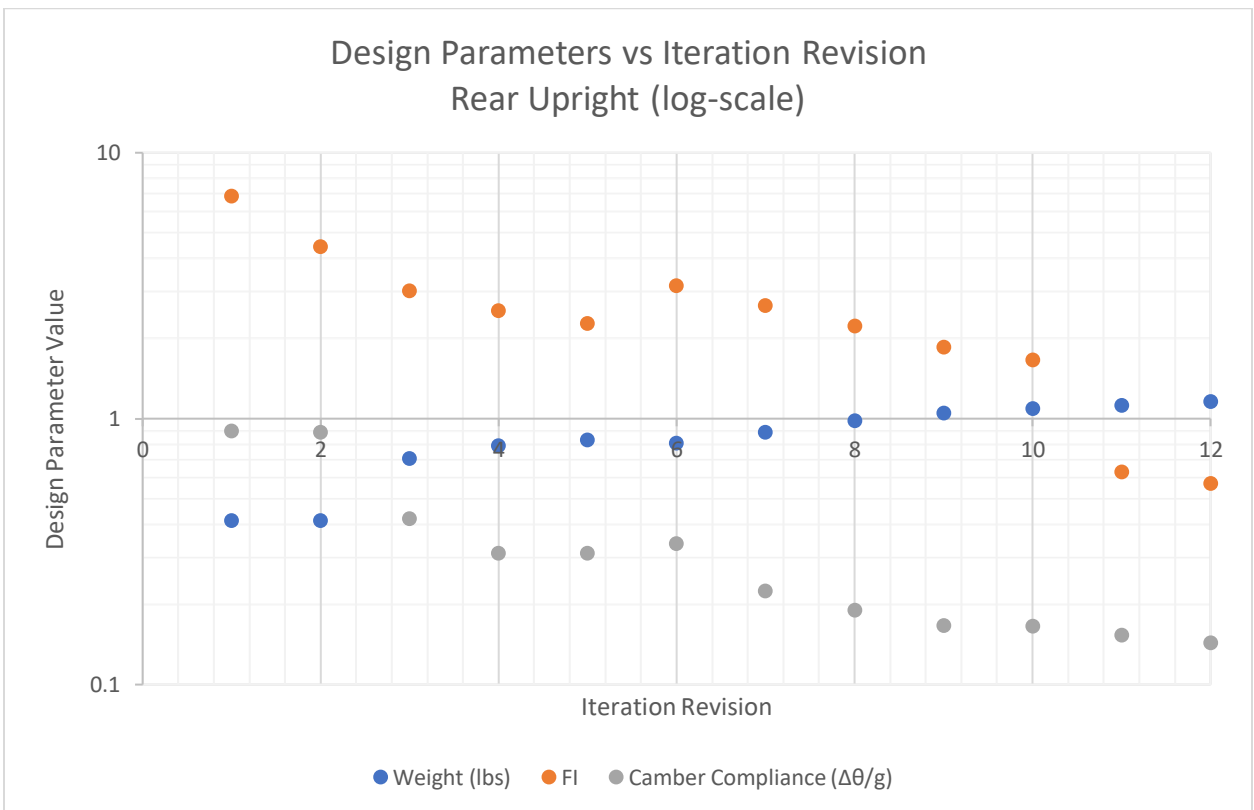


Figure 5.2.2: Design Parameter Values vs Iteration Revision for Rear Upright Laminate

After the laminate for each upright was determined, the analysis was expanded to consider the failure indices due to additional load conditions from Table 5.1.1.1 and Table 5.1.1.2. The element from each structure with the highest bond failure index was determined and the ply and bond failure values were organized in Table 5.2.3 and Table 5.2.4.

*Table 5.2.3: Load Case Failure Index Comparison (Hashin) – Front Upright*

<b>Hashin Failure Index - All Load Cases - Front Upright</b>		
Load Case	FI (bond)	FI (ply)
Maximum Lateral Acceleration	0.606	0.110
Maximum Braking	0.317	0.010
Maximum Longitudinal Acceleration	0.168	0.004
Braking During Turn Entry	0.519	0.039

*Table 5.2.4: Load Case Failure Index Comparison (Hashin) – Rear Upright*

<b>Hashin Failure Index - All Load Cases - Rear Upright</b>		
Load Case	FI (bond)	FI (ply)
Maximum Lateral Acceleration	0.632	0.060
Maximum Braking	0.081	2.988E-05
Maximum Longitudinal Acceleration	0.363	9.681E-05
Braking During Turn Entry	0.611	0.016
Accelerating Through Turn	0.571	0.021

In the load case analysis for the front and rear uprights the maximum lateral acceleration load case demonstrated the highest failure index. The magnitude of the bond failure index is higher in both cases due to the greater interlaminar stresses present within the geometry at the critical elements. The calculation of the bond and ply failure indices is covered in more depth later in the chapter.

### **5.3. Composite Failure Analysis**

There are several different methods to predict composite material failure. The two main categories of failure are comparison of independent stress components and the interaction of stress components. Maximum strain and stress theories are considered independent material

component comparisons while Tsai-Wu and Hashin are characterized as stress interaction theories. The analysis performed on the composite upright models considered failure indices from both classes of failure theories.

### 5.3.1. Maximum Strain Theory

The maximum strain theory and maximum stress theory are both considered independent component failure comparisons. In this sense, the resulting principal strain (or stress) from an applied load is compared against its respective material strain limit at failure. The strain limits for an orthotropic material differ in tension and compression for either principal material direction. As a result, each applied strain for a principal material direction can be compared against its limit to determine if the lamina will fail. These ratios are given below [32].

$$FI_i = \begin{cases} \frac{\varepsilon_i}{\varepsilon_{iT}} \text{ for } \varepsilon_i > 0 \\ -\frac{\varepsilon_i}{\varepsilon_{iC}} \text{ for } \varepsilon_i < 0 \end{cases} \text{ and } i = 1, 2, 3 \text{ (normal strain components)} \quad (23)$$

$$FI_{ij} = \left| \frac{\gamma_{ij}}{\gamma_{sij}} \right| \text{ for } \varepsilon_{ij} > 0 \text{ and } i, j = 1, 2, 3 \text{ (shear strain components)} \quad (24)$$

$$FI = \max(FI_1, FI_2, FI_3, FI_{23}, FI_{13}, FI_{12}) \quad (25)$$

The failure indices for the normal strain components are determined based on the sign of the applied strain. For example, an applied compressive strain in the number one principal material direction would be calculated using the compressive strain allowable. The failure index for an interlaminar strain is determined via the absolute value of the ratio of the applied strain and the strain allowable. Since the interlaminar failure is a matrix dominated method, the strain allowable for this project is assumed as  $\gamma_{s13} = \gamma_{s23}$  using the experimental data determined in Chapter 4. To avoid lamina failure, it is ideal to have a failure index below one for any given strain component.

### 5.3.2. Tsai-Wu Failure Theory

Stress interaction theories improve upon the maximum strain theory by simultaneously considering more than one stress component in determining a failure index value. Specifically, Tsai-Wu provides a better curve fit of biaxial failure to experimental data by increasing number of terms in the prediction equation [6]. Figure 5.3.2.1 demonstrates the improvement in curve fitting of the Tsai-Wu failure calculation in comparison to the maximum strain theory.

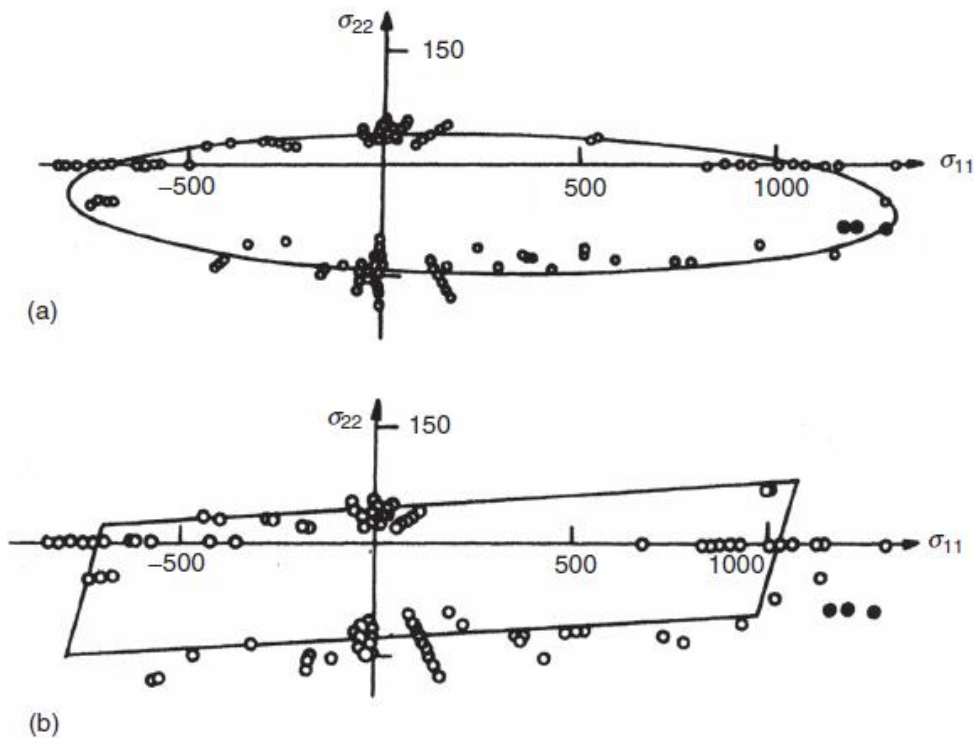


Figure 5.3.2.1: Comparison of (a) Tsai-Wu and (b) Maximum Strain Failure Theories with Biaxial Strength Data of CFRP [8]

The three-dimensional formulation of Tsai-Wu failure criteria is displayed below where  $F_{12}$  and  $F_{23}$  are strength interaction terms between their respective applied stress directions that are experimentally determined. Additionally, Tsai-Wu produces a more accurate failure

prediction in comparison to earlier interaction theories (Hill for example) by considering the different principal material strengths in tension versus compression. The three-dimensional Tsai-Wu failure index is calculated as follows [33].

$$\begin{aligned}
 FI = & F_1\sigma_1 + F_2(\sigma_2 + \sigma_3) + F_{11}\sigma_1^2 + F_{22}(\sigma_2^2 + \sigma_3^2) + F_{44}\tau_{23}^2 + \\
 & F_{66}(\tau_{13}^2 + \tau_{12}^2) + 2F_{12}\sigma_1(\sigma_2 + \sigma_3) + 2F_{23}\sigma_2\sigma_3
 \end{aligned} \tag{26}$$

$\sigma_3$  is typically prevalent in a structure like a pressure vessel where the applied load is distributed normal to the laminate. Due to the geometry of the front and rear upright, the  $\sigma_3$  term in the equation is assumed to be zero, thus it can be neglected. Therefore, the Tsai-Wu formulation is reduced to

$$\begin{aligned}
 FI = & F_1\sigma_1 + F_2\sigma_2 + F_{11}\sigma_1^2 + F_{22}\sigma_2^2 + \\
 & F_{44}\tau_{23}^2 + F_{66}(\tau_{13}^2 + \tau_{12}^2) + 2F_{12}\sigma_1\sigma_2
 \end{aligned} \tag{27}$$

Where the coefficients are defined as:

$$\begin{aligned}
 F_1 &= \frac{1}{X_t} + \frac{1}{X_c} & F_2 &= \frac{1}{Y_t} + \frac{1}{Y_c} \\
 F_{11} &= \frac{1}{X_t * X_c} & F_{22} &= \frac{1}{Y_t * Y_c} \\
 F_{44} &= \frac{1}{S_{23}^2} & F_{55} &= \frac{1}{S_{13}^2} & F_{66} &= \frac{1}{S_{12}^2}
 \end{aligned}$$

Reduced failure equation for orthotropic lamina under plane stress conditions will reduce this equation even further. Classical lamination theory and the in-plane ply failure index calculation in Hyperworks utilize the following equation [34]:

$$FI = F_1\sigma_1 + F_2\sigma_2 + F_{11}\sigma_1^2 + F_{22}\sigma_2^2 + F_{66}\tau_{12}^2 + 2F_{12}\sigma_1\sigma_2 \tag{28}$$

As previously mentioned,  $F_{12}$  is the strength interaction term between  $\sigma_1$  and  $\sigma_2$  and is typically determined via equi-biaxial material test. Interaction terms can be difficult and

expensive to obtain and appears to have little influence on the results. Narayanaswami and Adelman suggest  $F_{12}$  may be substituted as zero while S.W. Tsai and H.T. Hahn suggest  $F_{12}$  may be approximated from the following range.

$$-\frac{1}{2}(F_{11}F_{22})^{\frac{1}{2}} \leq F_{12} \leq 0 \quad (29)$$

The lower limit of equation above is frequently used as an approximation of the  $F_{12}$  term [8]. For the analysis performed in this project a lower bound value of  $F_{12} = -4.797 \text{ E-11}$  was calculated and used instead of an experimental biaxial material parameter.

### 5.3.3. Hashin Failure Theory

Hashin's theory for composite materials is another failure index calculation based on the interaction of stresses and differentiates between fiber and matrix failure. The equations below are for a three-dimensional stress state [35]

1. Tensile fiber failure for  $\sigma_1 \geq 0$

$$FI = \frac{\sigma_1^2}{S_{1T}^2} + \frac{\tau_{13}^2 + \tau_{12}^2}{S_{s12}^2} \quad (30)$$

2. Compressive fiber failure for  $\sigma_1 < 0$

$$FI = \frac{\sigma_1^2}{S_{1C}^2} \quad (31)$$

3. Tensile matrix failure for  $\sigma_2 + \sigma_3 > 0$

$$FI = \frac{(\sigma_2 + \sigma_3)^2}{S_{2T}^2} + \frac{\tau_{23}^2 - \sigma_2 \sigma_3}{S_{s23}^2} + \frac{\tau_{13}^2 + \tau_{12}^2}{S_{s12}^2} \quad (32)$$

4. Compressive matrix failure for  $\sigma_2 + \sigma_3 < 0$

$$FI = \left( \frac{S_{2C}^2}{4S_{s23}^2} - 1 \right) \left( \frac{\sigma_2 + \sigma_3}{S_{2C}} \right) + \frac{(\sigma_2 + \sigma_3)^2}{4S_{s23}^2} + \frac{\tau_{23}^2 - \sigma_2 \sigma_3}{S_{s23}^2} + \frac{\tau_{13}^2 + \tau_{12}^2}{S_{s12}^2} \quad (33)$$

5. Interlaminar tensile failure for  $\sigma_3 > 0$

$$FI = \frac{\sigma_3^2}{S_{3T}^2} \quad (34)$$



6. Interlaminar compression failure for  $\sigma_3 < 0$

$$FI = \frac{\sigma_3^2}{S_{3C}^2} \quad (35)$$

The indices obtained using Hyperworks primarily consider the in-plane stresses for the prediction of failure [34]. As a result, the previous equations reduce to the following:

1. Tensile fiber failure for  $\sigma_1 \geq 0$

$$FI = \frac{\sigma_1^2}{S_{1T}^2} + \frac{\tau_{12}^2}{S_{s12}^2} \quad (36)$$

2. Compressive fiber failure for  $\sigma_1 < 0$

$$FI = \frac{\sigma_1^2}{S_{1C}^2} \quad (37)$$

3. Tensile matrix failure for  $\sigma_2 > 0$

$$FI = \frac{(\sigma_2)^2}{S_{2T}^2} + \frac{\tau_{12}^2}{S_{s12}^2} \quad (38)$$

4. Compressive matrix failure for  $\sigma_2 < 0$

$$FI = \left( \frac{S_{2C}^2}{4S_{s23}^2} - 1 \right) \left( \frac{\sigma_2}{S_{2C}} \right) + \frac{(\sigma_2)^2}{4S_{s23}^2} + \frac{\tau_{12}^2}{S_{s12}^2} \quad (39)$$

where  $S_{s23}$  is defined by the approximation  $S_{s12} = S_{s23}$  for compressive matrix failure.

### 5.3.4. Failure Theory Comparison

The data provided within the following tables are based upon the failure index calculation utilized by the Hyperworks software. As such, the ply indices are determined for the entire laminate via the in-plane failure calculations from the previous subsections for the respective failure theory. The value of bond failure is determined via the equation per the Hyperworks documentation [34].

$$FI = \frac{\max(|\tau_{13}|, |\tau_{23}|)}{S_B} \quad (40)$$

Table 5.3.4.1: Failure Theory Comparison – Front Upright

<b>Failure Theory Comparison - Maximum Lateral Load – Front Upright</b>		
Failure Theory	FI (bond)	FI (ply)
Tsai-Wu	0.606	0.144
Maximum Strain	0.606	0.319
Hashin	0.606	0.110

Table 5.3.4.2: Failure Theory Comparison – Rear Upright

<b>Failure Theory Comparison - Maximum Lateral Load – Rear Upright</b>		
Failure Theory	FI (bond)	FI (ply)
Tsai-Wu	0.632	0.109
Max Strain	0.632	0.238
Hashin	0.632	0.060

Failure in front and rear upright is expected from interlaminar stress due to bending and since FI is determined using the same formula regardless of failure theory. Additionally, the critical ply failure for a given theory from bond failure may not correspond to ply failure due to in plane tension or compression. The data in the previous two tables simply considers all maximum failure indices for the entire laminate at a specific element. The following study in critical ply failure considers the three-dimensional stress state for calculation of Hashin and Tsai-Wu failure indices in Section 5.5.

#### **5.4. Fiber Misalignment Study**

This study was performed using the existing FEA models for the front and rear uprights to determine the impact on the factor of safety on each component due to fiber misalignment. As mentioned in Chapter 4, fiber misalignment in a laminate can be attributed to deviation of orientation in ply cutting and in layup which can result in changes of strength and stiffness for the manufactured component. To quantify the potential change in dynamic camber change and failure index of the parts, each ply in the laminate within the FEA material model was increased either five or ten degrees for comparison with the baseline analysis for the

maximum lateral acceleration load case. Results from the analysis are displayed for comparison in Table 5.4.1 and Table 5.4.2.

*Table 5.4.1: Fiber Misalignment Study – Front Upright*

<b>Misalignment Study - Maximum Lateral Acceleration - Front Upright</b>		
Degree of Misalignment	Failure Index	Camber Compliance ( $\Delta\theta/g$ )
0°	0.606	0.015
5°	0.605	0.015
10°	0.612	0.015

*Table 5.4.2: Fiber Misalignment Study – Rear Upright*

<b>Misalignment Study - Maximum Lateral Acceleration - Rear Upright</b>		
Degree of Misalignment	Failure Index	Camber Compliance ( $\Delta\theta/g$ )
0°	0.632	0.153
5°	0.655	0.135
10°	0.650	0.137

The data presented in Table 5.4.1 suggest that the front upright is much less sensitive to ply angle misalignment with respect to the predicted dynamic camber change, as each analysis provided the same result of 0.015 degree/g. However, the five-degree misalignment model resulted in a slightly lower failure index than baseline and the ten-degree model. The data presented in Table 5.4.2 shows different trends than the front upright, most notable being that a five-degree rotation in all ply alignment would produce a lower camber compliance with the sacrifice of part failure index increasing slightly. All misalignment studies for the front and rear uprights predicted a Hashin failure index less than the 0.667 required to be compliant with the FAA recommendations for composite structures.

## **5.5. Critical Ply Analysis**

To provide greater insight into the failure of the front and rear uprights, a deeper analysis was performed to expand the failure criteria to the three-dimensional stress state. As demonstrated in Table 5.3.4.1 and Table 5.3.4.2, Hyperworks uses a simplified prediction for bond/interlaminar

shear failure which makes Maximum Strain, Tsai-Wu and Hashin appear to have the same failure results, when in actuality the underlying calculations are not the same. They follow the same interlaminar shear stress comparison supporting the data in Table 5.2.1 through Table 5.4.2

To solve for complete three-dimensional failure indices for Tsai-Wu, Hashin, and Maximum Strain, stress components were extracted from the ply with the maximum failure index of the most critical element. These values are compared against material allowables that were derived from experimental data. The tensorial stress values are organized for the front and rear uprights in Table 5.5.1 and Table 5.5.2, respectively. Failure index is calculated for each material component via the equation

$$FI = \frac{\sigma_{allowable}}{\sigma_{applied}} \quad (41)$$

Table 5.5.1: Critical Ply Analysis – Front Upright

<b>Critical Ply Analysis - Global 0 Degree #2 - Front Upright</b>			
Material Component	Stress Allowable (ksi)	Applied Stress (ksi)	FI (Equation 41)
F1t	111.999	-	-
F1c	92.806	1.160	0.012
F2t	110.805	4.041	0.036
F2c	94.342	-	-
F12	7.071	0.571	0.081
<b>F13</b>	<b>8.314</b>	<b>5.037</b>	<b>0.606</b>
F23	8.314	4.020	0.484

Table 5.5.2: Critical Ply Analysis – Rear Upright

<b>Critical Ply Analysis - Global 45 Degree #2 - Rear Upright</b>			
Material Component	Stress Allowable (ksi)	Applied Stress (ksi)	FI (Equation 41)
F1t	111.999	-	-
F1c	92.806	1.137	0.012
F2t	110.805	-	-
F2c	94.342	0.893	0.009
F12	7.071	0.344	0.049
<b>F13</b>	<b>8.314</b>	<b>5.252</b>	<b>0.632</b>
F23	8.314	2.585	0.311

The front upright model predicts the highest failure index in the  $F_{13}$  material component with a failure index of 0.606. The rear upright model predicts the highest failure index in the  $F_{13}$  material component with a failure index of 0.632. This value is the same as the maximum strain failure index from the failure theory comparison in Section 5.3 and is consistent with the failure index values from the laminate development tables. Regardless of the failure theory chosen for the analysis, Hyperworks determines bond failure using the comparison of interlaminar allowables. For this reason, a more in-depth analysis was performed to understand how the failure indices change in a three-dimensional stress state.

The critical ply failure indices for Tsai-Wu, Hashin and Maximum Strain theories were calculated from the material component stresses organized in Table 5.5.1 and Table 5.5.2 and substituted into the respective equations for three-dimensional stress states for the given failure method (Table 5.5.3 and Table 5.5.4).

*Table 5.5.3: Three-Dimensional Stress State Failure Analysis – Front Upright*

<b>Three-Dimensional Stress State - Front Upright</b>		
Failure Theory	Failure Index	Factor of Safety
Tsai-Wu	0.606	1.285
Hashin - Compressive Fiber	0.002e-1	5000.000
Hashin - Tensile Matrix	0.750	1.333
Max Strain	0.606	1.650

*Table 5.5.4: Three-Dimensional Stress State Failure Analysis – Rear Upright*

<b>Three-Dimensional Stress State - Rear Upright</b>		
Failure Theory	Failure Index	Factor of Safety
Tsai-Wu	0.502	1.411
Hashin - Compressive Fiber	0.002e-1	5000.000
Hashin - Compressive Matrix	0.950	1.053
Max Strain	0.632	1.582

The front and rear expanded analysis resulted in the highest failure indices within the Hashin matrix calculations with values of .749 and .949 (1.333 and 1.053 factor of safety), respectively. However, the Hashin fiber failure calculations result in a near zero failure index for the critical

ply at the extreme element. The Maximum Strain failure calculations are the same as the bond failure indices from Table 5.2.1, Table 5.2.3, Table 5.5.1 for the front upright and Table 5.2.2, Table 5.2.4 and Table 5.4.2 for the rear upright because they share the same independent material component comparisons, respectively. The Tsai-Wu factor of safety values cannot be considered the same as the Maximum Strain factor of safety values due to the difference in conversion from failure index to factor of safety ( $SF = 1/FI$  for Hashin and Maximum Strain compared to  $SF = 1/\sqrt{FI}$  for Tsai-Wu).

The three-dimensional stress state failure calculations further confirm that any failure of the front or rear upright is most likely to be because of tensile or compressive matrix failure at the extreme elements of the critical ply, as demonstrated by the higher than originally approximated bond failure index in the laminate development tables. While considering the calculation of Tsai-Wu factors of safety, the values agree that the largest contributors to the three-dimensional failure analysis calculation are attributed to the interlaminar shear stresses ( $F_{13}$  and  $F_{23}$  in Table 5.5.1 and Table 5.5.2). In plane stresses are an order of magnitude lower for the front and rear upright critical plies than any interlaminar stress at the most extreme element.

## **5.6. Analysis Discussion**

The results provided from the finite element analysis verifies that the design goal of the utilization of the same toolset to produce four unique structures has been met. Additionally, the finished products have achieved a lower weight in comparison to their full aluminum counterparts. The FEA model generated for the front and rear upright allowed for iterative design of the laminate for the prototype components. Further analysis could be performed to determine a more efficient laminate.

The initial analysis of the front and rear upright submits factors of safety that are within the FAA's recommended limits for protoflight components. Upright misalignment analysis propose that the manufactured front laminate could benefit from a slightly lowered failure index by rotating each ply five degrees while the rear upright would be within the recommended FS of 1.500 with up to a ten-degree ply misalignment while reducing the amount of camber compliance in cornering. The three-dimensional stress state failure calculations for the front and rear uprights provide a FS lower than advised from the FAA's recommendations for composite structures. However, both matrix failure indices are less than one, which would suggest the material would not fail given the analyzed loading scenarios.

When performing any sort of FEA it is important to understand how the program is predicting the output data of the model. Although steps were taken to extract tensorial stresses and calculate three-dimensional stress state failure, the load cases that were analyzed are at the limits of the vehicles performance and are not often sustained in duration. Additionally, the composite structure was being analyzed on its own without any of the fastened hardware which would contribute strength and stiffness to the assembled components. Finally, the FEA model utilizes several RBE2's to represent the interfacing suspension mounts on the upright. As a result, the constraints dictated by the model boundary conditions provide an artificially high stiffness to the nodes of the composite geometry.

## 6. Manufacturing

### 6.1. Molds and Tooling

The primary objective of the aluminum tooling is to be able to mold the composite structure of four unique components without any post machining operations. The mandrels had to be reconfigurable to manufacture front left, front right, rear left, and rear right uprights. To reduce the need for additional tooling, the front and rear uprights were designed to share the mandrels to form the upper ball joint and brake caliper mounting features. Mandrel configuration for one of the front uprights is shown in Figure 6.1.1 below.



*Figure 6.1.1: Tooling to Manufacture Front Left Upright*

The general layup process for the upright geometry occurs in two main stages. The tooling is used in conjunction with the layup of the global geometry of the part through the first cure. After the part is demolded, the local plies are added with the lateral stiffeners. The part is cured once again. The details of these processes are covered in the following sections. A streamlined description of the manufacturing process for the front and rear upright is available in Appendix B: Front and Rear Upright Manufacturing Overview



## **6.2. Composite Manufacturing Process**

Laminate manufacturing is broken down into the prepreg preparation, layup, and curing.

### **6.2.1. Lamina Preparation**

As mentioned in chapter four, prepreg carbon fiber was chosen due to ease of manufacturability, material availability to the project, and savings in time with respect to material preparation. Material is stored in a frozen state to preserve the life of the resin and removed from storage only prior to manufacturing of the component. After the material has reached room temperature, plies are cut and organized per the build specification for the layup process. Ply templates were generated using SolidWorks by extracting the relevant surfaces from the three-dimensional geometry. Once the surfaces are extracted, they are flattened to create the appropriate area and curvature of the plies. Next, the plies are extended by ¼” in each direction to allow for adequate overlap between adjacent plies and runout past the trimmed edge of the finished part. Finally, the templates are converted to a 1:1 scale for print and use in cutting of the material. If resources and time had allowed, a ply generation software would have been used to control ply taper and fiber alignment more precisely. The plies would then have been imported into a CNC plotting program and oriented to be cut per the layup specification.

### **6.2.2. Layup**

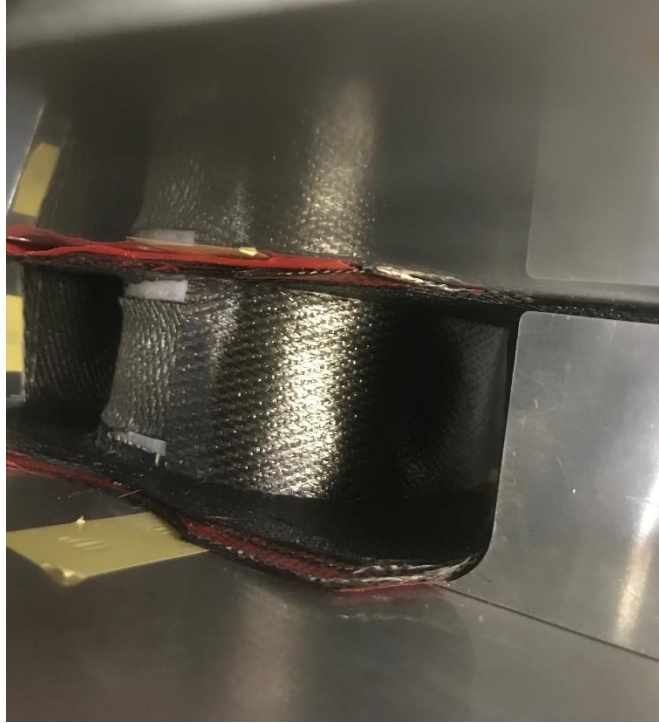
The manufacturing process for the front and rear uprights follow the same general steps. Plies are placed onto the aluminum tool halves per their respective stacking sequence. The same stacking sequence is implemented on the mandrels that are brought in after the two halves of the tool are bolted together. Those being the steer/toe, brake caliper, and rear upright lower ball joint mandrels. Release film from the prepreg is placed between the plies on the regions interfacing

with the secondary mandrels to allow for the material to be manipulated during installation (Figure 6.2.2.1).



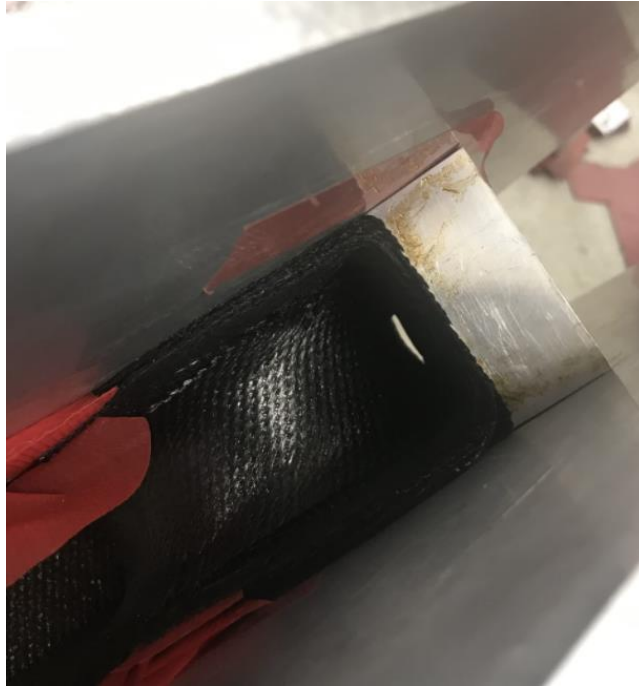
*Figure 6.2.2.1: Joining of Both Sides of Tool*

After the two halves of the tool are fastened together, material is installed circumferentially around the bearing mandrel to join the inside and outside surfaces of the part (Figure 6.2.2.2). The upper and lower ball joint geometry is created for the front upright as the eight global plies are brought together and sandwiched between the aluminum tooling. A similar effect is created for the rear upright with respect to the upper ball joint with plies five through eight being dropped locally. The lower ball joint mount is formed in a similar manner to the steering/toe and brake caliper features.



*Figure 6.2.2.2: Joining of Inside and Outside Laminates*

Once the bearing housing plies are applied to the tool, the part is prepared for the secondary mandrels to be installed. The general procedure is the same for the brake caliper, steering/toe mandrel, and the lower ball joint of the rear upright. The release film is removed layer by layer alternating from inside to outside tool surface and the prepreg is folded toward the inside of the part. The secondary mandrels are brought into contact with the surface plies to create a single lap joint. After the feature is bolted into place, the composite material is brought together. An example of the joining process is depicted in Figure 6.2.2.3. This process is repeated until all the mandrels are in place and the prepreg is positioned against the tool surface.



*Figure 6.2.2.3: Brake Mandrel Installed to Tool*

After every ply is installed peel ply is applied to the inside surfaces of the part that are not in contact with the tool. Peel ply is a material used to create a textured surface for bonding of the prepreg composite in the secondary layup. It is removed from the part after the cure cycle is completed. After the peel ply is positioned, perforated release film is applied to allow the laminate to evacuate air and volatiles during cure without adhering to the breather cloth. Breather cloth is wrapped around the edge of the tool and worked into the cavities of the part. The breather cloth allows for the creation of an air passage circuit from the vacuum pump to the laminate. Next, the assembly is transitioned into an Airtech Stretchlon 850 vacuum bag. The Stretchlon material is chosen for its high elongation at break (450%) and thermal limit (400°F) [36] to ensure the bagging film extends deep into any voids of the part to prevent bridging and film failure during autoclave cure. The assembly is placed in the oven at 125°F under vacuum for two hours to allow the material to debulk (Figure 6.2.2.4). Debulking of

the laminate allows for the plies to consolidate to the tool after which the vacuum bag material can be rearranged into the cavities of the part in preparation for the autoclave cure cycle.



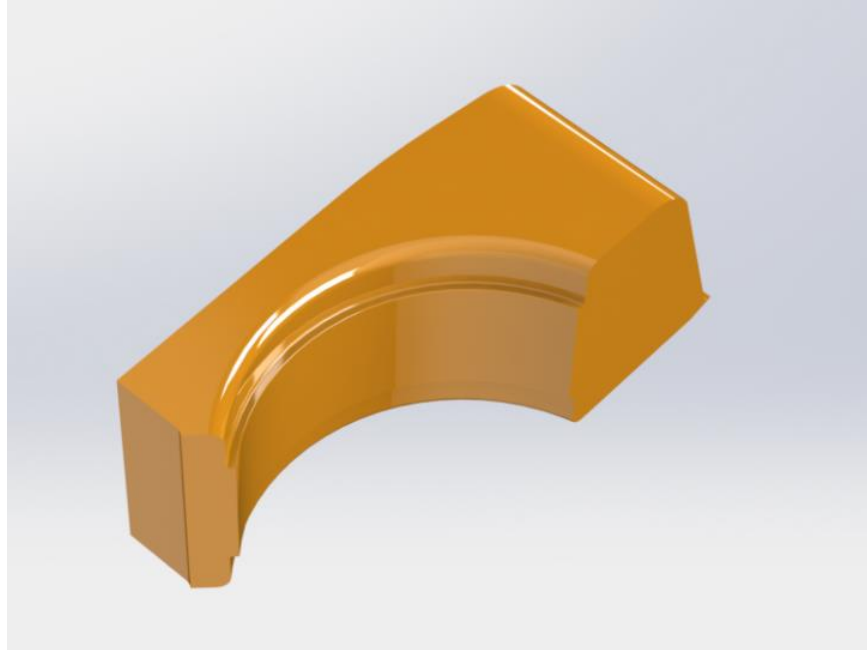
*Figure 6.2.2.4: Debulking of Composite in Oven*

The autoclave cure for this material takes approximately eight hours after which the vacuum bag material is removed from the cured part. Then the part is marked using a paper template to designate the trim line of the material. Trimming is carefully performed using a handheld rotary tool with a diamond edged bit. A solvent is used to remove the carbon dust and debris from the surfaces of the part. Local plies are added to the structure (Figure 6.2.2.5) in the location and orientation defined by the layup table (detailed in the engineering drawings in Appendix A: Left Front and Left Rear Engineering Drawings). These additional plies are installed to provide the required strength and bending stiffness to the structure. Perforated release film and breather cloth are applied to the part and is placed inside of the vacuum bag for its final autoclave cure.



*Figure 6.2.2.5: Application of Local Plies to Component*

The prototype build of the part required careful measuring and placement of the lateral stiffeners relative to the datum edges of the composite. The addition of a silicone tool set would have allowed for greater precision in ply placement and ease in the vacuum bagging process during the first and second stages of the layup. An example of one of these tools is demonstrated in Figure 6.2.2.6. Another benefit of utilizing silicone tooling is that the rubber will expand during cure and consolidate the laminate in hard to reach areas that a vacuum bag may not fully extend.



*Figure 6.2.2.6: Example of Supplemental Silicone Tool*

### **6.2.3. Laminate Cure**

The temperature ramp and dwell components of the cure cycle are based upon the manufacturing processes from the composite supplier (Figure 6.2.3.1). However, instead of utilizing a Vacuum Bag Only (VBO) cycle the part is cured in an autoclave. The elevated pressure of an autoclave compared to VBO cure is desirable for greater fiber consolidation and volatile evacuation of the laminate [6]. The additional pressure on the part aids in the composite conformity to the geometry of the tooled surface throughout the cure cycle.

The cure cycle begins at ambient temperature and full vacuum. The laminate is heated to 140°F at rate of  $\pm 5^\circ\text{F}$  while the pressure is increased to 85 psi at 5psi  $\pm 1$ psi per minute. for 120  $\pm 10$  minutes. The part is ramped to 250°F  $\pm 10^\circ\text{F}$  for 120 +/- 10 minutes at a rate of 2°F  $\pm 1^\circ\text{F}$  per minute. After the second dwell duration the laminate is ramped to 350°F  $\pm 10^\circ\text{F}$  for 120  $\pm 10$  minutes. Finally, the pressure is bled from the autoclave and the laminate can cool at no more than 10°F/minute to below 140°F when it can be removed from the autoclave.



Figure 6.2.3.1: Solvay 5320-1 Cure Cycle [18]

### 6.3. Final Processing

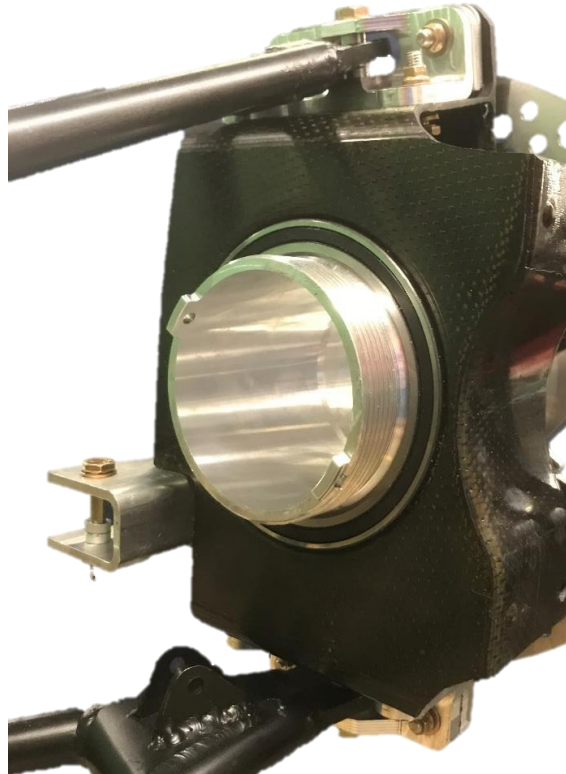
After the composite components are completely cured, there are two main steps that must occur prior to assembling of the components. First, the mounting holes for any interfacing mounts must be drilled. Second, the part periphery must be trimmed to its final dimension.

The untrimmed upright is placed back into the aluminum tools which act as a drill guide for the primary fastener locations. A carbide drill bit is run through the tool and part for each ball joint mount, steering/toe link, and brake caliper mounting location. The part is removed from the aluminum tool and the secondary drill mounts are fastened to the upper and lower ball joints and steer/toe link location (recall Figure 3.3.2). A carbide drill bit is used again to finish drilling the part. Next, the component is marked with a 1:1 scale template to designate the edge to be trimmed with a handheld rotary tool. After trimming is complete, the part can be cleaned with solvent and it is ready to be assembled. All the critical features have been formed during the composite cure to locate the outboard suspension mounts, house the wheel bearings, and no further post processing is required.

Before fastening mounts to the upright, the wheel bearings and wheel hub are installed into the part using a hydraulic press. To complete the upright assembly, the upper, lower ball



joint, and steering/toe mounts are fastened to the composite structure. An example of the assembled upright is provided below in Figure 6.3.1.



*Figure 6.3.1: Partially Assembled Front Corner Suspension Assembly*

After all mounts are fastened and properly torqued, the driveshaft (if rear upright) can be installed, and the component is attached to the suspension and steering/toe linkages. The brake rotor and caliper are installed, and fluid lines can be plumbed and bled for trapped air. Finally, the wheel speed sensor can be installed into the threaded housing that is bonded into the upright. An example of the assembled rear suspension corner is displayed in Figure 6.3.2.



*Figure 6.3.2: Fully Assembled Rear Upright*

## **7. Model Validation**

Finite element analysis is practical in design to predict strain response in various loading conditions without manufacturing and testing multiple configurations. However, the results obtained via analysis are simply an approximation that is dependent on the quality of the input conditions and component model. Additionally, variations may occur between the model and physical component due to model assumptions, material properties, and manufacturing deviations. To quantify the accuracy of the FEA model, physical testing must be performed.

The automotive industry employs specially designed test apparatus to simulate and measure suspension kinematics and compliance. These machines utilize a body clamping platform and wheel platforms that can be independently controlled with steering and brake actuators coupled with numerous load and displacement sensors. While the use of a kinematics and compliance test fixture would be ideal, the resources available at KU and JMS provided the means to validate the prototypes using a static lateral loading test.

### **7.1. Static Lateral Loading**

To determine the accuracy of the FEA model against the manufactured components a structural test was designed and performed on the front and rear quarter suspension assemblies. The FEA model utilized in the component development was modified to simulate an equivalent applied force for strain measurement at multiple locations to quantify the error in the analysis.

### **7.2. Methods**

A static structural test was designed to emulate a maximum lateral loading scenario on the front and rear quarter suspension assembly. JMS designed and manufactured a lateral load fixture that can be mounted to a 13" wheel and support a load at 3.1 feet from the tire. Utilizing the weights available in the JMS lab a moment of 550.7 ft-lb can be applied to the wheel

resulting in a lateral load magnitude of 495.3 lbf at the tire contact patch. The FEA model utilized for dynamic load cases was modified to replicate the applied load using the lateral load fixture. The JMS19C employs an overall vehicle weight of 456lb with a 45.7% front bias without driver. The front and rear half axle weight were applied as a vertical force with the lateral force from the fixture in the FEA model to determine strain distribution within the front and rear composite uprights. The applied loads are displayed in the table below.

*Table 7.2.1: FEA Load Cases*

<b>Lateral Load Test</b>			
Load Case	X -Longitudinal (lbf)	Y - Lateral (lbf)	Z - Vertical (lbf)
Front Contact Patch	0	-495.3	104.2
Rear Contact Patch	0	-495.3	123.8

Four locations were selected from the FEA model for comparison with the physical testing results. The locations and orientations were determined based on high strain regions and accessibility of strain gauge installation without complete disassembly of the vehicle (Figure 7.2.1, Figure 7.2.2, Figure 7.2.3, and Figure 7.2.4). Elemental strains were extracted from the outermost composite layer in the regions of choice and averaged over a surface area equivalent to the size of a strain gauge for comparison with the physical test results. An example of the strain query is displayed in Figure 7.2.5. The localized strain averages for the front and rear uprights are shown in Table 7.2.2.

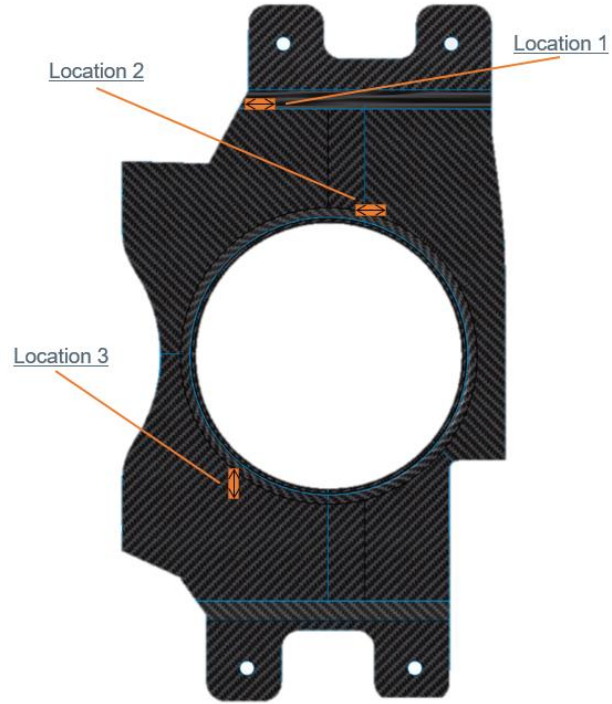


Figure 7.2.1: Strain Gauge Locations on Front Upright - Outboard

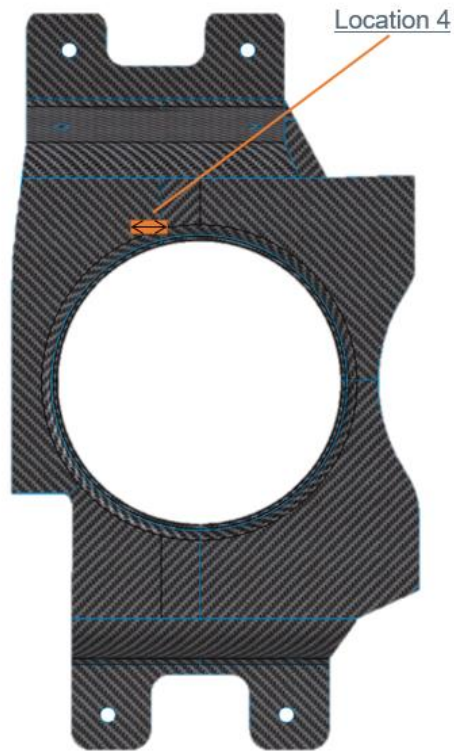


Figure 7.2.2: Strain Gauge Locations on Front Upright - Inboard

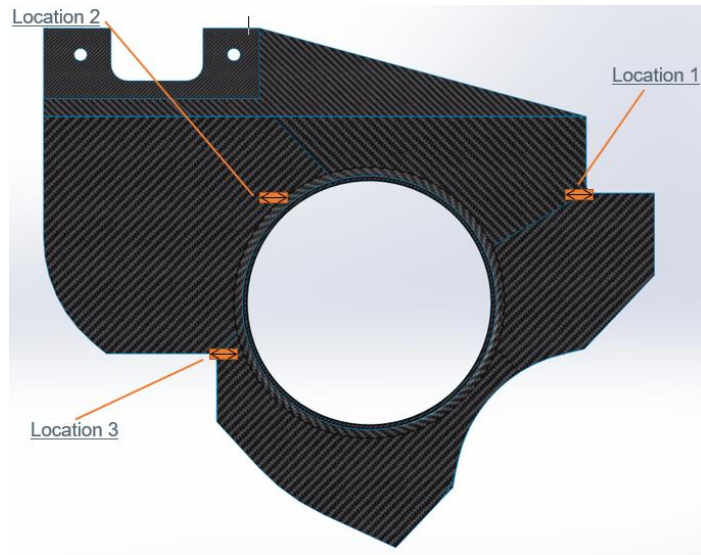


Figure 7.2.3: Strain Gauge Locations on Rear Upright - Outboard

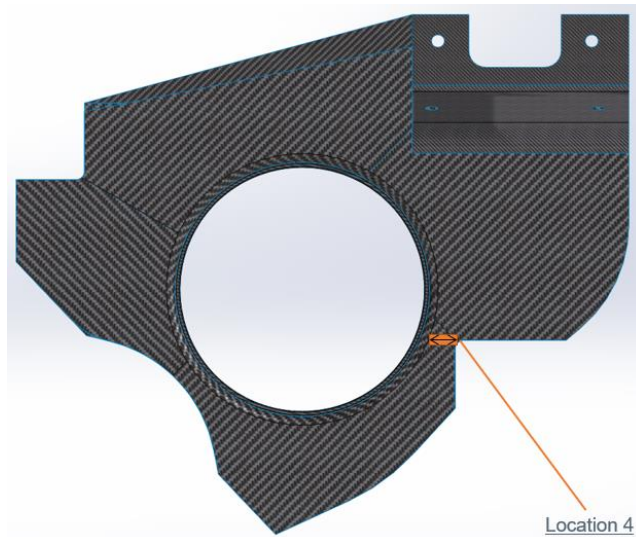


Figure 7.2.4: Strain Gauge Locations on Rear Upright - Inboard

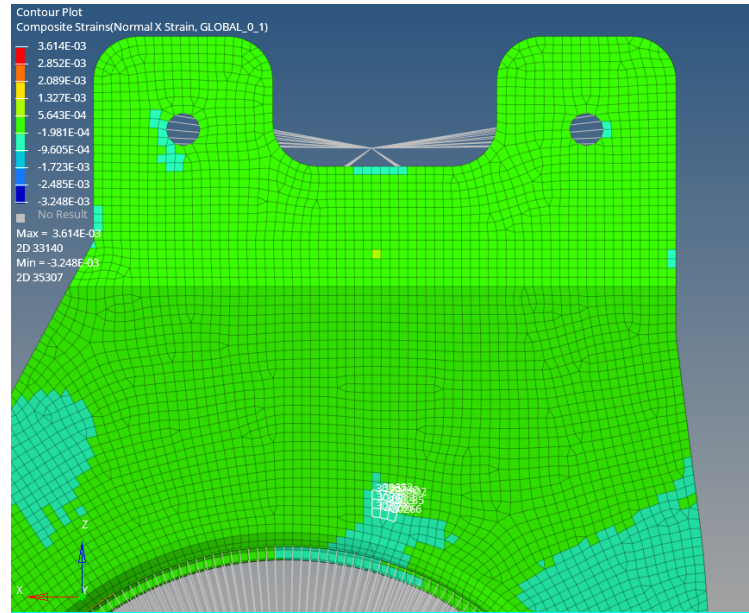


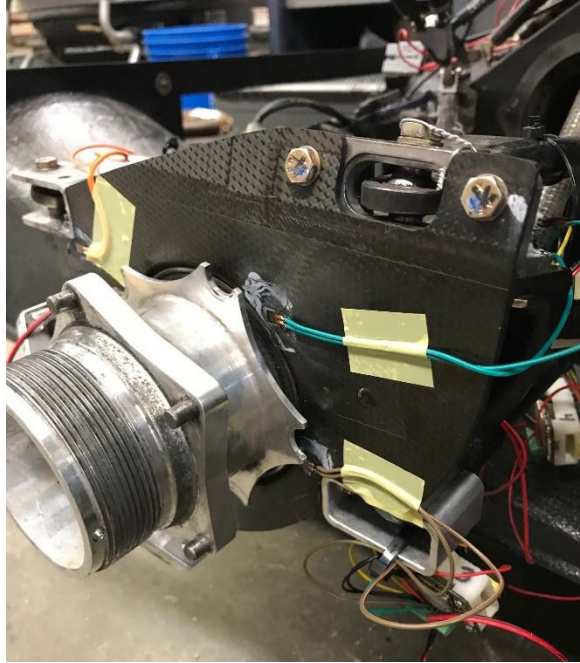
Figure 7.2.5: Example of Element Strain Averaging for Location Two on Front Upright

Table 7.2.2: Local Strain Averages for FEA Load Cases

	<b>FEA Results - Region Average Strain (<math>\mu\text{in/in}</math>)</b>			
	Location 1	Location 2	Location 3	Location 4
Front Upright	-247.9	-50.4	-415.3	557.4
Rear Upright	21.0	-461.7	1358.4	370.5

### 7.3. Procedure

The general-purpose strain gauges utilized for the test are a linear pattern that were appropriate for static and low-fatigue dynamic measurement on composite materials. The data was transmitted to the DAQ via two channel analog wireless nodes for simultaneous strain measurement during the test. Simple housings were designed and manufactured from printed acrylonitrile butadiene styrene (ABS) to contain the lithium-ion battery and wireless node and provide the means for attachment to the suspension linkage with cable ties. To prepare the parts for strain gauge application, the uprights were locally abraded with 600-grit silicon carbide paper and cleaned with denatured alcohol. The strain gauges were bonded to the surface with the M-Bond 200 adhesive via the procedure provided from MicroMeasurements [37].



*Figure 7.3.1: Strain Gauges Installed on Rear Upright*

To imitate the fixed constraints of the FEA model, the springs and dampers were replaced with solid steel links. Solid ABS spacers were placed on the steering rack to prevent rotation of the front wheels under load. The wireless nodes are a full Wheatstone bridge configuration which necessitated each active gauge on the upright to be wired in a quarter-bridge formation for strain measurement. Three passive strain gauges were bonded to a small sample of composite attached to the sensor housing to complete the full bridge configuration of each node. After each gauge was verified for continuity and resistance the wireless nodes were calibrated in the Lord SensorConnect application using the strain gauge specifications provided from Micromasurements without load on the vehicle. Once the calibration was complete the lateral load fixture was placed on the wheel and the load was applied incrementally.





*Figure 7.3.2: Maximum Lateral Load on Front Quarter Assembly*

The front and rear quarter suspension assemblies were loaded and unloaded in three independent trials with the wheel and tire placed on a roller plate to minimize the frictional force of the tire on the ground. Strain data was recorded simultaneously for each strain gauge for the duration of each trial. Individual gauge data was averaged for the three trials to provide the results displayed in Table 7.3.1 and Table 7.3.2 for front and rear quarter suspension assemblies, respectively.

Table 7.3.1: Averaged Strain Data from Lateral Loading of Front Quarter Assembly

Trial Average						
Load	Distance	Moment	Strain 1	Strain 2	Strain 3	Strain 4
(lb)	(ft)	(ft-lb)	( $\mu\text{in/in}$ )	( $\mu\text{in/in}$ )	( $\mu\text{in/in}$ )	( $\mu\text{in/in}$ )
0	3.1	0	0	0	0	0
10.2	3.1	31.4	-18.3	-0.7	-22.3	38.3
20.4	3.1	62.8	-36.7	-1.7	-52.3	73.3
35.4	3.1	109.0	-68.3	0.0	-89.7	121.7
71.4	3.1	219.9	-146.7	-28.3	-179.0	240.0
108.4	3.1	333.9	-236.7	-73.3	-247.3	348.3
144.2	3.1	444.1	-330.0	-66.7	-317.3	443.3
<b>178.8</b>	<b>3.1</b>	<b>550.7</b>	<b>-421.7</b>	<b>-46.7</b>	<b>-389.0</b>	<b>531.7</b>
144.2	3.1	444.1	-351.7	-80.0	-307.3	451.7
108.4	3.1	333.9	-266.7	-110.0	-230.7	363.3
71.4	3.1	219.9	-178.3	-113.3	-145.7	238.3
35.4	3.1	109.0	-86.7	-61.7	-64.0	110.0
20.4	3.1	62.8	-56.7	-53.3	-32.3	61.7
10.2	3.1	31.4	-31.0	-40.0	-7.3	30.0
0	3.1	0	-5.0	-18.3	-12.7	3.3

Table 7.3.2: Averaged Strain Data from Lateral Loading of Rear Quarter Assembly

Trial Average						
Load	Distance	Moment	Strain 1	Strain 2	Strain 3	Strain 4
(lb)	(ft)	(ft-lb)	( $\mu\text{in/in}$ )	( $\mu\text{in/in}$ )	( $\mu\text{in/in}$ )	( $\mu\text{in/in}$ )
0	3.1	0	0	0	0	0
10.2	3.1	31.4	5.7	-17.3	43.0	13.0
20.4	3.1	62.8	10.3	-33.3	91.7	26.7
35.4	3.1	109.0	13.0	-66.7	126.7	53.7
71.4	3.1	219.9	24.3	-146.7	433.3	123.3
108.4	3.1	333.9	39.3	-237.7	693.3	195.0
144.2	3.1	444.1	49.7	-325.0	951.7	265.0
<b>178.8</b>	<b>3.1</b>	<b>550.7</b>	<b>55.3</b>	<b>-405.0</b>	<b>1200.0</b>	<b>320.0</b>
144.2	3.1	444.1	42.7	-361.7	1065.0	282.7
108.4	3.1	333.9	27.0	-305.0	895.7	236.7
71.4	3.1	219.9	18.3	-218.3	696.7	173.3
35.4	3.1	109.0	2.7	-125.0	450.0	99.0
20.4	3.1	62.8	0.3	-76.7	495.0	58.3
10.2	3.1	31.4	3.3	-44.3	180.0	25.7
0	3.1	0	2.3	-10.0	50.7	2.3

The front and rear uprights were loaded up to a moment of 550.7 ft-lb which resulted in the maximum strain values for any given gauge location on the component. These values are emboldened in their respective tables and compared against the FEA results.

## 7.4. Results

The strain approximations from the FEA models are compared against the physical measurements obtained from testing in Table 7.4.1 and Table 7.4.2.

*Table 7.4.1: Front Upright Strain Comparison – FEA vs Experimental*

<b>FEA Results - Region Average (<math>\mu\text{in/in}</math>)</b>			
<b>Location 1</b>	<b>Location 2</b>	<b>Location 3</b>	<b>Location 4</b>
-247.9	-50.4	-415.3	557.4
<b>Physical Testing - Strain Gauge Measurement (<math>\mu\text{in/in}</math>)</b>			
-421.7	-46.7	-389.0	531.7
<b>Measured Strain Deviation from Analysis (%)</b>			
41.2	-7.9	-6.8	-4.8

Testing results from the front upright deviate from the FEA model -6.8% to 41.2% for any given maximum strain gauge measurement with an average error of 5.4% from the FEA model (Table 7.4.1). The rear upright maximum strain measurements demonstrate a deviation range of -15.8% to 62.0% from the FEA model with an average of 4.8% (Table 7.4.2). These deviations could be attributed to realization of ply layup compared to the FEA model, misalignment of strain gauge orientation to part geometry, variation in load distribution from the aluminum mounts to the composite structure in comparison to FEA model, and/or compliance from the entire quarter suspension assembly.

*Table 7.4.2: Rear Upright Strain Comparison – FEA vs Experimental*

<b>FEA Results – Region Average (<math>\mu\text{in/in}</math>)</b>			
<b>Location 1</b>	<b>Location 2</b>	<b>Location 3</b>	<b>Location 4</b>
21.0	-461.7	1358.4	370.5
<b>Physical Testing – Strain Gauge Measurement (<math>\mu\text{in/in}</math>)</b>			
55.3	-405.0	1200.0	320.0
<b>Measured Strain Deviation from Analysis (%)</b>			
62.0	-14.0	-13.2	-15.8

To measure the accuracy of the strain gauge placement in comparison to the FEA model, a follow up study was performed. For any given strain gauge location, the subset of elements utilized to determine the average strain reading were shifted two elements (approximately 0.10”

or half a gauge width) in any direction. Positional strain gauge error from the FEA model is organized in Table 7.4.3 and Table 7.4.4.

*Table 7.4.3: Front Upright FEA Positional Strain Error*

<b>FEA Positional Error – Front Upright</b>				
<b>Δposition (inch)</b>	<b>Location 1 (μin/in)</b>	<b>Location 2 (μin/in)</b>	<b>Location 3 (μin/in)</b>	<b>Location 4 (μin/in)</b>
<b>0.1 Left</b>	-211.5	5.3	-247.5	364.5
<b>0.1 Right</b>	-193.4	-166.7	-578.9	815.0
<b>0.1 Up</b>	-206.3	-70.8	-370.8	235.8
<b>0.1 Down</b>	-222.2	66.5	-436.9	735.5
<b>Average</b>	-208.3	-41.4	-408.5	537.7
<b>Average Error in Measurement (%)</b>				
-	-16.0	-17.7	-1.6	-3.5

*Table 7.4.4: Rear Upright FEA Positional Strain Error*

<b>FEA Positional Error – Rear Upright</b>				
<b>Δposition (inch)</b>	<b>Location 1 (μin/in)</b>	<b>Location 2 (μin/in)</b>	<b>Location 3 (μin/in)</b>	<b>Location 4 (μin/in)</b>
<b>0.1 Left</b>	15.5	-355.5	828.1	466.0
<b>0.1 Right</b>	-0.9	-461.6	1612.9	248.0
<b>0.1 Up</b>	-20.5	-365.6	1126.5	344.3
<b>0.1 Down</b>	21.0	-289.7	1352.0	293.1
<b>Average</b>	3.8	-368.1	1229.9	337.8
<b>Average Error in Measurement (%)</b>				
-	-82.1	-20.3	-9.5	-8.8

The averaged positional error for the front upright ranges from -17.7% to -1.6% with an overall average of -9.7% in comparison to the baseline FEA results. The averaged positional error for the rear upright ranges from -82.1% to -8.8% in comparison with the baseline FEA results with an average of -30.2%. For any strain gauge location, the magnitude of the average strain is lower than the baseline FEA model suggesting that any difference in the strain gauge application location from the queried elements would not be detrimental in the assessment of the structural integrity of the uprights as manufactured.

To further investigate the FEA results, an isolated structural fixture could be implemented with a uniaxial testing machine to eliminate compliance contributions from interfacing components or load distribution variation from FEA model to as-manufactured geometry. Dynamic testing on the vehicle is another option to validate the results of load cases that were analyzed. Additionally, this dynamic testing could be expanded to validating the input conditions from the quarter-vehicle numerical model.

## 8. Conclusions

The components developed throughout the design, analysis, manufacturing, and physical testing of this project verify that a complex machined structure on a FSAE vehicle can be redesigned as an efficient additively manufactured structure using CFRP. The front and rear composite upright designs met the original goal of utilizing a modular toolset to produce four unique geometries while reducing weight by 55.0% in comparison to the 2017 and 20.0% compared to the 2016 full aluminum designs while maintaining structural fidelity in all dynamic load cases.

Although a composite with more favorable shelf life could have been utilized, material testing provided the means for the development of the manufacturing method using a composite that may have otherwise been left to waste. An even more efficient and lightweight structure can be produced using the methods developed in this project with a composite inside of its usable shelf life. Despite the reduction in material strength when compared to manufacturers specification, the FEA results demonstrate that adequate strength is maintained at all limit load cases with minimum factors of safety of 1.650 and 1.582 for the front and rear uprights, respectfully. Three-dimensional stress state analysis suggested a Tsai-Wu factor of safety of 1.285 for the front upright and a Hashin factor of safety of 1.053 for the rear upright. These safety factors are less conservative than the FAA recommended guidelines but do not exceed the failure criteria for the material model and are therefore acceptable for the composite prototype designs. A static structural test on the front and rear quarter suspension assemblies was performed to verify the integrity of the material model and correlates with the FEA model and generally suggests that the parts manufactured were more robust than initially analyzed. If time and resources allowed, expanded testing in static

lateral loading could verify FEA model stiffness. Furthermore, dynamic load testing with additional strain gauges on suspension linkages could provide greater insight into accuracy of not only the FEA model but the accuracy of input forces to the analysis.

The simplicity of the modular tooling and FEA model for the uprights provides the means for further development using resources available to the JMS FSAE team. Machining complexity and dependence on outside suppliers to the team are reduced thus providing additional resources for other components to be manufactured or extra time for testing on track. As a result, this helps to improve the overall vehicle performance in competition. The modular toolset allows for minor changes to suspension geometry or hub design to be achieved with minimal complexity and barrier to entry. The added benefits of utilizing a composite for the front and rear uprights not only gives the team the ability to capitalize on the greater strength to weight ratio of CFRP but to progress the cutting-edge engineering of the JMS FSAE vehicle.

## References

- [1] Society of Automotive Engineers (SAE), "Formula SAE Rules", 2019
- [2] SAE International Surface Vehicle Information Report, "SIGN CONVENTION FOR VEHICLE CRASH TESTING." SAE Standard J1733, Rev. Dec. 1994.
- [3] Milliken, William F., and Milliken, Douglas L. "Race Car Vehicle Dynamics." (Warrendale, PA: Society of Automotive Engineers, 1994).
- [4] Gillespie, T. D. "Fundamentals of Vehicle Dynamics." (Warrendale, PA: Society of Automotive Engineers, 1992).
- [5] Blundell, Mike and Harty, Damien. "The Multibody Systems Approach to Vehicle Dynamics, First Edition." (Warrendale, PA: Society of Automotive Engineers, 2004).
- [6] Jones, Robert M. "Mechanics of Composite Materials. 2nd ed." Philadelphia, PA: Taylor & Francis, 1999.
- [7] Callister, Jr., William D. and Rethwisch, David G. "Fundamentals of Materials Science and Engineering: An Integrated Approach. 4<sup>th</sup> ed." Hoboken, NJ: Wiley, 2012.
- [8] Mallick, P.K. "Fiber-Reinforced Composites. Materials, Manufacturing, and Design. 3<sup>rd</sup> ed." Boca Raton, FL: Taylor & Francis, 2008.
- [9] Ahlgren, Austin. "Analysis Process." 2017.
- [10] Sullivan, Rogelio. "Automotive Carbon Fiber: Opportunities and Challenges." JOM 58, no. 11 (2006): 77-79.
- [11] "Hybrid carbon fiber/aluminum suspension knuckle" CompositesWorld: Mar. 2017.
- [12] "Composite-lightweight rear suspension knuckle for a high-volume passenger vehicle." 2017.



- [13] Budynas, Richard G., and Nisbett, J. Keith. "Shigley's Mechanical Engineering Design. 10<sup>th</sup> ed." New York, NY: McGraw-Hill Education, 2015.
- [14] SKF. "Deep groove ball bearings, 61815-2RS1. Technical Data Sheet.
- [15] ASM Handbook Committee. "Properties and Selection: Nonferrous Alloys and Special-Purpose Materials (Volume 2)." 1990,  
<https://doi.org/10.31399/asm.hb.v02.9781627081627>.
- [16] Carbas, R.J.C, L.F.M Da Silva, E.A.S Marques, and A.M Lopes. "Effect of Post-cure on the Glass Transition Temperature and Mechanical Properties of Epoxy Adhesives." *Journal of Adhesion Science and Technology* 27, no. 23 (2013): 2542-557
- [17] ASTM Standard E1356. "Standard Test Method for Assignment of the Glass Transition Temperatures by Differential Scanning Calorimetry." ASTM International, 2014.
- [18] Solvay. "CYCOM 5320-1 Prepreg." Technical Data Sheet, 2016.
- [19] Man, Michelle. "Cytec Cycom 5320-1 T650 3k-PW Fabric Qualification Material Property Data Report." Wichita, KS: National Center for Advanced Materials Performance, 2015.
- [20] Park Electrochemical Corp. "E-765 Epoxy Prepregs, Rev. 10\_12." Technical Data Sheet.
- [21] Gurit. "SE 70 Low Temperature Cure High Toughness Epoxy Prepreg System." General Datasheet.
- [22] Tomblin, J., Ng, Raju, and National Inst FOR Aviation Research Wichita KS. "Material Qualification and Equivalency for Polymer Matrix Composite Material Systems", 2001.
- [23] Department of Defense. "Composite Materials Handbook Volume 3. Polymer Matrix Composites Materials Usage, Design, and Analysis (MIL-HDBK-17-3F)." Handbook, 2002.

- [24] ASTM Standard D3909. "Standard Test Method for Tensile Properties of Polymer Matrix Composite Materials." ASTM International, 2000.
- [25] ASTM Standard D2344. "Standard Test Method for Short-Beam Strength of Polymer Matrix Composite Materials and Their Laminates." ASTM International, 2000.
- [26] ASTM Standard D3171. "Standard Test Methods for Constituent Content of Composite Materials." ASTM International, 2015.
- [27] Cytec. "Thornel T-650/35 PAN-Based Fiber." Technical Data Sheet, 2012.
- [28] Sharp, Nathan, Johnathan Goodsell, and Anthony Favaloro. "Measuring Fiber Orientation of Elliptical Fibers from Optical Microscopy." *Journal of Composites Science* 3, no. 1 (2019): 23.
- [29] Chandrakala, Kunchi, Avadhanam Vanaja, and Rmvgk Rao. "Storage Life Studies on RT Cure Glass—Epoxy Pre-pregs." *Journal of Reinforced Plastics and Composites* 28, no. 16 (2009): 1987-997.
- [30] Altair University. "Introduction to Practical Aspects of Composite." Troy, MI: Altair Engineering, 2018.
- [31] United States. Federal Aviation Administration. Office of Commercial Space Transportation, FAA Ast, and Ast. *Guide to Verifying Safety-critical Structures for Reusable Launch and Reentry Vehicles*. Version 1.0. ed. Washington, DC: Federal Aviation Administration, Commercial Space Transportation, 2005.
- [32] Waddoups, M. E." *Advanced Composite Material Mechanics for the Design and Stress Analyst*." Fort Worth, TX: General Dynamics, 1974.
- [33] Tsai, S. W. and E. M. Wu. "A General Theory of Strength for Anisotropic Materials." *Journal of Composite Materials*, 1971.

[34] HyperWorks Online Help. "OptiStruct > User's Guide > Elements." Altair Engineering.

[35] Hashin, Z. "Failure Criteria for Unidirectional Fiber Composites." Journal of Applied Mechanics, 1980.

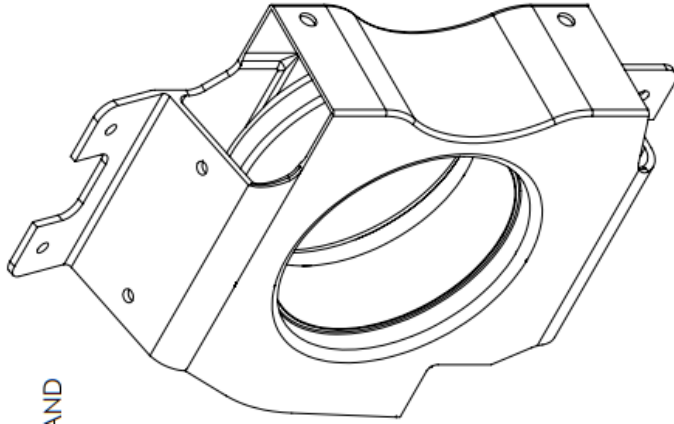
[36] "Stretchlon." Airtech Advanced Materials Group, 2005.

[37] Micro-Measurements. "Strain Gauge Adhesive." Vishay Precision Group, Inc., 2017.

**Appendix A: Left Front and Left Rear Engineering Drawings**

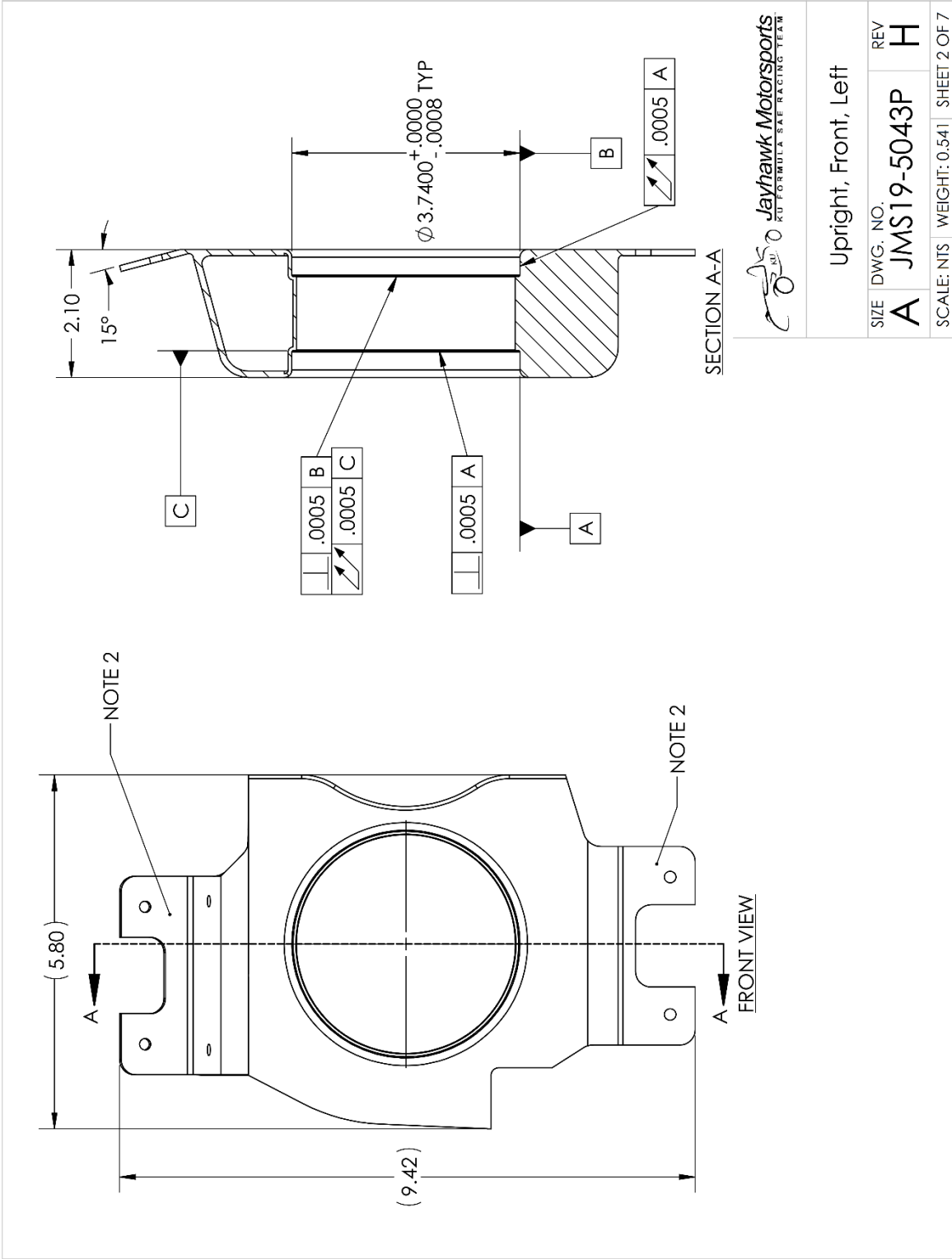
**NOTES:**

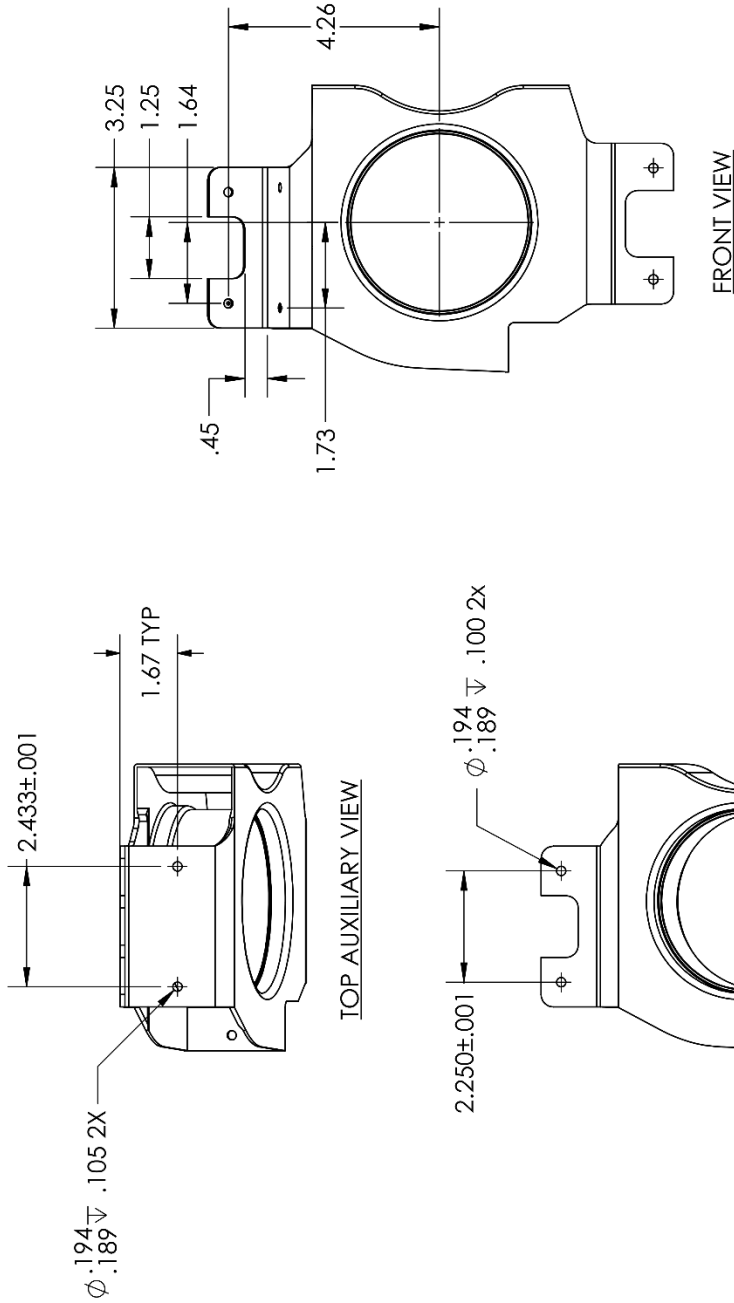
1. PART THICKNESS DEFINED BY PLY LAYOUT TABLE.
2. GLOBAL PLYS 1-4 ARE 2X ONLY IN REGIONS DEFINED BY JOINING OF INBOARD AND OUTBOARD SURFACES OF PART. REFER TO MANUFACTURING PROCEDURE FOR ADDITIONAL DETAILS.
3. JMS-50099 SHALL BE USED TO DEFINE PART SURFACE GEOMETRY.
4. HOLE POSITION DETERMINED BY TOOLING.
  - UPPER BALL JOINT: JMS-50104 (PRIMARY) AND JMS-50110 (SECONDARY)
  - LOWER BALL JOINT: JMS-50106 (PRIMARY) AND JMS-50112 (SECONDARY)
  - STEERING: JMS-50105 (PRIMARY) AND JMS-50111 (SECONDARY)
  - BRAKE: JMS-50108
5. PLY ID #1 OF LAYOUT TABLE BEGINS AT TOOLED SURFACE OF PART.
6. PART PERIPHERY TOLERANCE SHALL BE 0.05" TO TRIM TEMPLATE.



PLY ID	LOCATION	ORIENTATION	THICKNESS
1	GLOBAL	0/90	0.015
2	GLOBAL	±45	0.015
3	GLOBAL	±45	0.015
4	GLOBAL	0/90	0.015
5	LOCAL	0/90	0.015
6	LOCAL	±45	0.015
7	LOCAL	0/90	0.015

 Jayhawk Motorsports <small>FOR FORMULA SAERACING TEAM</small>		Upright, Front, Left	REV <b>H</b>
DRAWN	NMD	DATE	2/20/19
CHECKED			
ENG APPR.	RMS		3/13/19
MFG APPR.			
MFR			
UNLESS OTHERWISE SPECIFIED: DIMENSIONS ARE IN INCHES TOLERANCES: ANGULAR: ±.5° ONE PLACE DECIMAL: ±.1 TWO PLACE DECIMAL: ±.01 THREE PLACE DECIMAL: ±.005		COMMENTS: REMOVE SHARP EDGES	
MATERIAL CYTEC 5320-1 3K 8HS		FINISH SEE NOTES	
DO NOT SCALE DRAWING			
		<b>PROPRIETARY AND CONFIDENTIAL</b> THE INFORMATION CONTAINED IN THIS DRAWING IS THE SOLE PROPERTY OF JAYHAWK MOTORSPORTS. ANY REPRODUCTION IN PART OR AS A WHOLE WITHOUT THE WRITTEN PERMISSION OF JAYHAWK MOTORSPORTS IS PROHIBITED.	
SCALE: NTS		WEIGHT: 0.541	SHEET 1 OF 7



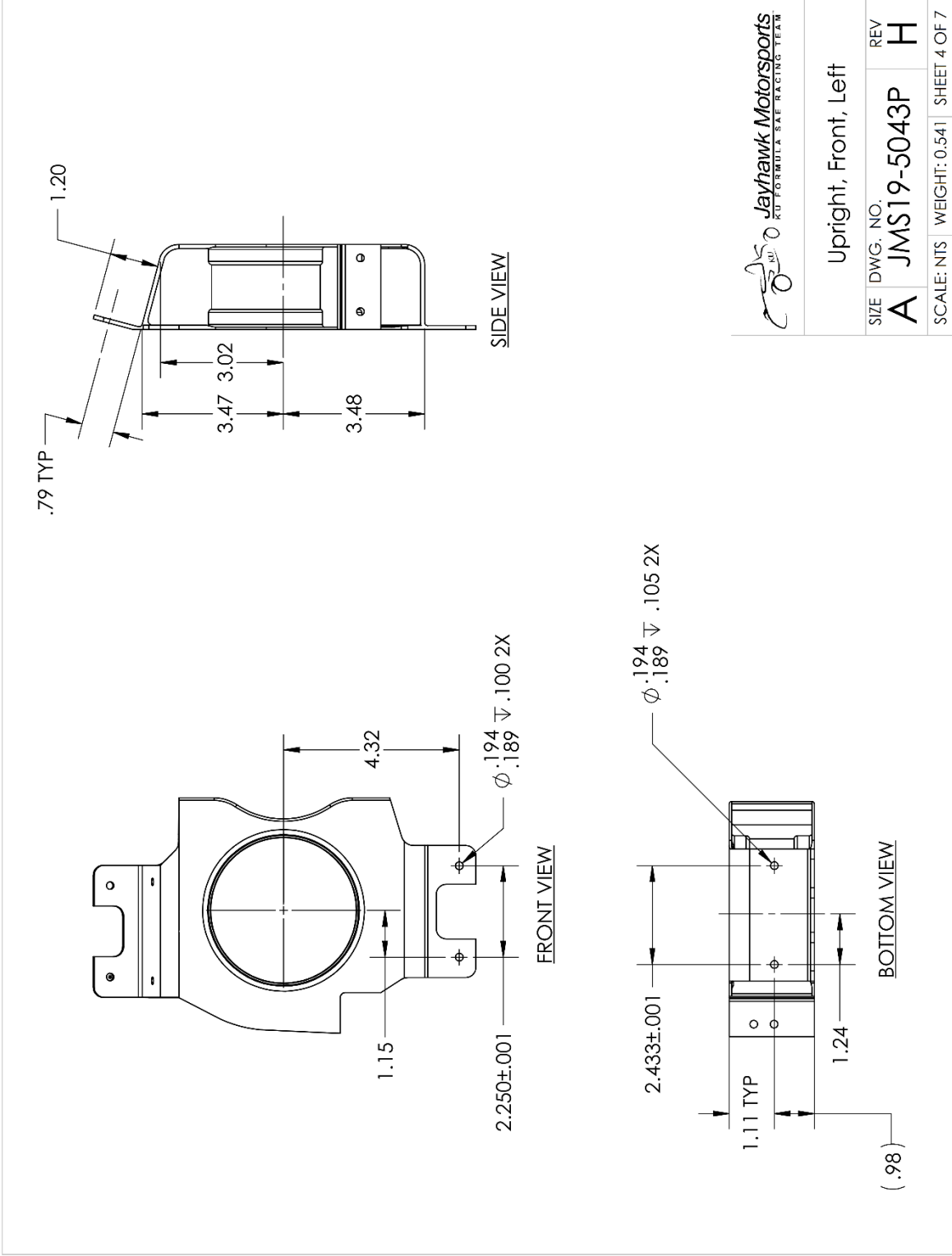


Upright, Front, Left

SIZE	DWG. NO.	REV
A	JMS19-5043P	H

SCALE: NTS WEIGHT: 0.541 SHEET 3 OF 7

SOLIDWORKS Educational Product. For Instructional Use Only.



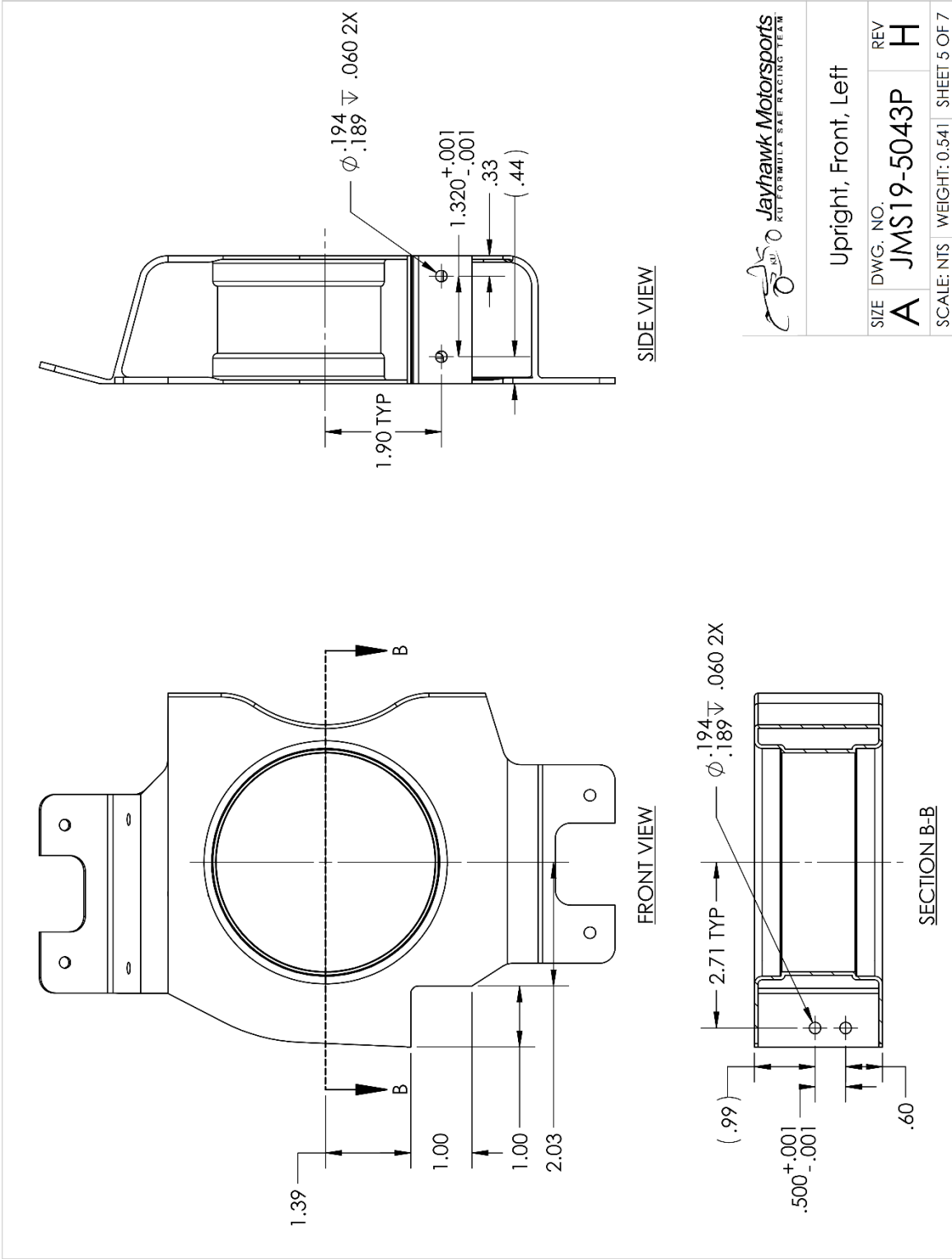
Upright, Front, Left

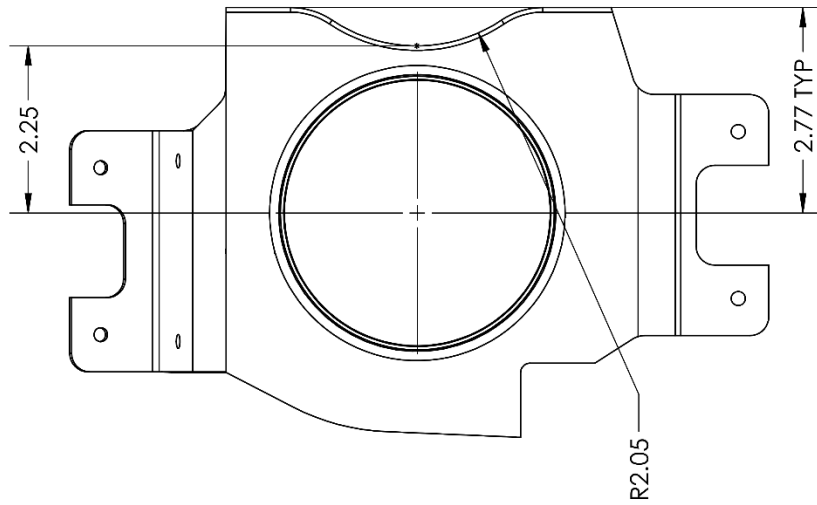
SIZE	DWG. NO.	REV
A	JMS19-5043P	H

SCALE: NTS WEIGHT: 0.541 SHEET 4 OF 7

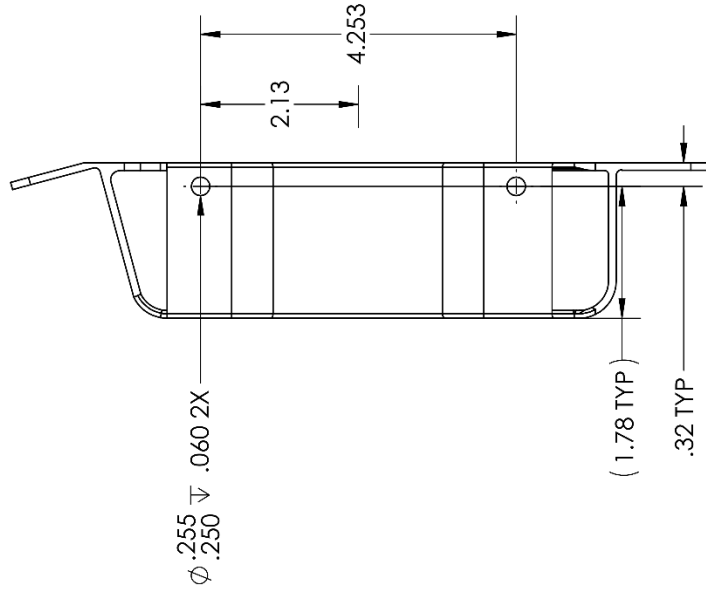
SOLIDWORKS Educational Product. For Instructional Use Only.







FRONT VIEW



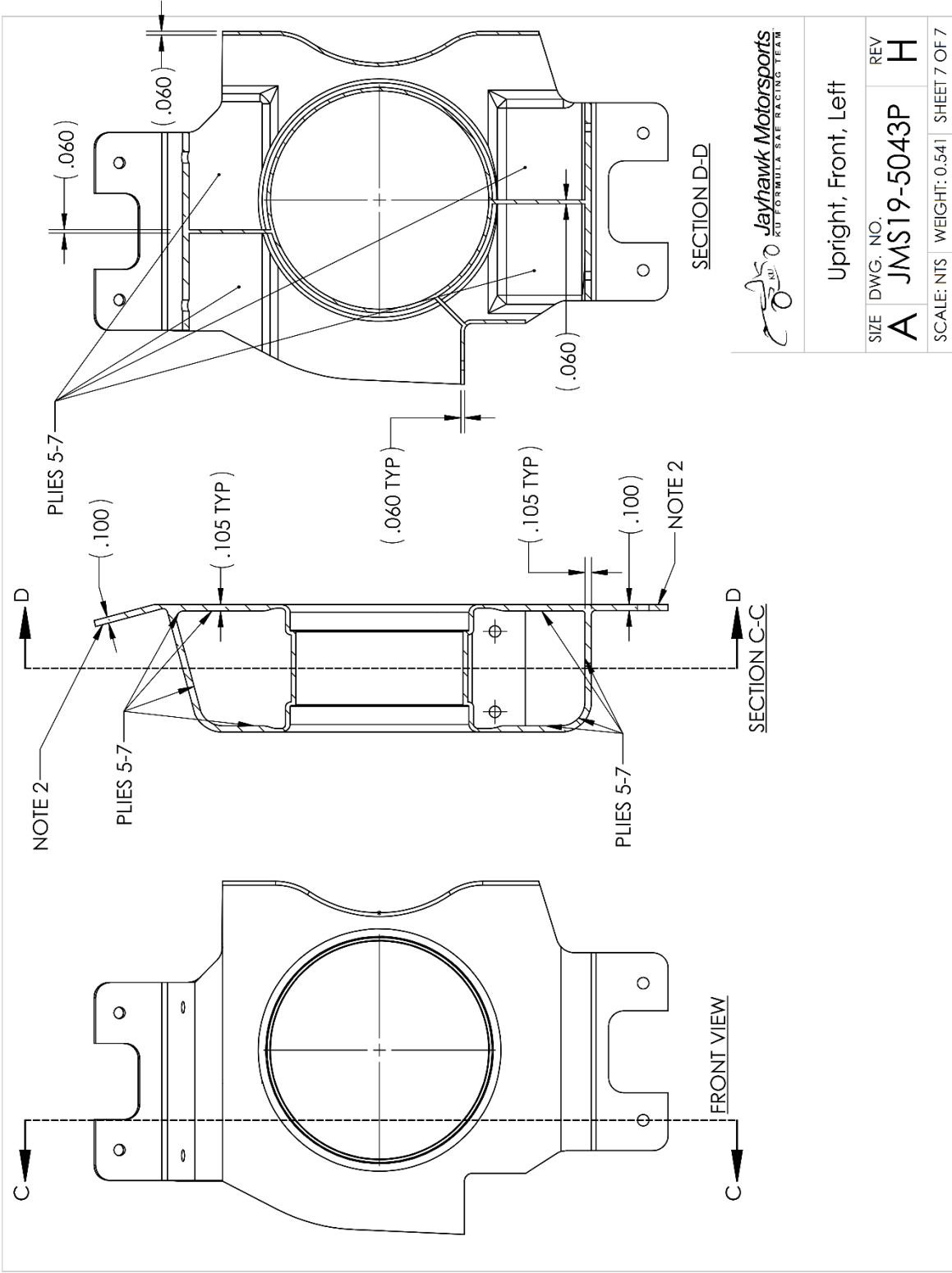
SIDE VIEW



Upright, Front, Left

SIZE	DWG. NO.	REV
A	JMS19-5043P	H

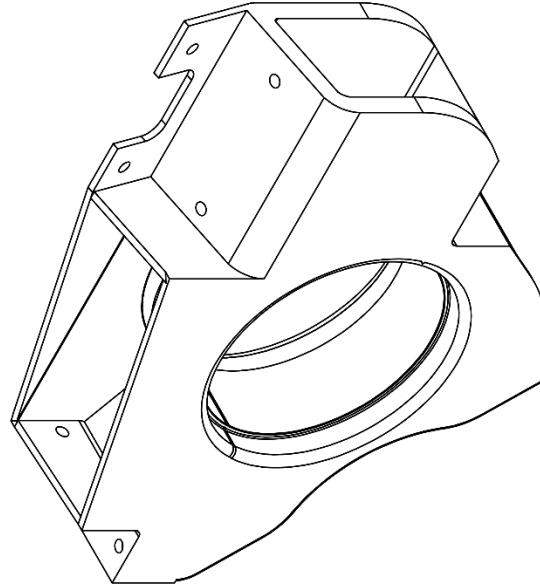
SCALE: NTS	WEIGHT: 0.541	SHEET 6 OF 7
------------	---------------	--------------



SOLIDWORKS Educational Product. For Instructional Use Only.

**NOTES:**

1. PART THICKNESS DEFINED BY PLY LAYUP TABLE. SURFACE MODEL SHOWN.
2. JMS-50099 SHALL BE USED TO DEFINE PART SURFACE GEOMETRY.
3. HOLE POSITION DETERMINED BY TOOLING.
  - UPPER BALL JOINT: JMS-50104 (PRIMARY) AND JMS-50114 (SECONDARY)
  - LOWER BALL JOINT: JMS-50107 (PRIMARY) AND JMS-50115 (SECONDARY)
  - TOE LINK: JMS-50105 (PRIMARY) AND JMS-50113 (SECONDARY)
  - BRAKE: JMS-50108
4. PLY ID #1 OF LAYUP TABLE BEGINS AT TOOLED SURFACE OF PART.
5. PART PERIPHERY TOLERANCE SHALL BE 0.05" TO TRIM TEMPLATE.



ISOMETRIC VIEW

PLY ID	LOCATION	ORIENTATION	THICKNESS
1	GLOBAL	±45	0.015
2	GLOBAL	0/90	0.015
3	GLOBAL	±45	0.015
4	GLOBAL	0/90	0.015
5	GLOBAL	0/90	0.015
6	GLOBAL	±45	0.015
7	GLOBAL	0/90	0.015
8	GLOBAL	±45	0.015
9	LOCAL	0/90	0.015
10	LOCAL	±45	0.015
11	LOCAL	±45	0.015
12	LOCAL	0/90	0.015
13	LOCAL	±45	0.015
14	LOCAL	±45	0.015
15	LOCAL	0/90	0.015
16	LOCAL	±45	0.015
17	LOCAL	±45	0.015
18	LOCAL	0/90	0.015
19	LOCAL	±45	0.015
20	LOCAL	±45	0.015
21	LOCAL	0/90	0.015

UNLESS OTHERWISE SPECIFIED:  
 DIMENSIONS ARE IN INCHES  
 TOLERANCES:  
 ANGULAR: ± .5°  
 ONE PLACE DECIMAL: ± .1  
 TWO PLACE DECIMAL: ± .01  
 THREE PLACE DECIMAL: ± .005  
 MATERIAL  
 CYTEC 5320-1 3K 8HS

FINISH  
 SEE NOTES

DO NOT SCALE DRAWING

**PROPRIETARY AND CONFIDENTIAL**  
 THE INFORMATION CONTAINED IN THIS DRAWING IS THE SOLE PROPERTY OF JAYHAWK MOTORSPORTS. ANY REPRODUCTION IN PART OR AS A WHOLE WITHOUT THE WRITTEN PERMISSION OF JAYHAWK MOTORSPORTS IS PROHIBITED.

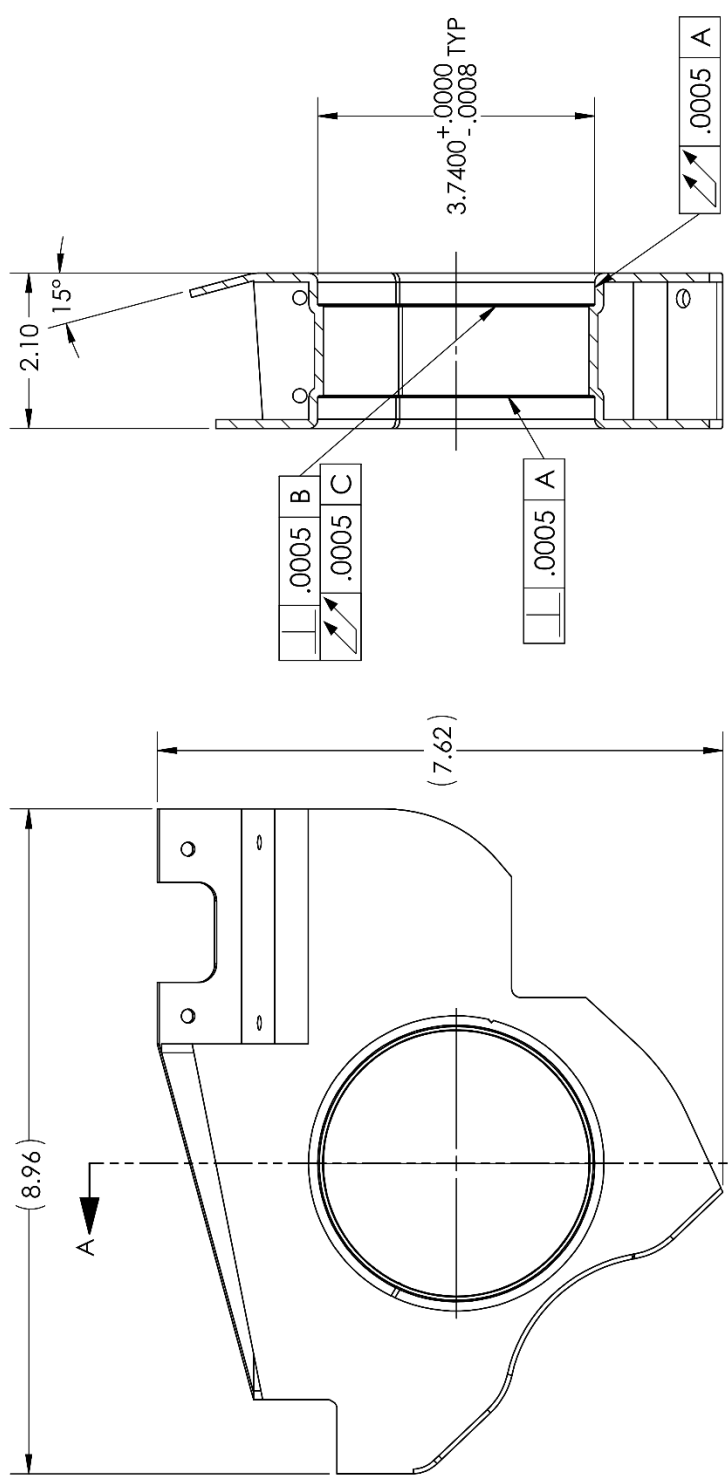
DRAWN	NMD	DATE	2/21/19
CHECKED			
ENG APPR.	RMS		3/13/19
MFG APPR.			
MFR			
COMMENTS: REMOVE SHARP EDGES			

Jayhawk Motorsports  
 RACING TEAM

Upright, Rear, Left

SIZE DWG. NO. REV  
**A** JMS19-5045P **L**

SCALE: NTS WEIGHT: 1.123 SHEET 1 OF 8



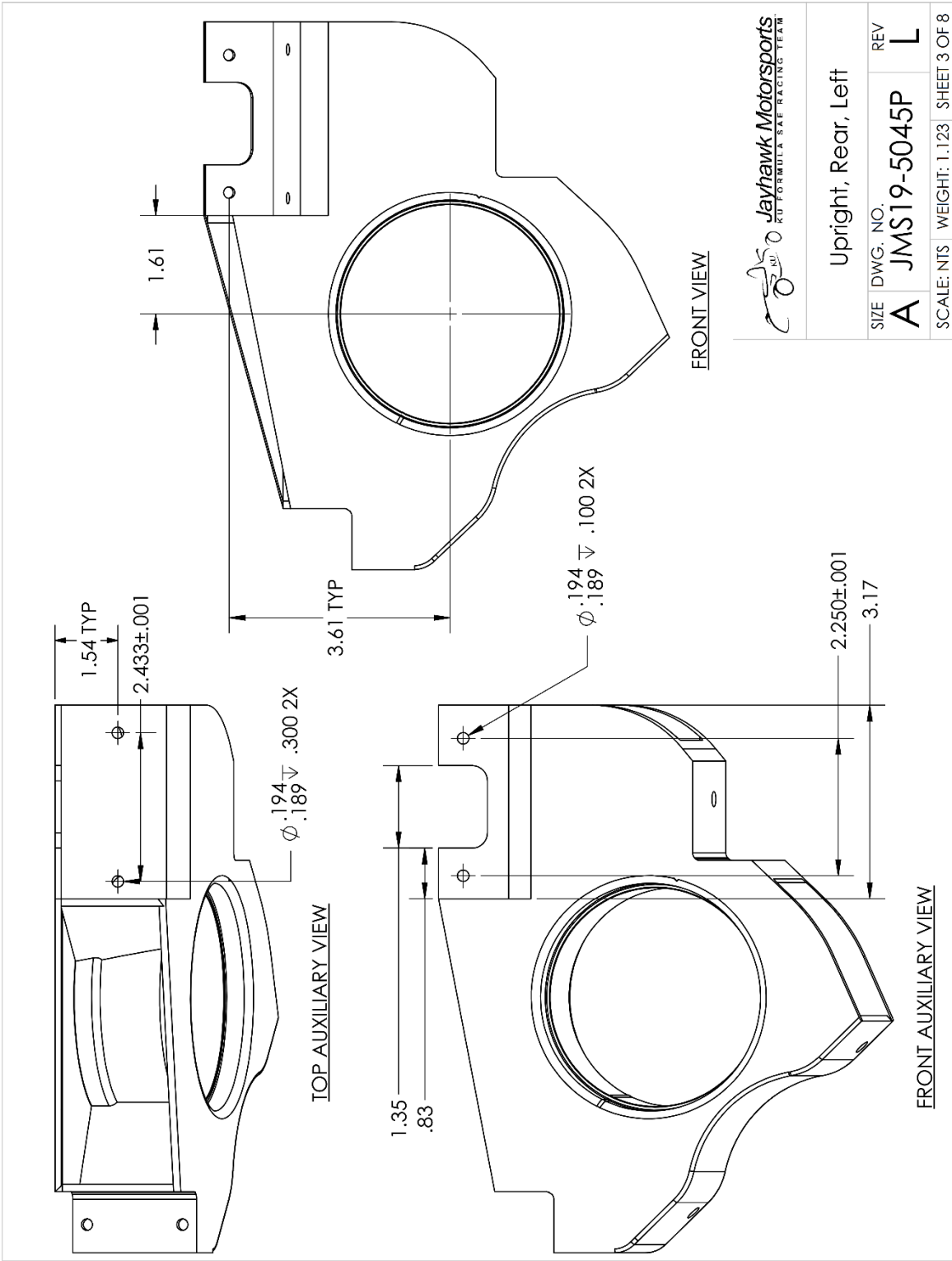
SECTION A-A



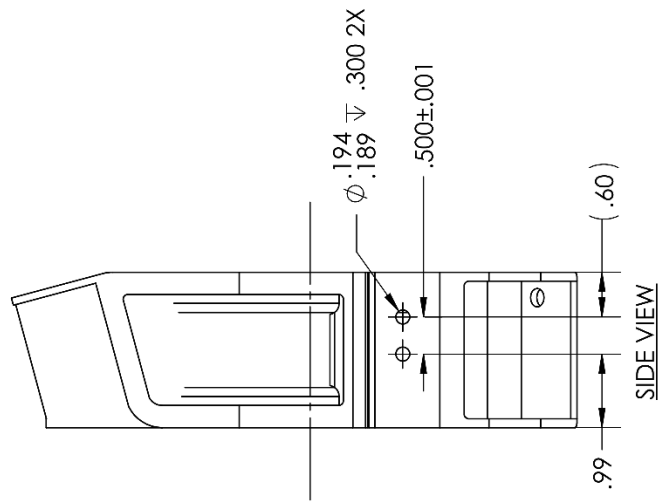
Upright, Rear, Left	
SIZE	DWG. NO.
<b>A</b>	<b>JMS19-5045P</b>
SCALE: NTS	WEIGHT: 1.123 SHEET 2 OF 8
REV	<b>L</b>

FRONT VIEW

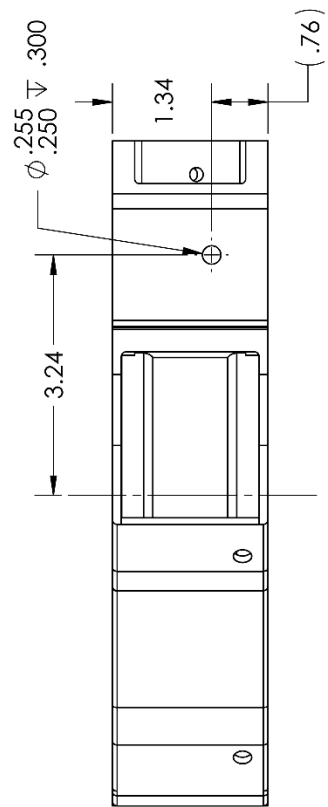
SOLIDWORKS Educational Product. For Instructional Use Only.



SOLIDWORKS Educational Product. For Instructional Use Only.



FRONT VIEW



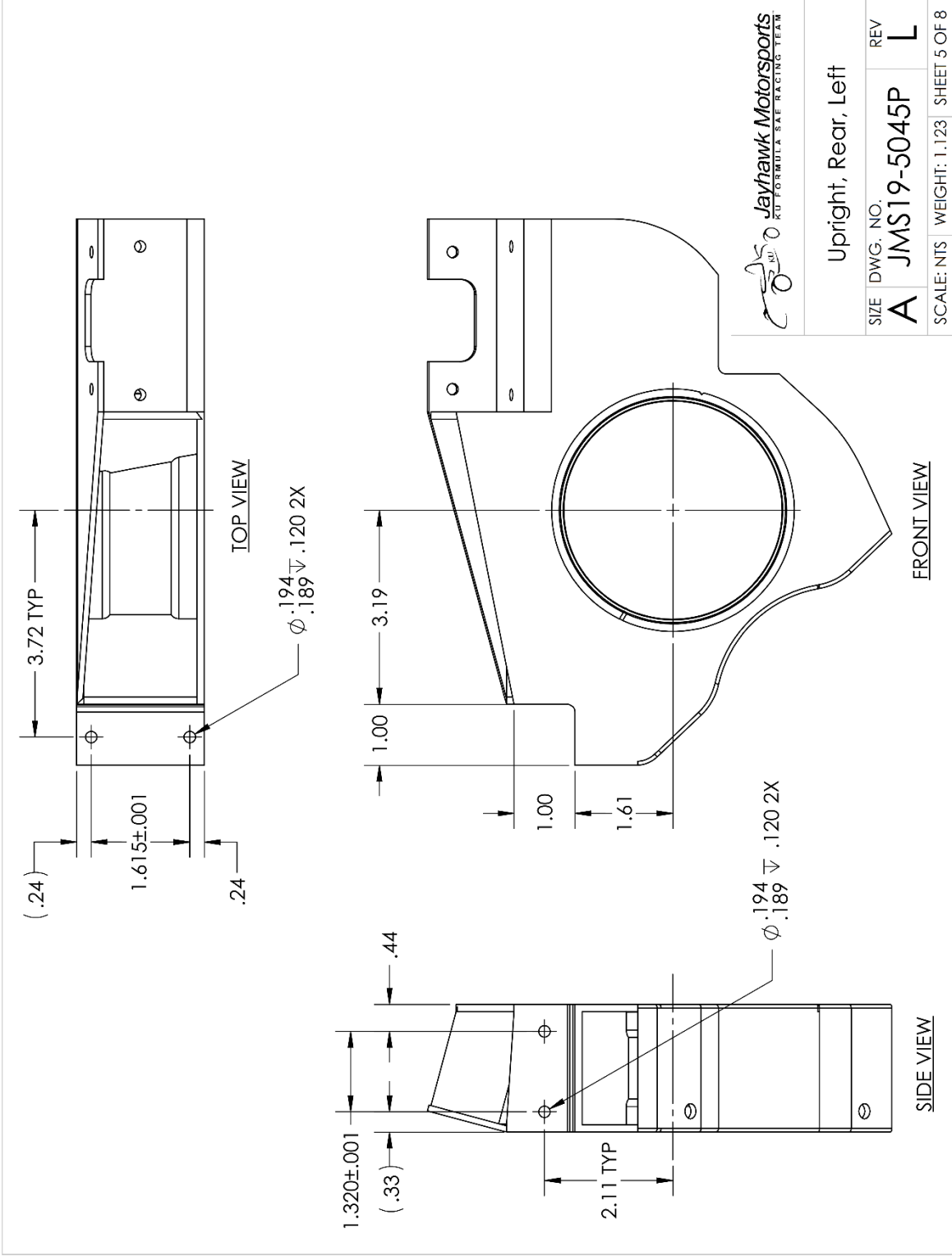
BOTTOM VIEW



Upright, Rear, Left

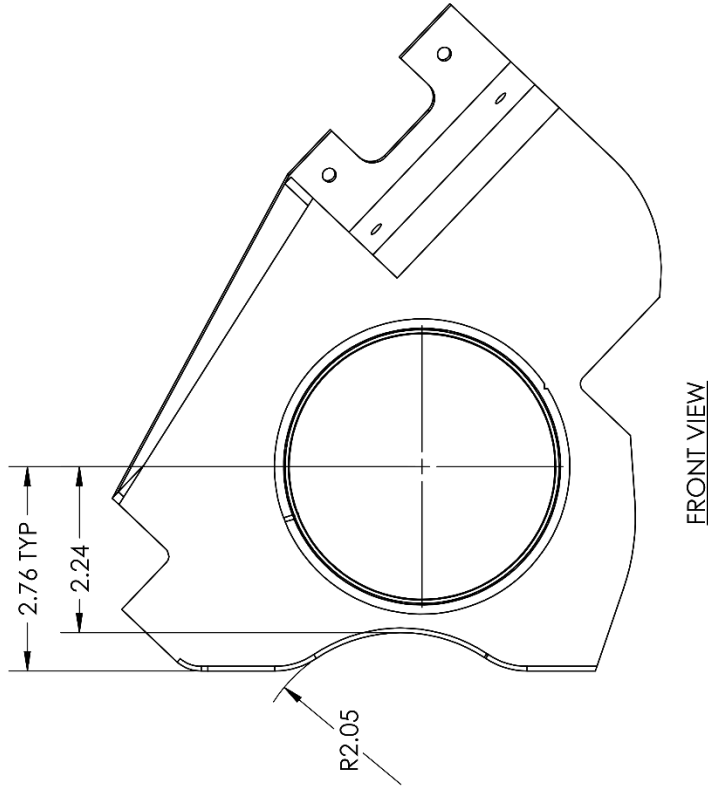
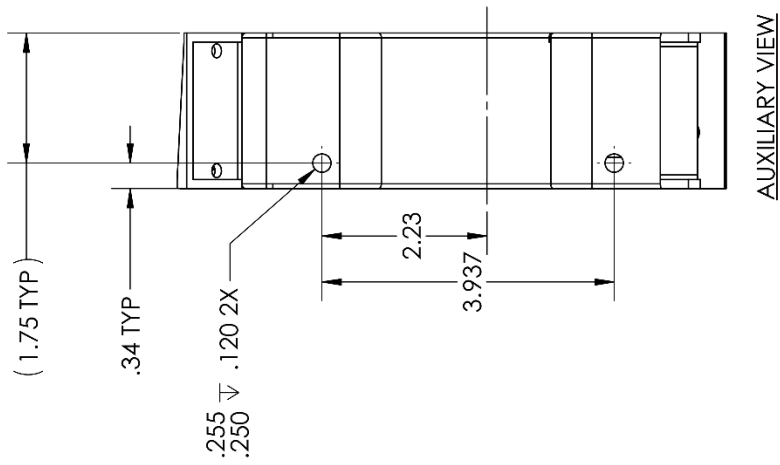
SIZE	DWG. NO.	REV
A	JMS19-5045P	L

SCALE: NTS WEIGHT: 1.123 SHEET 4 OF 8



SOLIDWORKS Educational Product. For Instructional Use Only.



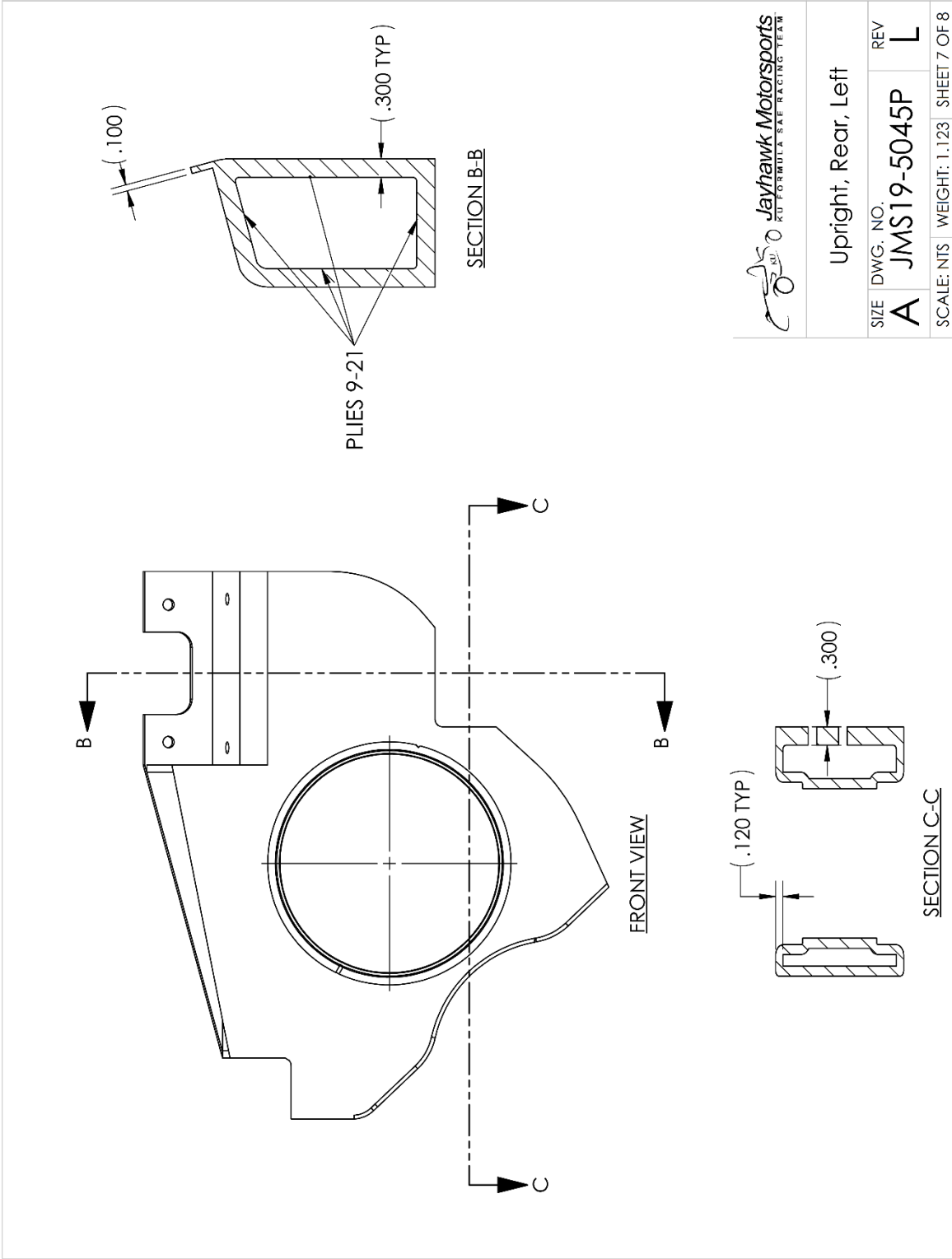


Upright, Rear, Left

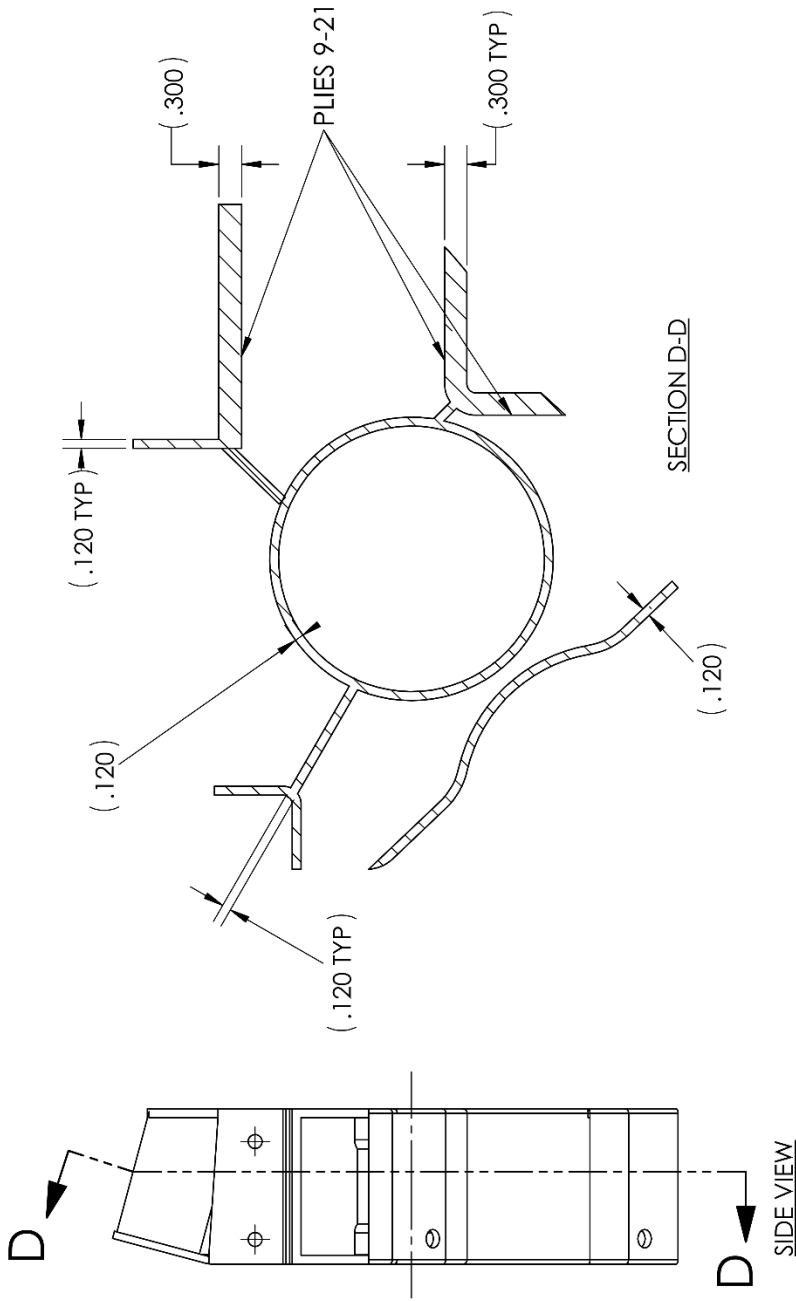
SIZE	DWG. NO.	REV
A	JMS19-5045P	L

SCALE: NTS WEIGHT: 1.123 SHEET 6 OF 8

SOLIDWORKS Educational Product. For Instructional Use Only.



SOLIDWORKS Educational Product. For Instructional Use Only.



Upright, Rear, Left


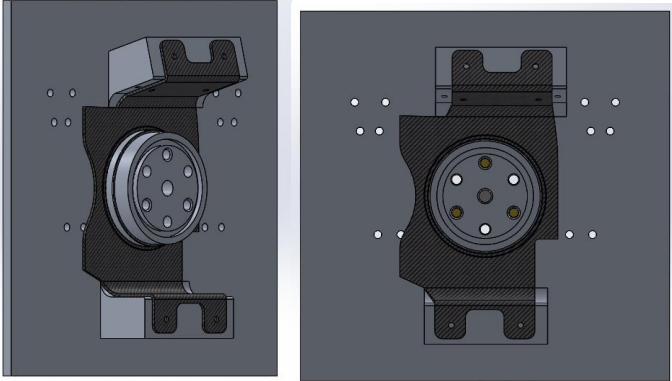
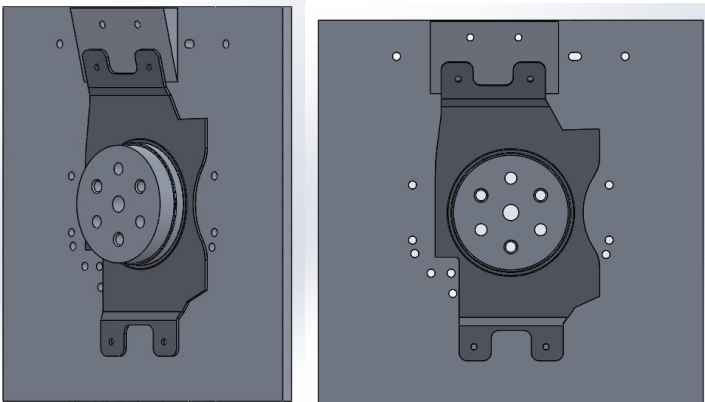
SIZE	DWG. NO.	REV
A	JMS19-5045P	L

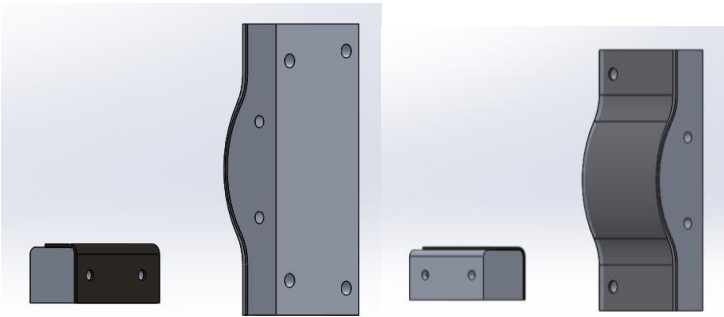
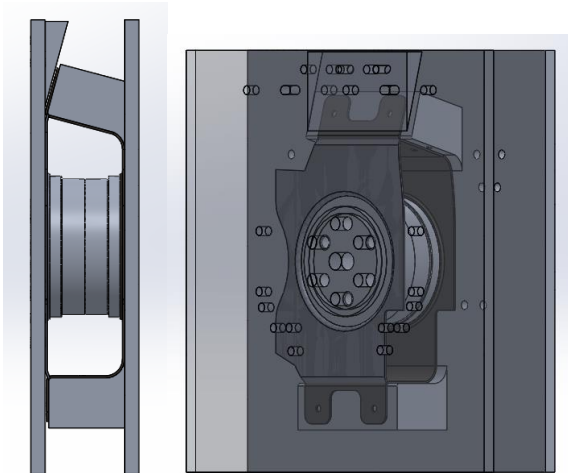
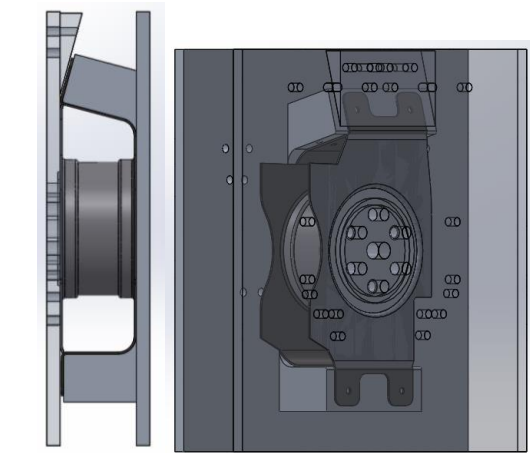
SCALE: NTS WEIGHT: 1.123 SHEET 8 OF 8

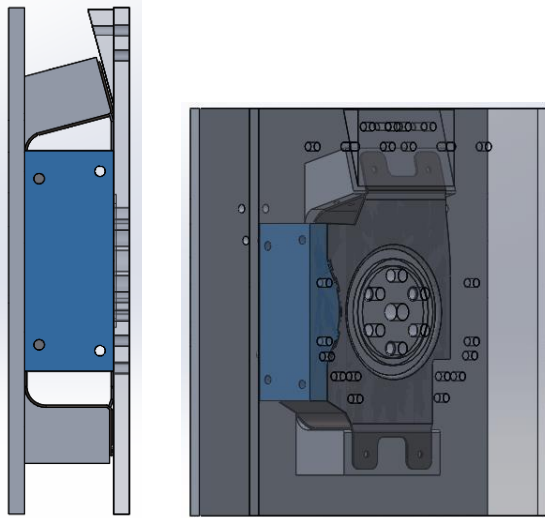
SOLIDWORKS Educational Product. For Instructional Use Only.

**Appendix B: Front and Rear Upright Manufacturing Overview**

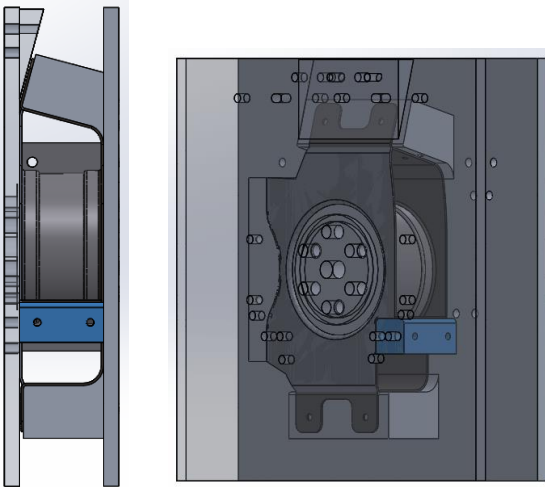
## JMS-5043P and JMS-5044P Manufacturing Overview

	<p>Clean and prepare tooling in configuration to manufacture front left or front right upright.</p>
	<p>Apply global plies one through four to surface of side one.</p> <p>[0/90, 45]<sub>s</sub></p>
	<p>Apply global plies one through four to surface of tool side two.</p> <p>[0/90, 45]<sub>s</sub></p>

	<p>Apply global plies one through four to surface of brake and steering mandrels.</p> <p>[0/90, 45]<sub>s</sub></p>
	<p>Join sides one and two of tool together and fasten through bearing mandrels using hardware.</p>
	<p>Apply global plies one through four around perimeter of bearing mandrels.</p> <p>[0/90, 45]<sub>s</sub></p>



Install brake mandrel into base plates. Fasten into place. Work material at radii onto surface of tool.



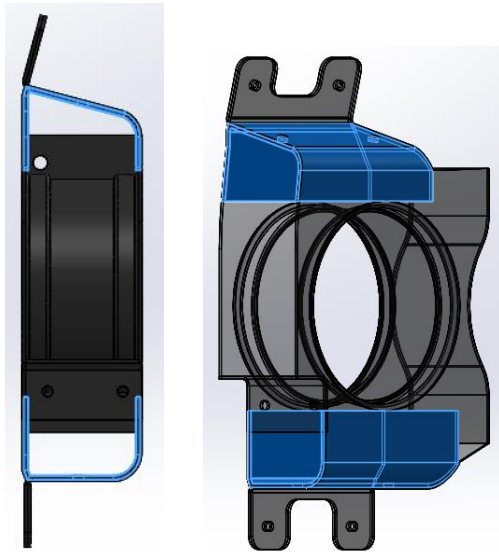
Install steer mandrel into base plates. Fasten into place. Work material at radii onto surface of tool.



Apply peel ply to laminate. Apply release film to part. Apply breather cloth to part. Place tool and part into vacuum bag. Draw air out and eliminate all air pockets and bridging.

Debulk part and tool in oven at 120°F for 2 hours.

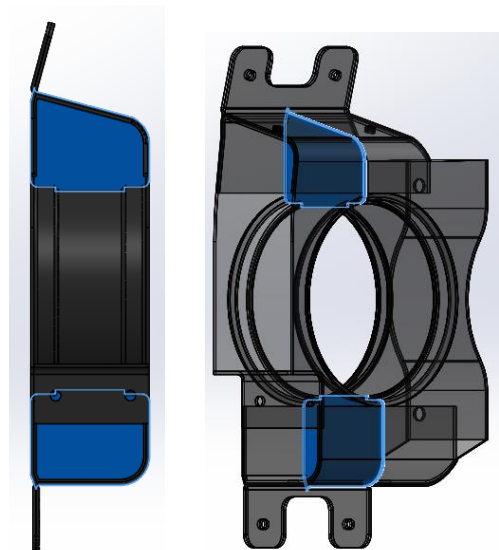
Reposition vacuum bag, check for air pockets and bridging. Cure in autoclave per CYTEC 5320-1 thermal ramp and dwell cycle.



Take part out of tool and remove peel ply. Trim edge of part to template. Wash out composite particulate and wipe down with solvent.

Install local upper and lower ball joint plies.

{0/90, 45, 0/90}



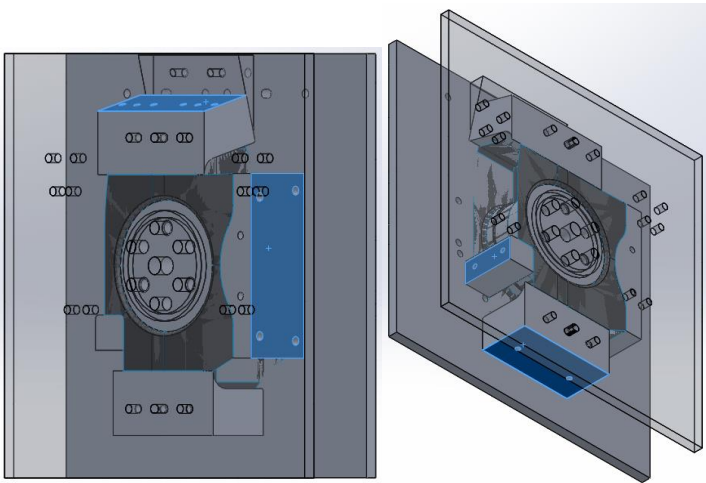
Install upper and lower lateral stiffeners to part per drawing.

[0/90, 45]<sub>s</sub>

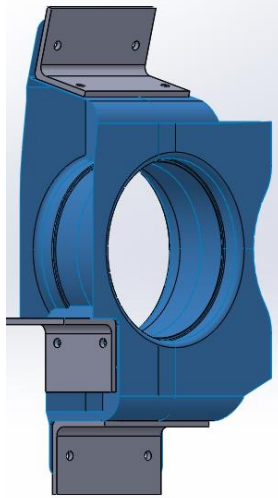
Apply release film to part. Apply breather cloth to part. Place part into vacuum bag. Draw air out and eliminate all air pockets and bridging.

Cure in autoclave per CYTEC 5320-1 thermal ramp and dwell cycle.



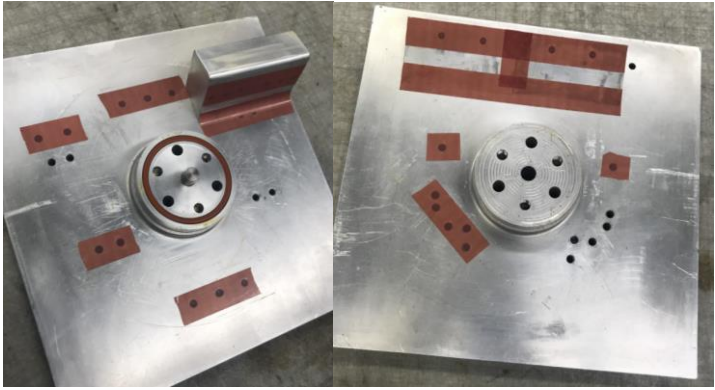
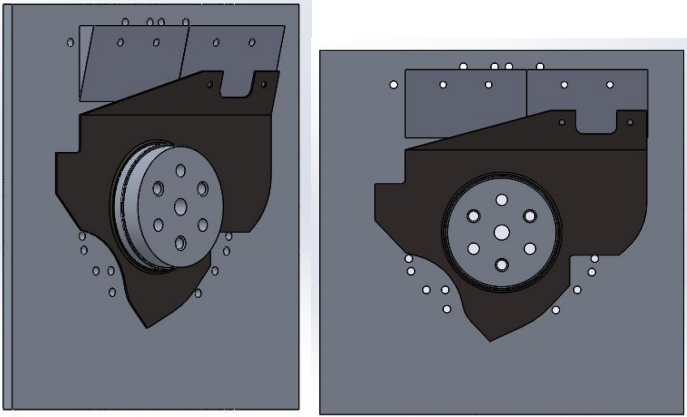
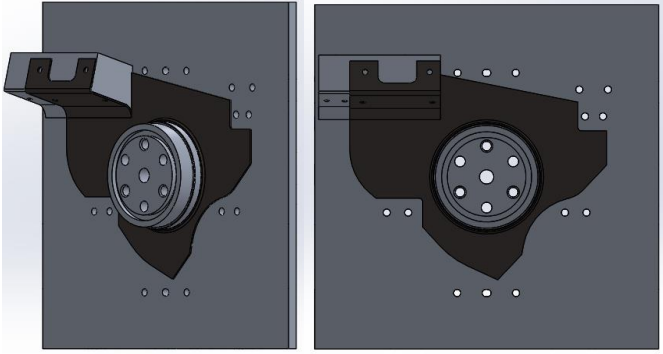


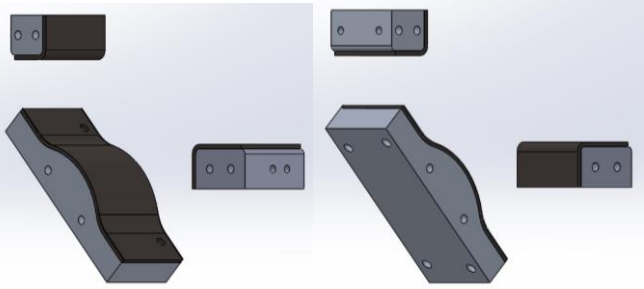
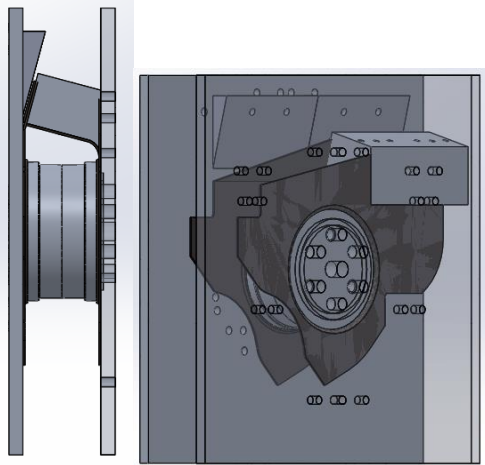
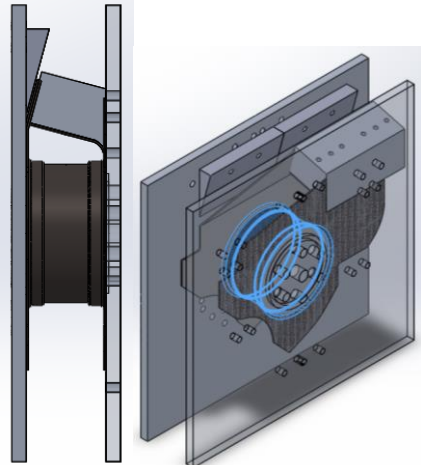
Place part into tool and drill per drawing. Remove from tool. Mark and trim edge of part to template.

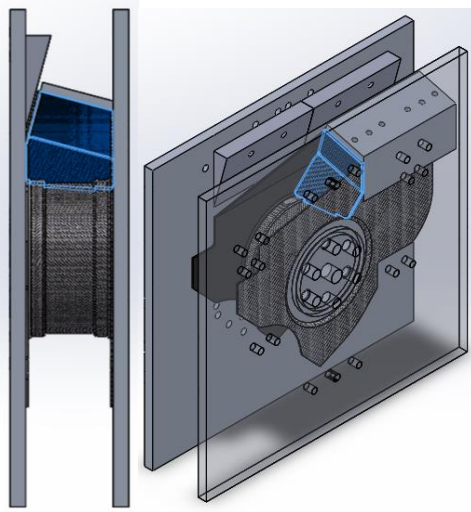


Install secondary fixtures to part and drill per drawing.

## JMS-5045P and JMS-5046 Manufacturing Overview

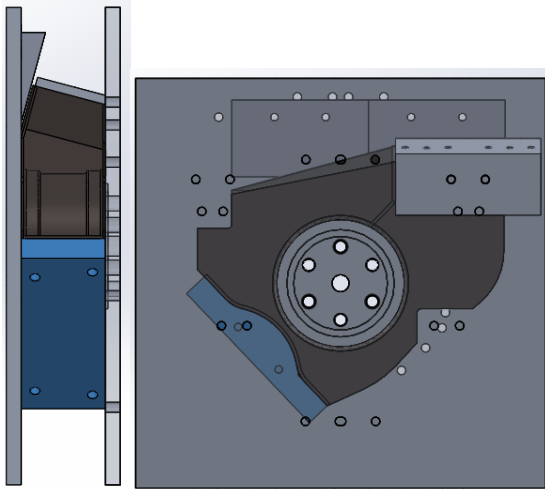
	<p>Clean and prepare tooling in configuration to manufacture rear left or front right upright.</p>
	<p>Apply global plies one through eight to surface of side one.</p> <p>[45, 0/90, 45, 0/90]<sub>s</sub></p>
	<p>Apply global plies one through eight to surface of tool side two.</p> <p>[45, 0/90, 45, 0/90]<sub>s</sub></p>

	<p>Apply global plies one through eight to surface of brake, lower ball joint, and toe-link mandrels.</p> <p>[45, 0/90, 45, 0/90]<sub>s</sub></p>
	<p>Join sides one and two of tool together and fasten through bearing mandrels using hardware.</p>
	<p>Apply global plies one through eight around perimeter of bearing mandrels.</p> <p>[45, 0/90, 45, 0/90]<sub>s</sub></p>

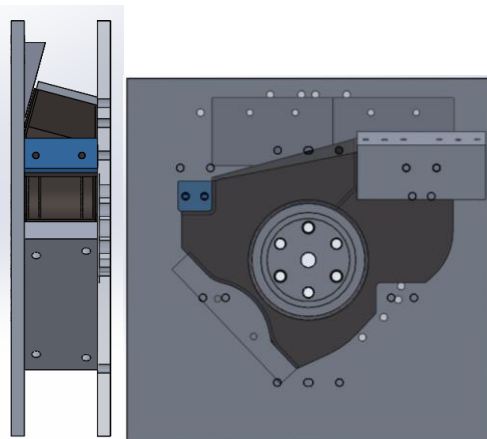


Apply global plies one through eight to upper ball joint lateral support.

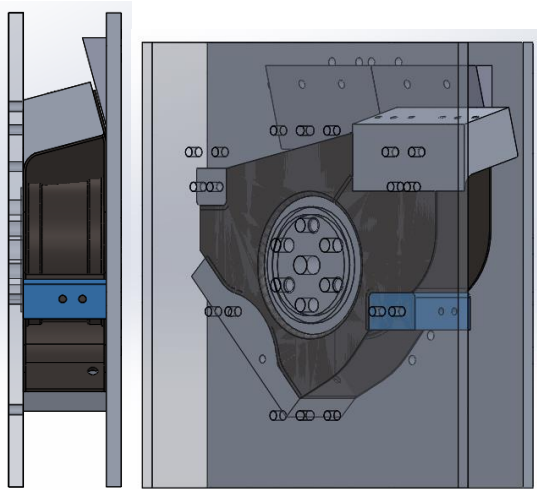
[45, 0/90, 45, 0/90]s



Install brake mandrel into base plates. Fasten into place. Work material at radii onto surface of tool.



Install toe-link mandrel into base plates. Fasten into place. Work material at radii onto surface of tool.



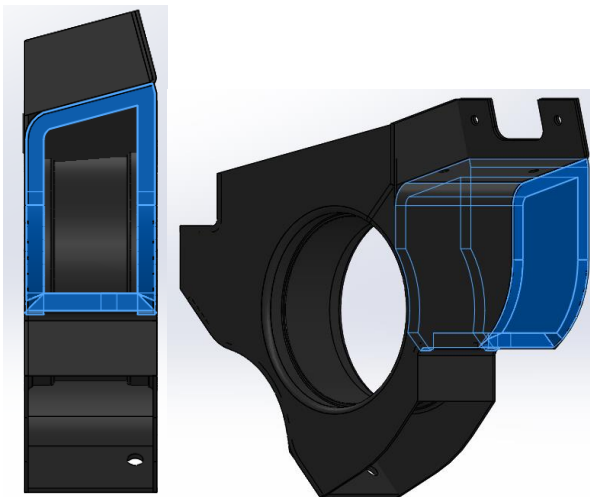
Install lower ball joint mandrel into base plates. Fasten into place. Work material at radii onto surface of tool.



Apply peel ply to laminate. Apply release film to part. Apply breather cloth to part. Place tool and part into vacuum bag. Draw air out and eliminate all air pockets and bridging.

Debulk part and tool in oven at 120°F for 2 hours.

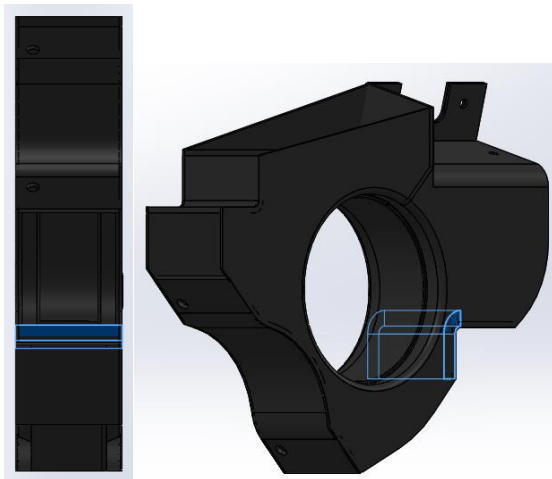
Reposition vacuum bag, check for air pockets and bridging. Cure in autoclave per CYTEC 5320-1 thermal ramp and dwell cycle.



Take part out of tool and remove peel ply. Trim edge of part to template. Wash out composite particulate and wipe down with solvent.

Install local upper and lower ball joint plies.

{0/90, 45, 45, 0/90, 45, 45, 0/90, 45, 45, 0/90, 45, 45, 0/90}

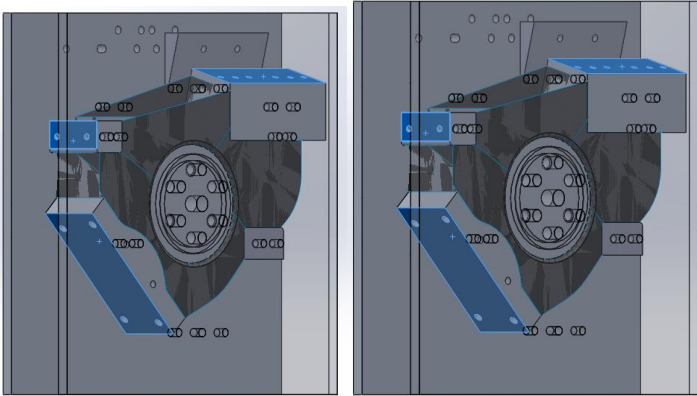


Continue installation of local lower ball joint plies.

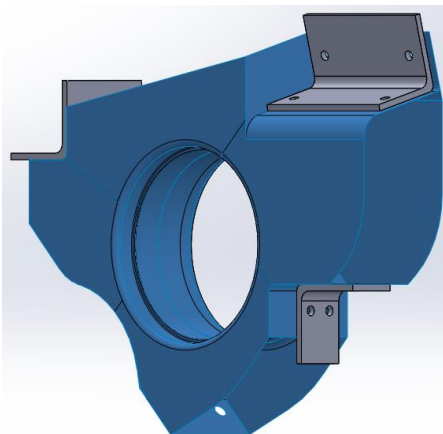
{0/90, 45, 45, 0/90, 45, 45, 0/90, 45, 45, 0/90, 45, 45, 0/90}

Apply release film to part. Apply breather cloth to part. Place part into vacuum bag. Draw air out and eliminate all air pockets and bridging.

Cure in autoclave per CYTEC 5320-1 thermal ramp and dwell cycle.



Place part into tool and drill per drawing. Remove from tool. Mark and trim edge of part to template.



Install secondary fixtures to part and drill per drawing.